

Review

Different Metal–Air Batteries as Range Extenders for the Electric Vehicle Market: A Comparative Study

Yasmin Shabeer ¹, Seyed Saeed Madani ¹, Satyam Panchal ¹, Mahboubeh Mousavi ² and Michael Fowler ^{1,*}

¹ Chemical Engineering, University of Waterloo, Waterloo, ON N2L3G1, Canada; yshabeer@uwaterloo.ca (Y.S.)

² AlumaPower Corporation, Kitchener, ON N2R1G1, Canada

* Correspondence: mfowler@uwaterloo.ca

Abstract: Metal–air batteries represent a category of energy storage system that leverages the reaction between metal and oxygen from the atmosphere to produce electricity. These batteries, known for their high energy density, have attracted considerable attention as potential solutions for extending the range of electric vehicles. Understanding the capabilities and limitations of metal–air batteries as range extenders is crucial for advancing electric vehicle technology, as these batteries could offer the additional energy needed to overcome current range limitations. This review paper provides a detailed overview of various metal–air battery technologies, delving into their design, functionality, and inherent challenges. By analyzing key theoretical and practical parameters, the study highlights how these factors influence overall battery performance. Additionally, the review addresses critical cost considerations, particularly the relationship between vehicle cost and driving range, uncovering the significant trade-offs involved in adopting metal–air batteries. Through an examination of nearly all the existing metal–air batteries, this paper sheds light on their potential to serve as effective range extenders, thereby facilitating the transition to a cleaner, more sustainable transportation landscape.

Keywords: metal–air batteries; range extenders; lithium–air battery; magnesium–air battery; sodium–air battery; aluminum–air battery; zinc–air battery; potassium–air battery; iron–air battery; calcium–air battery; silicon–air battery; germanium–air battery; electric vehicles



Academic Editors: Xiaoyuan Shi and Hengguo Wang

Received: 17 November 2024

Revised: 25 December 2024

Accepted: 18 January 2025

Published: 20 January 2025

Citation: Shabeer, Y.; Madani, S.S.; Panchal, S.; Mousavi, M.; Fowler, M. Different Metal–Air Batteries as Range Extenders for the Electric Vehicle Market: A Comparative Study. *Batteries* **2025**, *11*, 35. <https://doi.org/10.3390/batteries11010035>

Copyright: © 2025 by the authors. Licensee MDPI, Basel, Switzerland. This article is an open access article distributed under the terms and conditions of the Creative Commons Attribution (CC BY) license (<https://creativecommons.org/licenses/by/4.0/>).

1. Introduction

The extensive use of fossil fuels has been the primary driver of long-term climate change for the past 150 years, responsible for a staggering 75% of global greenhouse gas emissions and 90% of global carbon dioxide (CO₂) emissions. As fossil fuel reserves continue to dwindle and geopolitical tensions heighten over their supply, the imperative to develop alternative energy sources is becoming increasingly urgent in modern civilizations. Solar, wind, wave, biomass, and other renewable energy sources hold promise as alternatives to reduce dependence on fossil fuels. However, their widespread adoption faces significant challenges related to efficiency and regulatory hurdles. There is still a significant distance to cover in addressing the ecological damage brought on by the exploitation of fossil fuels by transitioning to renewable energy sources [1–12].

Motivated to decrease carbon emissions and dependence on fossil energy, a global transition towards electric vehicles (EVs) signifies a critical juncture in the automotive sector. Evidently, the ambitious goal of significantly reducing CO₂ emissions necessitates a multifaceted approach that includes the widespread deployment of EVs alongside a strategic focus on integrating renewable energy sources into the grid [13–15]. Although there

have been notable improvements in EV technology, the restricted range of existing battery systems hinders widespread adoption. This limitation translates into a critical concern for the EV industry in the form of range anxiety. Consumers remain apprehensive about the driving distance achievable on a single charge, ultimately dampening consumer confidence and hindering the overall growth of the EV market [16–21]. The rapid progress of energy storage technologies has been crucial in promoting the widespread use of battery-powered solutions in the automotive industry. Batteries are the core component of EVs and are essential in determining the driving range and overall performance of these environmentally friendly battery electric vehicles (BEVs). Advancements in battery technology are crucial for overcoming range limitations while alleviating concerns like range anxiety. This will demonstrably improve consumer acceptance of EVs, thereby expediting their universal adoption as a sustainable transportation solution [22–24].

Lithium-ion (Li-ion) systems currently dominate the battery industry, powering not only EVs but also a myriad of consumer electronics. They have experienced a significant advancement in energy density, rising from around 90 Wh kg⁻¹ to a contemporary range of ~100 to ~300 Wh kg⁻¹ between the 1990s and now. Though this advancement has permitted larger vehicles to cover typical driving patterns, this is insufficient for BEVs striving to outperform internal combustion engine vehicles (ICEVs), which typically achieve a mileage equivalent of about 7 to 11 kilometers per liter of gasoline, varying based on the model [25–31]. Contrariwise, lithium-powered systems are unable to meet the escalating demand for energy storage, particularly within the automotive sector. In the wake of recent regulations and the fact that lithium comprises only 0.0017% of the Earth's crust the demand for electric vehicle batteries is anticipated to increase substantially over the next decade [32,33]. To accommodate the driving patterns mentioned earlier, BEV manufacturers are compelled to include large and bulky Li-ion battery packs, which are both heavy and expensive, thereby limiting the ability of EVs to compete with standard ICEVs. Furthermore, safety issues related to Li-ion systems are of primary concern due to the significant potential risks to users resulting from battery malfunctions. This failure can occur due to an electrical shortage caused by the formation of dendritic lithium during rapid charging, or thermal runaway resulting from overcharging/discharging. These failures could potentially cause fires due to the highly combustible electrolyte used in Li-ion cells, consequently leading to a multitude of accidents involving these batteries, as analyzed by Yu et al. [34] in Figure 1. A further significant concern is the negative environmental impact of Li-ion systems. The extraction, production, and indiscriminate disposal of these batteries contribute to environmental issues, primarily because of the existence of hazardous substances and specifically, heavy metals classified as such, including nickel and cobalt. The recycling of the Li-ion system continues to pose challenges, primarily stemming from economic feasibility issues and the complexity of the disassembly process. Consequently, the combination of lithium scarcity, limited energy capacities, extended charging durations, adverse environmental effects, and safety apprehensions surrounding their components collectively hinder the widespread adoption and commercialization of Li-ion systems, particularly within the realm of the EV industry [35–43].

To address the challenges posed by Li-ion systems and meet the growing demands in the energy sector, researchers are focusing on the advancements of metal–air/oxygen batteries. Metal–air batteries (MABs), consisting of electrolytes and bifunctional air electrodes, typically function by extracting atmospheric oxygen and simultaneously converting metal anodes into their oxide forms. The batteries utilize a range of metal electrodes, including alkali metals like potassium (K), lithium (Li), and sodium (Na), metalloids like germanium (Ge) and silicon (Si), as well as transition metals, and post-transition metals such as aluminum (Al), calcium (Ca), iron (Fe), magnesium (Mg), tin (Sn), zinc (Zn), and

vanadium (V). MABs have a remarkable theoretical energy density that falls within the range of 1353 to 11,429 Wh kg⁻¹ (per unit weight) based on calculations for common MABs including those utilizing Li, Zn, Al, and Mg [44,45].

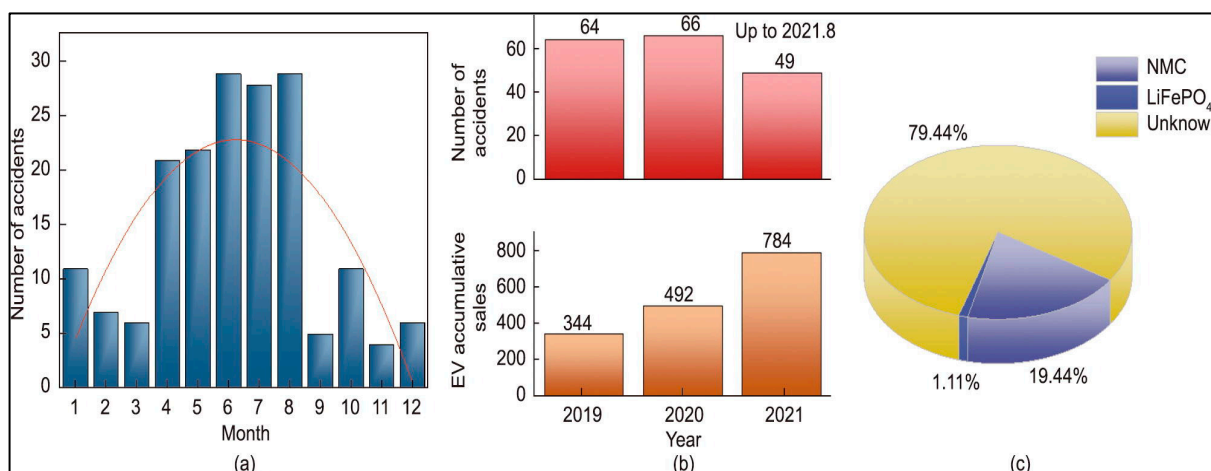


Figure 1. Compilation of EV fire occurrences from January 2019 to August 2021: (a) Monthly count of EV fire incidents. (b) Comparison of annual EV fire incidents and the total number of EVs sold. (c) Distribution of accidents attributed to various types of Li-ion battery [34].

The development of MABs has a rich history rooted in the quest for high-energy-density storage systems. Originating in the mid-20th century, early research focused on zinc-air batteries due to their simplicity and practical energy potential. However, advancements gained momentum with the rising demand for sustainable energy solutions, particularly for electric vehicles and renewable energy integration. Innovations in electrode design, catalysts, and electrolytes have progressively addressed challenges like poor rechargeability and limited cycle life [46,47]. The essence of MABs lies in their innovative design, where electrical energy is generated through the reaction of atmospheric oxygen with a metallic electrode. The process underscores the pivotal role of air in facilitating the electrochemical reactions within these batteries, resulting in efficient energy conversion and storage. This dynamic offers a promising avenue for advancing energy storage technologies toward higher performance and sustainability through the unique interplay between air and metal electrodes. Thus, MABs are anticipated to have a significant impact in the markets of the automobile, consumer electronics, stationary storage, defense, marine, and aviation markets [48,49].

MABs have become prominent because of their efficient operation in outdoor settings, making them ideal for meeting the high energy requirements of EVs. Researchers anticipate that specific MABs will directly replace Li-ion batteries, while others will act as range extenders. This feature reduces range anxiety, enhances safety, and improves cost efficiency by decreasing the size of Li-ion batteries when they are not replaced directly. Figures 2 and 3 give a visual summary of essential parameters influencing the selection and utilization of various metals in MAB technologies. Figure 2 presents a comparative analysis of the energy parameters of different metals used in MABs, highlighting the theoretical volumetric energy density in Wh L⁻¹, specific energy in Wh kg⁻¹, and nominal cell voltage in V. Concurrently, Figure 3 illustrates the cost and abundance of these elements, offering insights into their economic feasibility and natural availability.

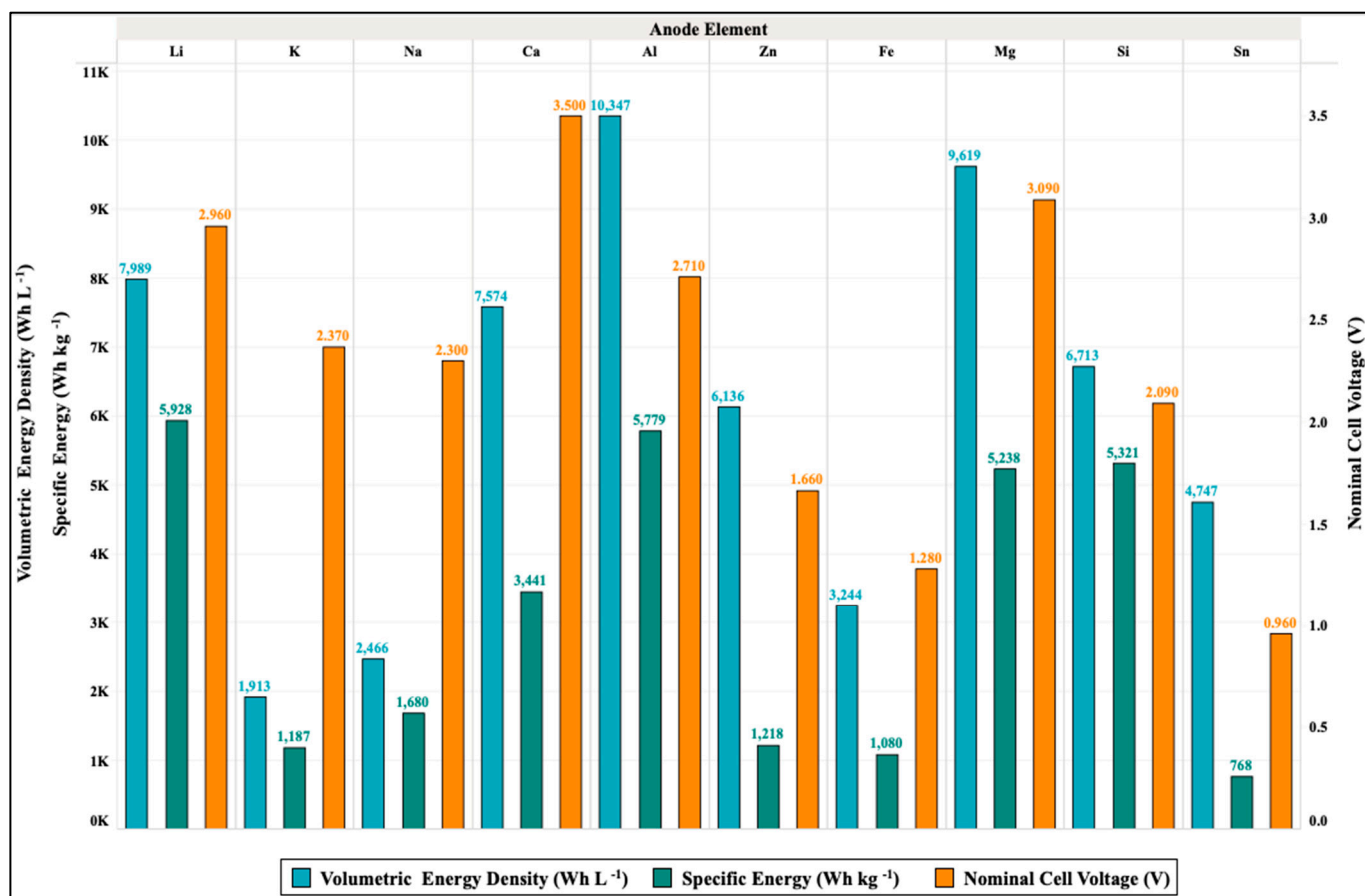


Figure 2. Comparison of the performance of several metal-air batteries, highlighting the theoretical specific energy, volumetric energy density, and nominal cell voltage.

Together, these figures present a holistic perspective on the essential parameters that must be considered when evaluating the practicality and efficiency of using these different metals. From the graph, lithium appears to be a very effective anode because of its superior theoretical specific energy of 5928 Wh kg⁻¹ and an open circuit voltage (OCV) of 2.96 V. Nevertheless, the very low abundance (<0.0017 %) and high cost of lithium metal (46 USD kg⁻¹), combined with its intrinsic instability when it comes into contact with air and aqueous electrolytes, present significant challenges [50]. Subsequently, Al metal emerges as a promising candidate due to its exceptional theoretical specific energy of 5779 in Wh kg⁻¹ and its energy density of 10,347 Wh L⁻¹. Al metal is also known for its high safety, cost-effectiveness, and abundance. However, its high corrosion rate in aqueous electrolytes, coupled with parasitic reactions, diminishes its overall performance [51]. The appeal of employing Mg metal in MABs lies in their ability to achieve uniform metal deposition and significant theoretical energy potentials (energy density of 9619 Wh L⁻¹, specific energy of 5238 Wh kg⁻¹, and OCV of 3.090 V). However, the ubiquitous usage of magnesium electrodes in aqueous electrolytes is impeded by significant corrosion challenges and high self-charge characteristics. The high corrosion rates compromise the electrode's longevity and performance, posing a substantial barrier to its practical application [52]. Additionally, the cost of magnesium, approximately 11.02 USD kg⁻¹, coupled with its relatively limited abundance of only 2.10%, further limits its viability as a sustainable material in large-scale energy storage solutions.

It should be noted that, as of this point, in the context of aqueous MABs, only MABs with Zn anodes can be electrically recharged, while Mg- and Al-employing air batteries require mechanical replacement of these metal anodes due to their inability to be directly

converted from ions to metal [53]. Given this unique advantage, employing Zn as the metal anode presents promising opportunities for the development and enhancement of MAB technology. Zn is one of the most widely researched anodes for MABs with a high theoretical energy density of 6136 Wh L^{-1} and a specific energy of 1218 Wh kg^{-1} . However, limitations such as the formation of Zn dendrites and low cycle life need to be addressed to enhance its commercial viability [54,55]. While Na and K metals exhibit some chemical similarities to Li, their application as a viable battery alternative faces substantial hurdles. These hurdles include the lack of comprehensive understanding of the underlying electrochemistry, the development of stable electrolytes, and the design of high-performance electrode materials for these batteries [56,57]. Other metal anodes such as Fe, Si, Ca, and Sn, while less extensively researched, show promising potential due to their high crustal abundance and lower costs.

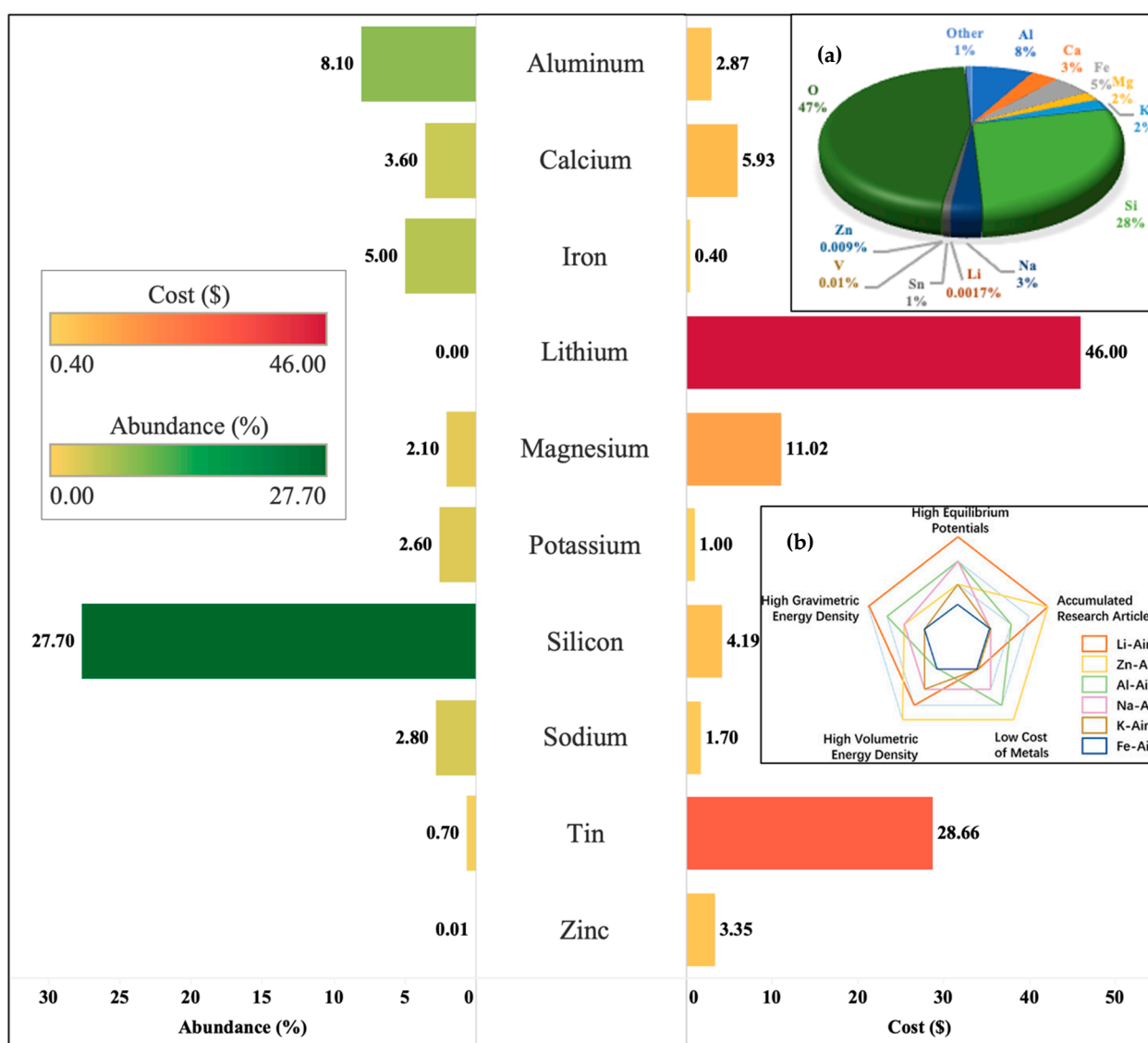


Figure 3. Abundance vs. cost of metal–air battery elements. Refer to the inset (a) for the earth’s crustal distribution (based on data from [49,58,59]) and inset (b) for a radar chart illustrating the benefits and drawbacks of various types of metal–air batteries based on research articles collected from the Web of Science between 2000 and 2023 (adapted from [55]).

Currently, none of these battery chemistries have achieved the technological maturity required for widespread industrial adoption. As a result, their potential to either replace

or supplement Li-ion batteries as the primary power source or range extenders for future EVs remains highly uncertain. Although some studies explore the potential of specific MABs like Li-air or Zn-air batteries as range extenders, they do not offer a comprehensive comparison of all the MABs currently being studied in the field. Thus, this comparative review aims to bridge this knowledge gap by offering a comprehensive analysis of different MABs as potential EV range extenders. The review will delve into their structural compositions, operational principles, performance metrics, and existing challenges. By critically evaluating the strengths and limitations of each battery type, the goal is to illuminate their suitability for integration into the rapidly evolving EV market. Section 2 introduces MABs as energy storage systems and delves into specific types with different anodes, describing in detail their types, working principles, advantages, and challenges. Section 3 provides a comparison of the practical properties of these MABs, focusing on factors such as driving range, battery pack volume, and total vehicle cost. Section 4 concludes with summarizing remarks, encapsulating the observations made throughout the review.

2. Metal–Air Batteries

The operational mechanisms of both aqueous and non-aqueous MABs and the various configurations are depicted in Figure 4 [60]. In essence, these batteries consist of three key parts: an anode (metal), an electrolyte solution positioned between the electrodes, and a permeable air-cathode. The categorization of MABs by Wang et al. [60] includes three distinct types: static battery setups with multiple cells, cell configurations with electrolyte flow, and innovative flexible battery designs.

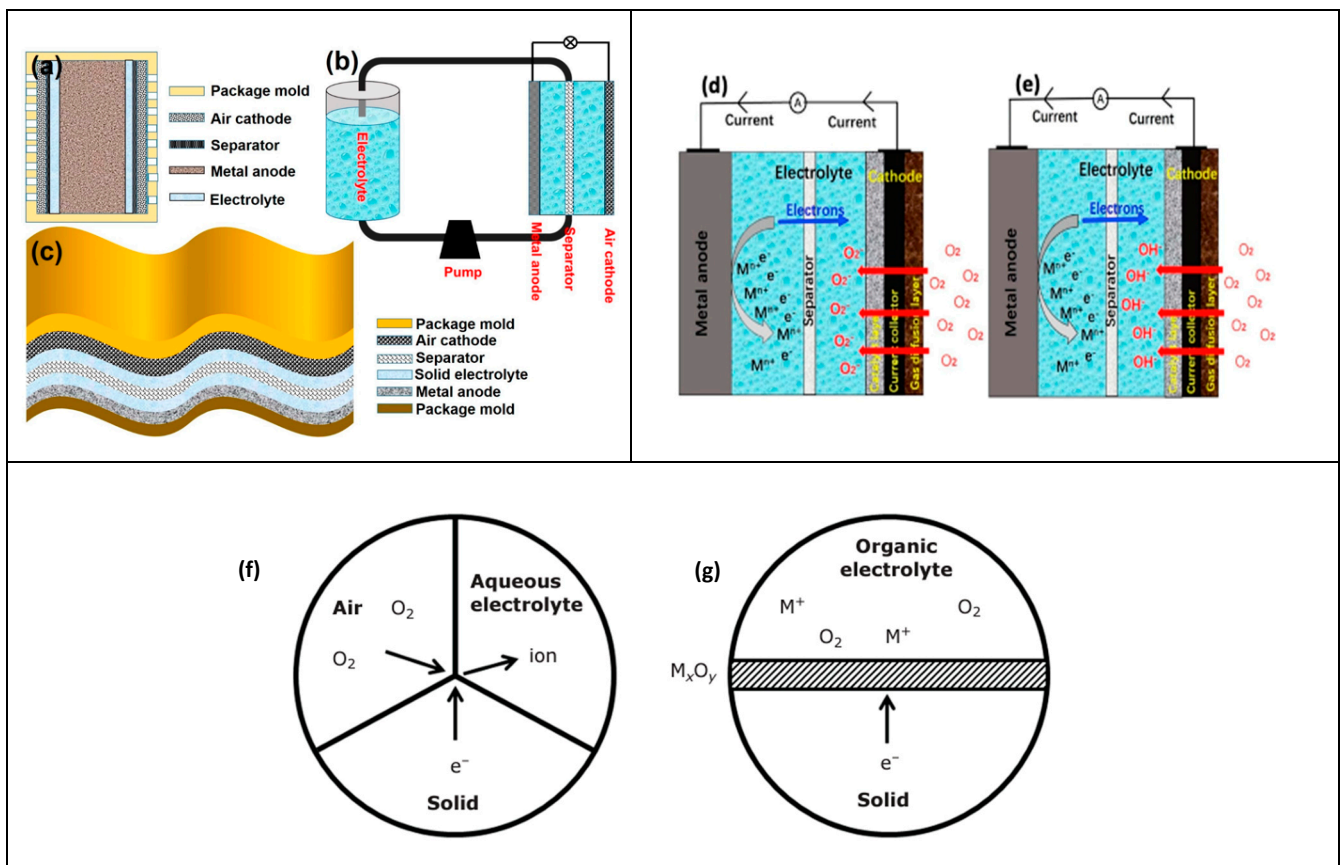


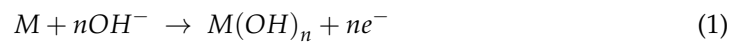
Figure 4. Illustration of different configurations of MABs, including a conventional static battery setup (a), a cell design with electrolyte flow (b), and a novel flexible cell design (c); (d,e) representations of non-aqueous and aqueous electrolyte MABs, respectively [60]; (f,g) a phase boundary diagram for both aqueous and non-aqueous electrolytes (modified from [48]).

In conventional static electrochemical setups, such as the one depicted in Figure 4a, four critical components are employed: a cathode, a separator, an electrolyte, and an anode. The anode reaction exhibits rapid kinetics, while the oxygen-reduction reaction (ORR) at the positive electrode is kinetically slow. This sluggishness is attributed to the reaction occurring at a three-phase boundary (solid catalyst, liquid electrolyte, and gaseous oxygen) that is crucial for the ORR. Furthermore, the oxygen-evolution reaction (OER) proceeds concurrently on the cathode at a two-phase boundary, consisting solely of the catalyst and electrolyte. Achieving optimal performance for both the OER and ORR necessitates the use of highly efficient dual-functional catalysts. However, a significant obstacle for conventional static designs is the accumulation of solid byproducts on the surfaces of both electrodes during the cycling of the cell. These deposits can block electrode pores, impeding air diffusion and ultimately reducing battery performance. Flow batteries (Figure 4b) include electrodes, an electrolyte, a separator, and an additional reservoir for storing the electrolyte, often accompanied by a pump to facilitate electrolyte flow. This flowing-electrolyte configuration mitigates some issues related to both positive and negative electrodes.

For example, in Zn–Ni battery types, a large volume of flowing electrolyte helps to prevent dendrite growth and uneven zinc geometry variations, thus mitigating passivation through enhanced current uniformity and reduced concentration disparities. Despite these advantages, the complex configuration of flowing electrolytes introduces drawbacks such as decreased energy efficiency and volumetric density, along with the necessity for auxiliary flow channels and pumps to enhance electrolyte circulation during cell operation. Han et al. [61] conducted an extensive review comparing static and flow batteries, providing a detailed analysis of their respective advantages and challenges. Flexible batteries (Figure 4c) have gained significant attention recently due to the rising demand for portable electronics. These miniaturized batteries prioritize high energy density within a lightweight form factor. They achieve this through a combination of electrodes, a separator, and a high-conductive (often solid-state) electrolyte. The small thickness of the metal anode further reduces the overall mass of the cell. Different nanomaterials like graphene, carbon nanotubes, and fibers are being investigated for optimal cathode performance. Flexible battery technology is transitioning beyond basic chemistries, with the emerging lithium-based and metal–air options. Notably, Zn and Al-based MABs are currently favored for the application of flexible electronics owing to their massive specific energy, safety profile, and cost-effectiveness [62–67].

Regarding the categorization of MABs depending on the electrolyte type, there are various kinds of electrolytes employed: aqueous (water-based), non-aqueous (organic solvent-based), solid-state (no liquid component), and hybrid (combinations of the above). Metal electrodes that are highly water-sensitive, such as those in lithium-, potassium-, and sodium–air batteries, cannot utilize aqueous electrolytes, as these alkali metals react vigorously with water, often leading to hazardous situations. In contrast, other types of MABs, including those with aluminum, zinc, iron, or magnesium electrodes, which are compatible with water, can use both aqueous and non-aqueous electrolytes, among others [62,68–70]. The distinctions between reactions in aqueous and non-aqueous MABs pose unique challenges for technological implementation, as elucidated in the review by Hardwick et al. [48]. In non-aqueous MABs, the ORR leads to the generation of metal oxides that precipitate on the surface of the permeable air-cathode itself. Conversely, in alkaline-based aqueous MABs, the anodic metallic ions do not arrive at the positive electrode; instead, the precipitation of these metal ions occurs by the reaction with hydroxide ions (OH^-), or they form a complex with a negative charge, such as the zincate anion ($\text{Zn}(\text{OH})_4^{2-}$) near the anode, preventing its migration to the cathode. Aqueous MABs encounter the

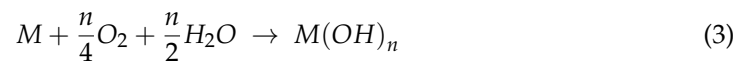
additional hurdle of low oxygen solubility in water (0.2 mM) under atmospheric pressure, necessitating the utilization of gaseous oxygen. Atmospheric oxygen permeates into the air-cathode propelled by the pressure gradient between the cell's interior and exterior. Catalysts enable the formation of hydroxyl (OH^-) ions in the basic media by oxygen reduction, with electrons produced at the negative electrode, potentially resulting in the production of metal hydroxides in solid form. This three-phase reaction involves a solid catalyst, a liquid electrolyte, and gaseous oxygen, as depicted in Figure 4f. Meanwhile, Figure 4g portrays the boundary diagram of non-aqueous MABs, facilitating a comparison between them [71–77]. Within aqueous MABs, the anode undergoes an oxidation reaction during discharge, releasing electrons and simultaneously forming metal hydroxide as the metal cations react with OH^- ions,



Here, M represents the metal, and n stands for the valence metal ions. The liberated electrons (e^-) travel via the closed circuit and arrive at the positive electrode to engage in the ORR. There, the oxygen molecules present in the ambient air, coupled with the e^- and water, undergo reduction to produce OH^- ions.



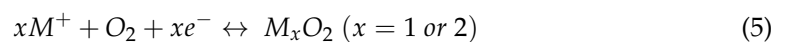
The produced OH^- ions move from the cathode to the metal anode, closing the loop. By combining Equations (1) and (2), the overall reaction can be derived [44].



Similarly, in non-aqueous MABs, the metal undergoes oxidation to form metal cations and electrons at the anode,



whereas, at the cathode, the metal cations react with O_2 and e^- to give metal oxides [45],



To quantify the performance of MABs, parameters like cell voltage, specific capacity, and energy density are used. These are crucial parameters for evaluating MAB performance. To calculate these metrics and gain a deeper understanding of MAB behavior, various formulas based on the underlying electrochemical reactions are utilized. Table 1 summarizes the formulae employed for calculating these key performance indicators of MABs.

Table 1. Key performance indicators and corresponding formulae for metal–air batteries.

Parameter	Formula	Units	Explanation	Ref.
Specific capacity	$C = \frac{(I \times t)}{m}$	mAh g ⁻¹	I is the discharge current, t is the discharge time, and m is the mass of the electrode	[78,79]
Capacity density	$Q = \frac{It}{\Delta m}$	mA cm ⁻²	I is the current in mA, t is the discharge time in hours, and Δm is the weight loss in g	[38]
Power density	$P = \frac{EI}{S}$	mW cm ⁻²	E is the average discharge voltage (V), I is the current in mA, and S is the active surface area in cm ²	[38]
Specific energy	$SE = \frac{V \times C}{M_B}$	Wh kg ⁻¹	SE is the specific energy, V is the nominal battery voltage in V, C is the rated battery capacity in Ah, and M _B is the battery mass	[80]
Energy density	$W = \frac{EIt}{\Delta m}$	mWh g ⁻¹	E is the average discharge voltage (V), I is the current in mA, t is the discharge time in hours, and Δm is the weight loss in g	[38]
Instantaneous specific energy (including oxygen)	$\frac{F \cdot \eta \cdot OCV}{3.6} \left[\frac{\ln(M_{M+O} / M_{Metal})}{M_{M+O} - M_{Metal}} \right]$	Wh kg ⁻¹	F is Faraday's constant, n is the number of electrons transferred per metal ion, OCV is the nominal voltage, M _{Metal} is the molar mass of metal anode, and M _{M+O} is the combined molar mass of metal anode and stoichiometric amount of oxygen that enters the battery	[50]
Energy density (including oxygen)	<i>Volumetric Energy Density</i> = (SE) · (OAD)	Wh L ⁻¹	SE is the specific energy in Whkg ⁻¹ and OAD is the oxidizing anode density in kgL ⁻¹	[50]
Nernst equation	$E = E^\circ - \frac{RT}{nF} \ln Q$	V	R is the gas constant, T is the temperature in K, F is Faraday's constant, n is the number of moles of electrons transferred, and Q is the reaction quotient	[81]
Gibbs free energy	$\Delta G^\circ = -nFE^\circ = \Delta H^\circ - T\Delta S^\circ$	J	T is the temperature in K, F is Faraday's constant, n is the number of moles of electrons transferred, S is the entropy, and H is the enthalpy	[81]
Current efficiency	$\eta_a = \frac{Q}{Q_0}$	%	Q is the actual capacity density in mAcm ⁻² and Q ₀ is the theoretical capacity density in mAhg ⁻¹	[38]
Energy efficiency	$\eta_{fuel} = \frac{W}{W_0} \times 100$	%	W is the actual energy density in mWhg ⁻¹ and W ₀ is the theoretical energy density in mWhg ⁻¹	[38]
Charging energy efficiency	$\eta_{charge} = \frac{\int_{SOC(0)}^{SOC(t)} U_{OCV} C_n d SOC}{\int_{SOC(0)}^{SOC(t)} U_{charge} C_n d SOC}$	%	Numerator = net energy; denominator = charge energy; SOC = state of charge; U = battery voltage; C _n = battery standard capacity	[81]

Table 1. Cont.

Parameter	Formula	Units	Explanation	Ref.
Discharging Energy efficiency	$\eta_{disch} = \frac{\int_{SOC(0)}^{SOC(t)} U_{disch} C_n d SOC}{\int_{SOC(0)}^{SOC(t)} U_{OCV} C_n d SOC}$	%	Numerator = discharge energy; denominator = net energy; SOC = state of charge; U = battery voltage; C _n = battery standard capacity	[81]
Charge-discharge Energy Efficiency	$\eta_{battery} = \frac{\int_{SOC(0)}^{SOC(t)} U_{disch} C_n d SOC}{\int_{SOC(0)}^{SOC(t)} U_{charge} C_n d SOC}$	%	Numerator = discharge energy; denominator = charge energy; SOC = state of charge; U = battery voltage; C _n = battery standard capacity	[81]
Vehicle Range	$R_V = \frac{E_B}{ECE_V \left(M_V + \frac{E_B}{SE_{BC}} \right)}$	km	E _B is the battery pack energy in Wh, ECE _V is the energy consumption efficiency of the vehicle in Wh km ⁻¹ kg ⁻¹ , M _V is the vehicle mass without a battery pack in kg, k _{m, B} is the battery mass overhead, and SE _{BC} is the specific energy of the battery cell in Whkg ⁻¹	[20]
Total Vehicle Cost	$C_{V,T} = C_V + C_B E_B$	USD	C _V is the vehicle cost without battery pack in USD and C _B is the battery pack cost in USD kWh ⁻¹	[19]
Battery Pack Volume	$Vol_B = \frac{E_B \times k_{vol,B}}{ED_{BC}}$	L	k _{vol,B} is the battery volume overhead and ED _{BC} is the energy density of the battery cell in WhL ⁻¹	[19]

MABs have a clear advantage in terms of energy storage capacity. When compared to a standard lithium/manganese dioxide (Li/MnO₂) battery with an assumed voltage of 3 V, MABs boast a much higher theoretical specific energy (Wh g⁻¹) and volumetric energy density (Wh cm⁻³). This is illustrated in Figure 5a,b, where the values for MABs are significantly greater. It is important to note that for rechargeable MABs (either electrically or mechanically), a more precise comparison would involve using data from discharged states. This is because the discharged material tends to be heavier and larger than its charged counterparts. Figure 5c,d showcase the theoretical energy storage potential including the discharged materials. Here, this potential is reduced as the by-products dissolve in the electrolyte. For comparison, the theoretical values for a common Li-ion battery (LiCoO₂) are 2.9 Wh cm⁻³ and 0.78 Wh g⁻¹, which in turn highlights the significant theoretical advantage of MABs for energy storage capacity. Accompanying this discussion is a comprehensive table that outlines the key theoretical parameters for each anode material, serving as a reference point for understanding the performance expectations of these technologies. In Table 2, specific energy values were determined by numerically integrating the oxygen uptake between the completely charged and completely discharged states of the battery. Volumetric energy densities were evaluated based on the anode density in its completely discharged state. The equations used to calculate the specific energy values are provided in Table 1. Refer to Supplementary Table S1 for further calculations and references. However, a significant drawback lies in the discharge behavior of MABs. Unlike Li-ion batteries, where electrode volume changes are minimal, the volume of MABs can increase by several tens of percent during discharge. This can pose challenges for their reusability. Interestingly, some MAB configurations can be manufactured pre-discharged (for instance, an anode built of metal oxide) and then activated through charging. The voltage output of MABs is typically stable and flat, reflecting a straightforward two-phase reaction between the metal anode and its products. The non-conductive nature of these discharged materials, compared to the highly conductive metals in their initial state, leads to voltage drops during discharge cycles [82–85]. Also, the presence of CO₂ in the ambient air poses several challenges. CO₂ reacts with the metal ions in the battery's cathode to form metal carbonates, which can block the active sites on the cathode, reducing the battery's efficiency and capacity. Additionally, the interaction between CO₂ and the electrolyte can lead to the formation of unwanted by-products, degrading the electrolyte and affecting the overall performance and lifespan of the battery. The presence of CO₂ also complicates the recharge process, as MABs using a mixture of O₂ and CO₂ as the active material in the cathode require specific measures to prevent electrolyte decomposition during recharge. Furthermore, the environmental impact of CO₂ in MABs is a concern, as the reactivity of CO₂ with the electrolyte and metal anode influences the discharge mechanism and stability, affecting the battery's overall environmental footprint [86,87].

To learn more about the potential and limitations of MABs, it is essential to explore the specific characteristics of each type of battery chemistry. While the general principles of MABs provide a foundational overview, the unique properties and performance metrics of individual MAB types are critical in determining their suitability for various applications, particularly in EVs. This detailed examination will not only highlight the distinct advantages and challenges associated with each type but will also provide valuable insights into their theoretical performance parameters. To facilitate this analysis, the following sections will delve into the specific MAB chemistries, beginning with Li–air batteries, to examine their design, functionality, and practical implications.

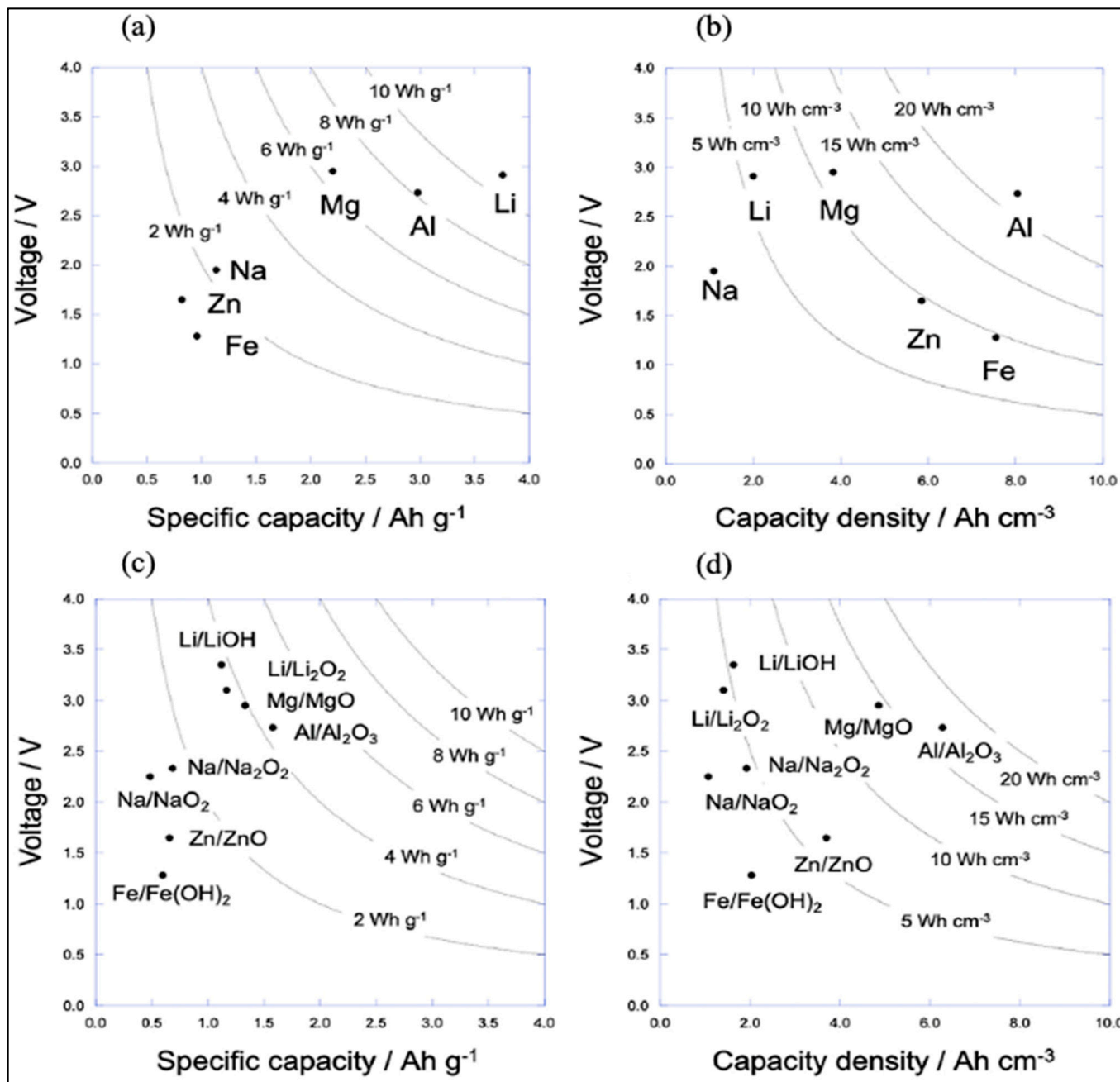


Figure 5. The metal’s mass and volume define the theoretical (a) specific energy and (b) volumetric energy density of MABs, whereas the plots (c,d) include the discharged products [82].

Table 2. Theoretical parameter comparison across various metal–air batteries.

Parameter	Li–Air	K–Air	Na–Air	Mg–Air	Al–Air	Zn–Air	Ca–Air	Fe–Air	Sn–Air	Si–Air	Ge–Air
Specific Energy (Wh kg ⁻¹)	5928	187	680	5238	5779	1218	3441	1080	768	5321	2214
Specific Power (W kg ⁻¹)	-	-	12–300	20–550	15–130	10–200	-	-	-	-	-
Specific Capacity (Ah kg ⁻¹)	2003	501	730	1695	2132	733	983.1	844	800	2548	1223
Volumetric Capacity density (Ah L ⁻¹)	2699	807	1072	3112	3817	3694	2164	2537	4944	3212	2633
Volumetric Energy Density (Wh L ⁻¹)	7989	1913	2466	9619	10347	6136	7574	3244	4747	6713	4766
Theoretical Open Circuit Voltage (V cell ⁻¹)	2.96	2.37	2.3	3.09	2.71	1.66	3.5	1.28	0.96	2.09	1.81
Energy Efficiency (%)	68–94	-	-	-	70	-	-	96	70–90	-	-
Operational Temperature Range (°C)	10–40	-	105–110	420–620	30–50	–20–70	-	-	-	-	-
Cost (USDkg ⁻¹)	46	13.02	1.7	11.02	2.866	3.351	5.93	0.4	28.66	4.19	1400

Refer to Supplementary Table S1 for the references and detailed calculations.

2.1. Lithium–Air Batteries

Lithium–air (Li–air) batteries were first conceptualized in 1976, though it was not until 1996 that Abraham et al. successfully demonstrated a practical Li–air battery using a non-aqueous electrolyte [88]. This technology has garnered significant attention due to its unique properties. Li–air batteries utilize lithium, the lightest element, and boast a remarkable theoretical specific energy. This value can reach $13,000 \text{ Wh kg}^{-1}$ calculated solely on the mass of lithium metal. However, considering the weight of the entire oxidized Li anode, the specific energy is still high at 5928 Wh kg^{-1} . Additionally, Li–air batteries possess an exceptional specific capacity of 2003 Ah kg^{-1} and operate at a voltage of 2.91 V [50,89–91]. Several Li–air battery architectures have been researched, including liquid electrolytes (aqueous and non-aqueous), hybrid systems (combining liquid and solid-state approaches), and the solid-state electrolyte system.

Driven by their high theoretical energy capacity and comparatively simpler construction, Li–air batteries with non-aqueous electrolytes have accumulated immense research effort [92–94]. These batteries (Figure 6) rely on Li metal for the anode and an air electrode that reacts with oxygen from the atmosphere. The components are isolated by a thin membrane, while an organic electrolyte enables the mobility of Li ions during operation. The reaction produces solid, insoluble Li_2O_2 as the discharge product and the corresponding reactions are shown in Table 3 [95,96]. Though these batteries possess substantial theoretical energy densities (3505 Wh kg^{-1} and 3436 Wh L^{-1}), they exhibit a high decomposition overpotential during the charging cycle. Additionally, during the discharge cycle, pore clogs of lithium oxide (Li_2O_2) within the cathode structure reduce the overall performance, and there is a necessity for pure oxygen as the fuel limiting the design configurations. Moreover, unfavorable side reactions are observed, stemming from reactions with water and carbon dioxide at both electrodes.

The aqueous Li–air battery (Figure 6) offers an alternative approach to the non-aqueous design. The electrolyte is placed in the cathode compartment to address safety concerns and prevent lithium from reacting with water. This battery also employs a special Li ion conducting separator between the anode and the electrolyte [97–99]. The reactions at the cathode differentiate between aqueous and non-aqueous Li–air batteries. This complexity arises from the dependence of these cathodic reactions on the electrolyte pH. At low pH (acidic environment), oxygen consumes H^+ ions to form water, while an alkaline environment promotes a reaction with H_2O to produce OH^- ions. This contrasting behavior significantly impacts the standard reaction potential (refer to Table 3 for the relevant reactions).

While the theoretical energy density of aqueous Li–air batteries (1910 Wh kg^{-1}) falls short of their non-aqueous counterparts (3505 Wh kg^{-1}), it still surpasses the energy potential of gasoline. However, the key strength of aqueous Li–air batteries lies in their inherent compatibility with atmospheric air. Unlike non-aqueous Li–air systems, where severe water contamination from the environment can occur, aqueous designs are less susceptible to this issue. Furthermore, the discharge product, LiOH , exhibits solubility within the aqueous electrolyte. This characteristic offers the potential for significantly reduced overpotential during the charging cycle and improved areal discharge capacity [100]. However, the lithium anode struggles with long-term stability, forcing efforts to maintain a neutral pH and minimize corrosion of the separator. Additionally, the battery's discharge capacity is reduced because of the limited conductivity of the separator at room temperature. While high temperatures can improve conductivity, they introduce other problems like electrolyte evaporation and higher corrosion rates. Furthermore, LiOH precipitation on the cathode during discharge hinders performance, requiring novel cathode designs with improved air channels [101–109]. By examining and comparing the pros and cons of both aqueous and

non-aqueous Li–air battery technologies, it becomes evident that despite their promising theoretical and practical aspects, they encounter substantial challenges that necessitate significant advancements before achieving widespread commercialization.

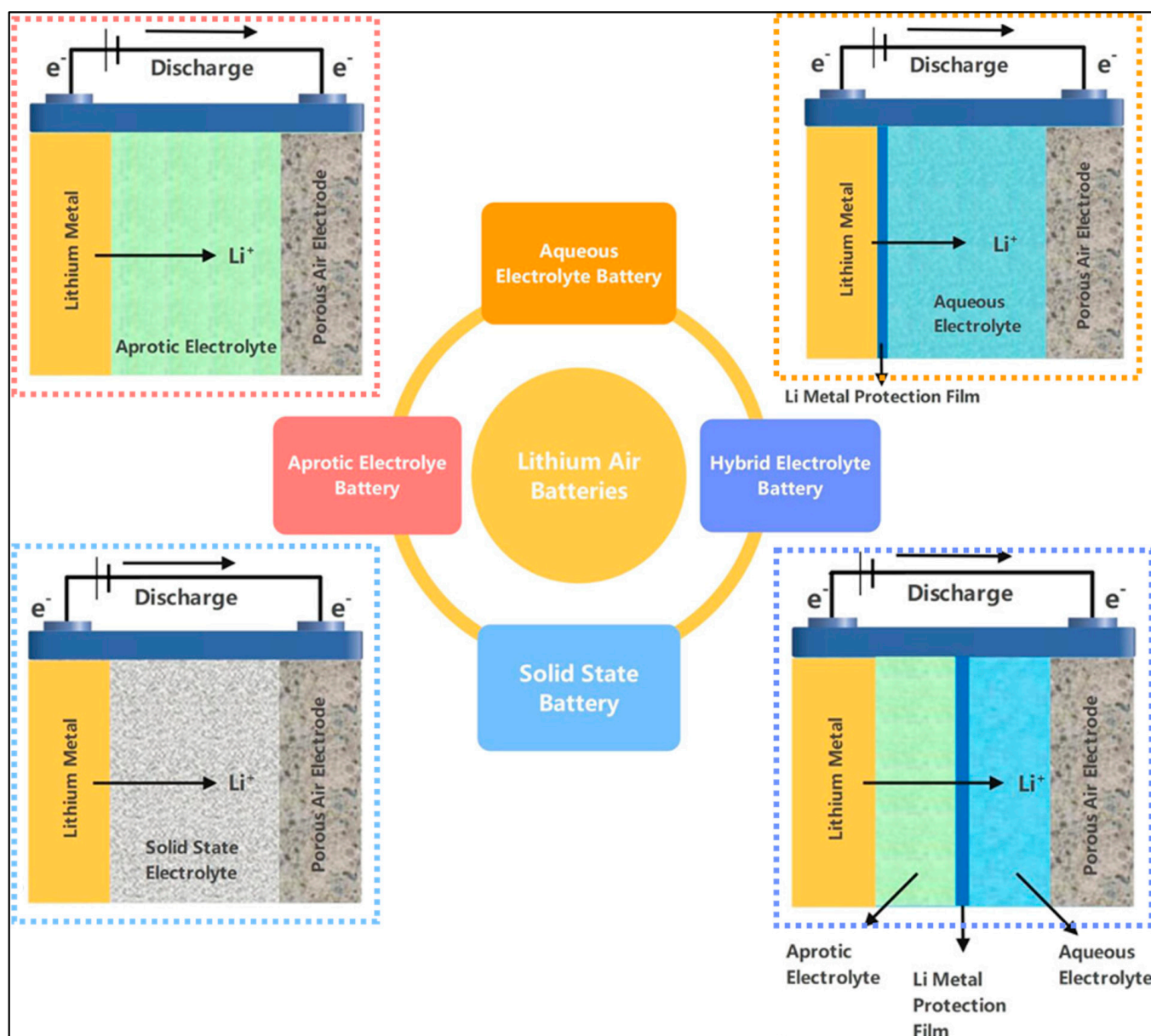


Figure 6. Classification of Li-air battery technologies with schematic representations. Modified from [91].

To address some of the above-mentioned limitations, a hybrid electrolyte system was put forward in 2010 [102,104]. This design combines a Li negative electrode in a non-aqueous electrolyte (organic) with an oxygen-reduction cathode in an aqueous electrolyte, separated by a LISICON (lithium superionic conductor) plate. This innovative strategy offers the potential to overcome some of the significant challenges plaguing conventional non-aqueous Li–air batteries. These challenges include lithium metal corrosion, Li_2O_2 product clogging of cathode pores, and the comparatively lower voltage output. By strategically separating the Li anode and the oxygen-reduction cathode using a LISICON plate, the hybrid system appears to circumvent these limitations [102,104]. However, a critical hurdle lies in the mechanical and chemical stability of the LISICON separator. For instance,

at higher pH levels, the corrosion rate of the LISICON plate accelerates, significantly compromising its stability and long-term performance within the battery. The Li dendrites developed during the charging of the battery negatively react with LISICON. Thus, the plate's durability decreases and has a short-term functionality within the battery system. Furthermore, developing low-cost, highly efficient carbon-based composite catalysts for these batteries remains a challenge [110].

Solid-state electrolytes present a paradigm shift in Li–air battery development, offering a confluence of higher energy density and safety. These solid-state Li–air batteries typically comprise three key components: an air cathode, an electrolyte, and a Li anode (as illustrated in Figure 6). Their exceptional mechanical strength and electrochemical stability enable the strategic integration of high-energy-density Li metal anodes and higher-potential cathode materials. This synergy unlocks the potential for significant advancements in energy density without compromising safety. Additionally, solid-state electrolytes simplify the manufacturing process due to their inherent ease of preparation, shaping, and large-scale production. This translates to streamlined battery management systems and potentially reduced production costs. Finally, the thermal stability and safety of solid electrolytes eliminate the need for intricate encapsulated cooling systems, further contributing to cost reductions and overall system optimization [111–113]. While solid-state electrolytes present a favorable avenue for futuristic Li–air batteries, their widespread adoption hinges on overcoming several critical limitations. A significant challenge lies in the inherently low electrolytic conductivity of many solid-state electrolytes, particularly at lower temperatures. This limitation directly impacts the battery's ability to charge and discharge efficiently. Furthermore, high interfacial resistance at the solid–electrolyte interface hinders the flow of ions, further compromising overall battery performance. Additionally, compatibility issues can arise between certain solid-state electrolytes (SSE) and Li metal cathodes, leading to degradation and a decline in performance over time. Finally, the weak physical stability observed in some electrodes can induce significant interfacial stress changes, ultimately contributing to mechanical failure and a shortened battery lifespan [114–116]. In recognition of the crucial role that solid-state electrolytes play in enabling efficient ionic transport between the anode and cathode, researchers [117–125] are diligently pursuing solutions to address the limitations. This multi-pronged approach encompasses advancements in SSE materials, cathode materials, and anode materials. Notably, optimizing the properties of SSEs remains a key factor in unlocking the utmost capability of solid-state Li–air batteries [126].

Table 3. Various metal anodes with electrolytes used in MABs: cell descriptions, electrode reactions, redox reactions, and electrochemical potentials.

Metal	Electrolyte	Cell Description	Reaction	Potential	Cell Reaction (Overall)	Refs.
Aluminum (Al)	Aqueous—Neutral	Anode: Aluminum Cathode: Air-breathing	Anode: $Al + 3H_2O \rightarrow Al(OH)_3 + 3H^+ + 3e^-$ Cathode: $O_2 + 4e^- + 2H_2O \rightarrow 4OH^-$	Anode: −1.47 V Cathode: 0.81 V	$Al + \frac{3}{4} O_2 + \frac{3}{2} H_2O \rightarrow Al(OH)_3$ (2.28 V)	[2,127,128]
	Aqueous—Alkaline	Anode: Aluminum Cathode: Air-breathing	Anode: $Al + 4OH^- \rightarrow Al(OH)_4^- + 3e^-$ Cathode: $O_2 + 4e^- + 2H_2O \rightarrow 4OH^-$ Side: $Al + 3H_2O + OH^- \rightarrow Al(OH)_4^- + \frac{3}{2} H_2$	Anode: −2.35 V Cathode: 0.39 V	$Al + \frac{3}{4} O_2 + \frac{3}{2} H_2O + OH^- \rightarrow Al(OH)_4^-$ (2.75 V)	[2,51,129]
	Aqueous—Acidic	Anode: Aluminum Cathode: Air-breathing	Anode: $Al \rightarrow Al^{3+} + 3e^-$ Cathode: $O_2 + 4e^- + 4H^+ \rightarrow 2H_2O$ Side: $Al + 3H^+ \rightarrow Al^{3+} + \frac{3}{2} H_2$	Anode: −1.66 V Cathode: 1.23 V	$Al + \frac{3}{4} O_2 + 3H^+ \rightarrow Al^{3+} + \frac{3}{2} H_2O$ (2.89 V)	[2]
	Organic Solvent Based: Solid-State Gel Polymer Electrolyte	Anode: Aluminum Cathode: Air-breathing (carbon and polymer-based) Electrolyte: PVA/LiCl polymer	Anode: $Al + 3OH^- \rightarrow Al(OH)_3 + 3e^-$ Cathode: $O_2 + 4e^- + 2H_2O \rightarrow 4OH^-$	Anode: −2.3 V Cathode: 0.81 V	$Al + 3H_2O \rightarrow Al(OH)_3 + 3H^+$ (3.31 V)	[2,130,131]
	Room Temperature Ionic Liquid (RTIL)-Based	Anode: Aluminum Cathode: Air-breathing Electrolyte: Aprotic room temperature ionic liquids	Anode: $Al + 7AlCl_4^- \rightarrow 4Al_2Cl_7^- + 3e^-$ Cathode: $H_2O_2 + 2H^+ + 2e^- \rightarrow 2H_2O$	Anode: −1.3 V Cathode: 0.695 V	$Al + 7AlCl_4^- + \frac{3}{2} H_2O_2 + 3H^+$ $\rightarrow 4Al_2Cl_7^- + 2H_2O$ (1.995 V)	[129,131–134]
Germanium (Ge)	Aqueous—Alkaline: 1–6 M KOH	Anode: Germanium wafers Cathode: Air-breathing Electrolyte: Aqueous KOH	Anode: $Ge + 4OH^- \rightarrow Ge(OH)_4 + 4e^-$ Cathode: $O_2 + 4e^- + 2H_2O \rightarrow 4OH^-$ Passivation: $Ge(OH)_4 \rightarrow GeO_2 + 2H_2O$	Anode: 1.0 V Cathode: 0.81 V	$Ge + O_2 + 2H_2O \rightarrow Ge(OH)_4$ (1.81 V)	[135]
Calcium (Ca)	Non-Aqueous—(Aprotic) Organic Electrolyte	Anode: Calcium Cathode: Air-breathing Electrolyte: Aprotic liquid	Anode: $Ca \rightarrow Ca^{2+} + 2e^-$ Cathode 1: $Ca^{2+} + 2O_2 + 2e^- \rightarrow Ca(O_2)_2$ Cathode 2: $Ca^{2+} + O_2 + 2e^- \rightarrow CaO_2$ Cathode 3: $Ca^{2+} + \frac{1}{2} O_2 + 2e^- \rightarrow CaO$	Anode: −2.368 V Cathode: varies	$Ca + 2O_2 \rightarrow Ca(O_2)_2$ (3.25 V) $Ca + O_2 \rightarrow CaO_2$ (3.28 V) $Ca + \frac{1}{2} O_2 \rightarrow CaO$ (3.13 V)	[136–138]
	Non-Aqueous— Ionic Liquid	Anode: Calcium Cathode: Carbon nanotube sheet Electrolyte: Ca salt in 1:1 EMIM-BF ₄ /DMSO solution	Anode: $Ca \rightarrow Ca^{2+} + 2e^-$ Cathode 1: $O_2 + 2Ca^{2+} + 4e^- \rightarrow 2CaO$ Cathode 2: $2O_2 + 2Ca^{2+} + 4e^- \rightarrow 2CaO_2$	Anode: −2.868 V Cathode: 0.715 V Cathode: 0.265 V	$O_2 + 2Ca \rightarrow 2CaO$ (3.583 V) $2O_2 + 2Ca \rightarrow 2CaO_2$ (3.133 V)	[131,139]
Iron (Fe)	Aqueous—Alkaline	Anode: Iron Cathode: Air-breathing Electrolyte: Basic media	Anode: $3Fe + 8OH^- \rightarrow Fe_3O_4 + 4H_2O + 8e^-$ Cathode: $O_2 + 4e^- + 2H_2O \rightarrow 4OH^-$ Side: $2H_2O + 2e^- \rightarrow H_2 + 2OH^-$	Anode: −0.88 V Cathode: 0.401 V	$3Fe + 2O_2 \rightarrow Fe_3O_4$ (1.28 V)	[140,141]
	Solid Oxide	Anode: Ni-Fe alloy Cathode: Ba _{0.6} La _{0.4} CoO ₃ Electrolyte: LSGM Fuel: Iron powder	Anode: $H_2 + O^{2-} \rightarrow H_2O + 2e^-$ Cathode: $\frac{1}{2} O_2 + 2e^- \rightarrow O^{2-}$ Iron Powder: $3Fe + 4H_2O \rightarrow Fe_3O_4 + 4H_2$	Anode: - Cathode: -	$3Fe + 2O_2 \rightarrow Fe_3O_4$ (0.97 V)	[142–146]

Table 3. Cont.

Metal	Electrolyte	Cell Description	Reaction	Potential	Cell Reaction (Overall)	Refs.
Lithium (Li)	Aprotic Solvent	Anode: Lithium Cathode: Porous carbon Electrolyte: Aprotic liquid	Anode: $Li \rightarrow Li^+ + e^-$ Cathode: $O_2 + Li^+ + e^- \rightarrow LiO_2$ Cathode: $LiO_2 + Li^+ + e^- \rightarrow Li_2O_2$ Cathode: $O_2 + 2Li^+ + 2e^- \rightarrow Li_2O_2$ Cathode: $Li_2O_2 + 2Li^+ + 2e^- \rightarrow 2Li_2O$ Cathode: $O_2 + 4Li^+ + 4e^- \rightarrow 2Li_2O$	Anode: -3.0401 V Cathode: varies	$O_2 + Li \rightarrow LiO_2$ (3.0 V) $LiO_2 + Li \rightarrow Li_2O_2$ (2.96 V) $O_2 + 2Li \rightarrow Li_2O_2$ (3.10 V) $Li_2O_2 + 2Li \rightarrow 2Li_2O$ (2.91 V) $O_2 + 4Li \rightarrow 2Li_2O$ (2.91 V)	[147–150]
	Aqueous—Acidic	Anode: Lithium Cathode: Air-breathing Electrolyte: Acidic media	Anode: $Li \rightarrow Li^+ + e^-$ Cathode: $\frac{1}{2}O_2 + 2e^- + 2H^+ \rightarrow H_2$	Anode: -3.0401 V Cathode: 1.229 V	$2Li + \frac{1}{2}O_2 + 2H^+ \rightarrow H_2O + 2Li^+$ (4.274 V)	[131,147,151]
	Aqueous—Alkaline	Anode: Lithium Cathode: Air-breathing Electrolyte: Basic media	Anode: $Li \rightarrow Li^+ + e^-$ Cathode: $\frac{1}{2}O_2 + H_2O + 2e^- \rightarrow 2OH^-$	Anode: -3.0401 V Cathode: 0.401 V	$2Li + \frac{1}{2}O_2 + H_2O \rightarrow 2LiOH$ (3.44 V)	[131,151]
Magnesium (Mg)	Aqueous—Neutral	Anode: Magnesium (or alloy) Cathode: Air-breathing Electrolyte: Saline	Anode: $Mg \rightarrow Mg^{2+} + 2e^-$ Cathode: $O_2 + 4e^- + 2H_2O \rightarrow 4OH^-$ Side: $2H_2O + 2e^- \rightarrow H_2 + 2OH^-$	Anode: -2.37 V Cathode: 0.81 V	$2Mg + O_2 + 2H_2O \rightarrow 2Mg(OH)_2$ (3.1 V)	[53,131]
Potassium (K)	K Salt Ether Solvent, Potassium Superoxide	Anode: Potassium Cathode: Air-breathing Electrolyte: Organic	Anode: $K \rightarrow K^+ + e^-$ Cathode: $O_2 + e^- \rightarrow O_2^-$	Anode: -2.931 V Cathode: -0.451 V	$K + O_2 \rightarrow KO_2$ (2.48 V)	[131,152]
Silicon (Si)	Non-Aqueous—RTIL: EMIm (HF) 2.3 F	Anode: Silicon Cathode: Air-breathing Electrolyte: Room temperature ionic liquids	Anode: $Si + 12(HF)_2F^- \rightarrow$ $SiF_4 + 8(HF)_3F^- + 4e^-$ Cathode: $O_2 + 12(HF)_3F^- + 4e^- \rightarrow$ $2H_2O + 16(HF)_2F^-$ SiO ₂ formation: $SiF_4 + 2H_2O + 4(HF)_2F^-$ $\rightarrow SiO_2 + 4(HF)_3F^-$	Anode: -2.71 V Cathode: 0.40 V	$Si + O_2 \rightarrow SiO_2$ (2.21 V)	[153]
	Aqueous—Alkaline: KOH	Anode: Silicon Cathode: Air-breathing	Anode: $Si + 4OH^- \rightarrow Si(OH)_4 + 4e^-$ Cathode: $O_2 + 4e^- + 2H_2O \rightarrow 4OH^-$	Anode: -2.71 V Cathode: -0.44 V Alternate: -0.38 V	$Si + O_2 + 2H_2O \rightarrow Si(OH)_4$ (2.09 V)	[153]
Sodium (Na)	Aqueous—Neutral	Anode: Sodium Cathode: Air-breathing Electrolyte: Saline	Anode: $Na \rightarrow Na^+ + e^-$ Cathode: $O_2 + 4e^- + 2H_2O \rightarrow 4OH^-$	Anode: -0.96 V Cathode: 0.33 V	$4Na + O_2 + 2H_2O \rightarrow 4NaOH$ (3.11 V)	[154]
	Aprotic Solvent	Anode: Sodium Cathode: Air-breathing	Anode: $Na \rightarrow Na^+ + e^-$ Cathode: $O_2 + e^- \rightarrow O_2^-$ Alternate Cathode: $O_2 + 2e^- \rightarrow O_2^{2-}$	Anode: -2.71 V Cathode: -0.44 V Alternate: -0.38 V	$Na + O_2 \rightarrow NaO_2$ (2.27 V) $2Na + O_2 \rightarrow Na_2O_2$ (2.33 V)	[154,155]
Tin (Sn)	Solid Oxide	Anode: Tin alloy Cathode: LSM/LSM-GDC Electrolyte: Ethylene glycol with tin powder (high temperature)	Anode: $Sn + 2O_2^{2-} \rightarrow SnO_2 + 4e^-$ Cathode: $O_2 + 2e^- \rightarrow O_2^{2-}$	Anode: -0.96 V Cathode: 0.33 V	$Sn + 2O_2 \rightarrow SnO_2$ (1.29 V)	[156,157]

Table 3. Cont.

Metal	Electrolyte	Cell Description	Reaction	Potential	Cell Reaction (Overall)	Refs.
Vanadium (Va)	Aqueous—Acidic	Anode: Zinc Cathode: Air-breathing Electrolyte: Acidic media	Anode: $V^{2+} \rightarrow V^{3+} + e^{-}$ Cathode: $VO_2^{+} + 2H^{+} + 2e^{-} \rightarrow VO^{2+} + H_2O$	Anode: -0.26 V Cathode: 1.0 V	$V^{2+} + VO_2^{+} + 2H^{+} \rightarrow V^{3+} + VO^{2+} + H_2O$ (1.26 V)	[158,159]
	Vanadium—Oxygen Fuel Cell	Anode: Vanadium Cathode: Oxygen diffusion electrode	Anode: $V^{2+} \rightarrow V^{3+} + e^{-}$ Cathode: $O_2 + 4e^{-} + 4H^{+} \rightarrow 2H_2O$	Anode: -0.26 V Cathode: 1.23 V	$4V^{2+} + O_2 + 4H^{+} \rightarrow 4V^{3+} + 2H_2O$ (1.49 V)	[143]
Zinc (Zn)	Aqueous—Neutral	Anode: Zinc Cathode: Air-breathing Electrolyte: Any neutral media	Anode: $Zn \rightarrow Zn^{2+} + 2e^{-}$ Cathode: $O_2 + 4e^{-} + 2H_2O \rightarrow 4OH^{-}$	Anode: -0.762 V Cathode: 0.817 V	$2Zn + O_2 + 2H_2O \rightarrow 2Zn(OH)_2$ (1.579 V)	[160]
	Aqueous—Alkaline	Anode: Zinc Cathode: Air-breathing Electrolyte: Any basic media	Anode: $Zn + 2OH^{-} \rightarrow ZnO + H_2O + 2e^{-}$ Cathode: $O_2 + 4e^{-} + 2H_2O \rightarrow 4OH^{-}$	Anode: -1.26 V Cathode: 0.40 V	$2Zn + O_2 \rightarrow 2ZnO$ (1.66 V)	[50,161]
	Non-Aqueous: Protic Room Temperature Ionic Liquids	Anode: Zinc Cathode: Air-breathing Electrolyte: Protic room temperature ionic liquid	Anode: $Zn \rightarrow Zn^{2+} + 2e^{-}$ Cathode: $O_2 + 2H^{+} + 2e^{-} \rightarrow H_2O_2$	Anode: -0.7618 V Cathode: 0.695 V	$Zn + O_2 + 2H^{+} \rightarrow Zn^{2+} + H_2O_2$ (1.457 V)	[131,162]

2.2. Zinc–Air Batteries

Zinc–air (Zn–air) batteries currently hold the distinction of being the sole commercially available metal–air battery technology worldwide. Their extensive history underscores their efficacy in low-current, long-duration applications such as hearing aids. Early prototypes of Zn–air batteries date back to the 1870s. Advancements in electrode design soon followed, paving the way for the primary Zn–air batteries onto the market in the 1930s, ultimately leading to their widespread adoption in hearing aids by the 1970s [163,164]. While zinc exhibits a lower specific capacity (733 Ah kg^{-1}) compared to certain alternative metals investigated for MABs (e.g., lithium and aluminum), it continues to demonstrate a notable performance. This is evidenced by its impressive theoretical specific energy and energy density as mentioned earlier. Furthermore, Zn–air batteries boast high anode utilization and compatibility with alkaline electrolytes. This compatibility offers a distinct advantage, as the comparatively slower reaction rate between the alkaline electrolyte and zinc minimizes hydrogen evolution, a significant challenge encountered in other metal–air chemistries (like Al- and Mg-based MABs). These properties position them as strong contenders in the development of next-generation portable, flexible electronics, and in the electrification of automobiles [163,165–168]. Zn–air batteries can be broadly classified into primary, mechanically rechargeable, and electrically rechargeable types. A typical primary Zn–air cell comprises several key components such as a zinc anode, a separator, an electrolyte, and an air cathode [169]. Mechanically rechargeable Zn–air batteries operate as functionally similar to primary batteries, relying on replacing the Zn anode and electrolyte during recharge. This distinct characteristic necessitates the use of only ORR electrocatalysts at the cathode [170]. Commercially proven primary Zn–air batteries, known for their high energy density, are used in power hearing aids (in the form of button cells) and even telecommunications and satellite systems in prismatic pouch formats. One key challenge associated with primary or replenishable primary Zn–air batteries is the potential for electrolyte evaporation. This evaporation can disrupt ionic conductivity within the battery, ultimately leading to performance degradation [171–174].

Rechargeable Zn–air batteries come in various arrangements, differing in their electrolyte types and design configurations. The most common design, depicted in Figure 7a, utilizes a simple “sandwich” framework with four key components. The first is a zinc anode. The second component, the air electrode, incorporates bifunctional oxygen electrocatalysts, a gas diffusion layer (GDL), and a current tab. Finally, the design is completed by a liquid electrolyte and a separator. This configuration allows for easy assembly in research labs using readily available materials like rubber gaskets, steel or plastic plates, and chambers.

Although planar Zn–air batteries can be arranged either horizontally or vertically, the vertical configuration is preferred to avoid electrolyte evaporation issues and ensure better ionic connectivity. While commercially available rechargeable Zn–air batteries are not yet widespread, their simple design offers potential advantages for EVs and other applications, owing to their high energy density and lightweight properties. In contrast, the planar design can lead to challenges, such as electrolyte loss in horizontal setups, which hampers the commercial viability of these batteries [172,174,175].

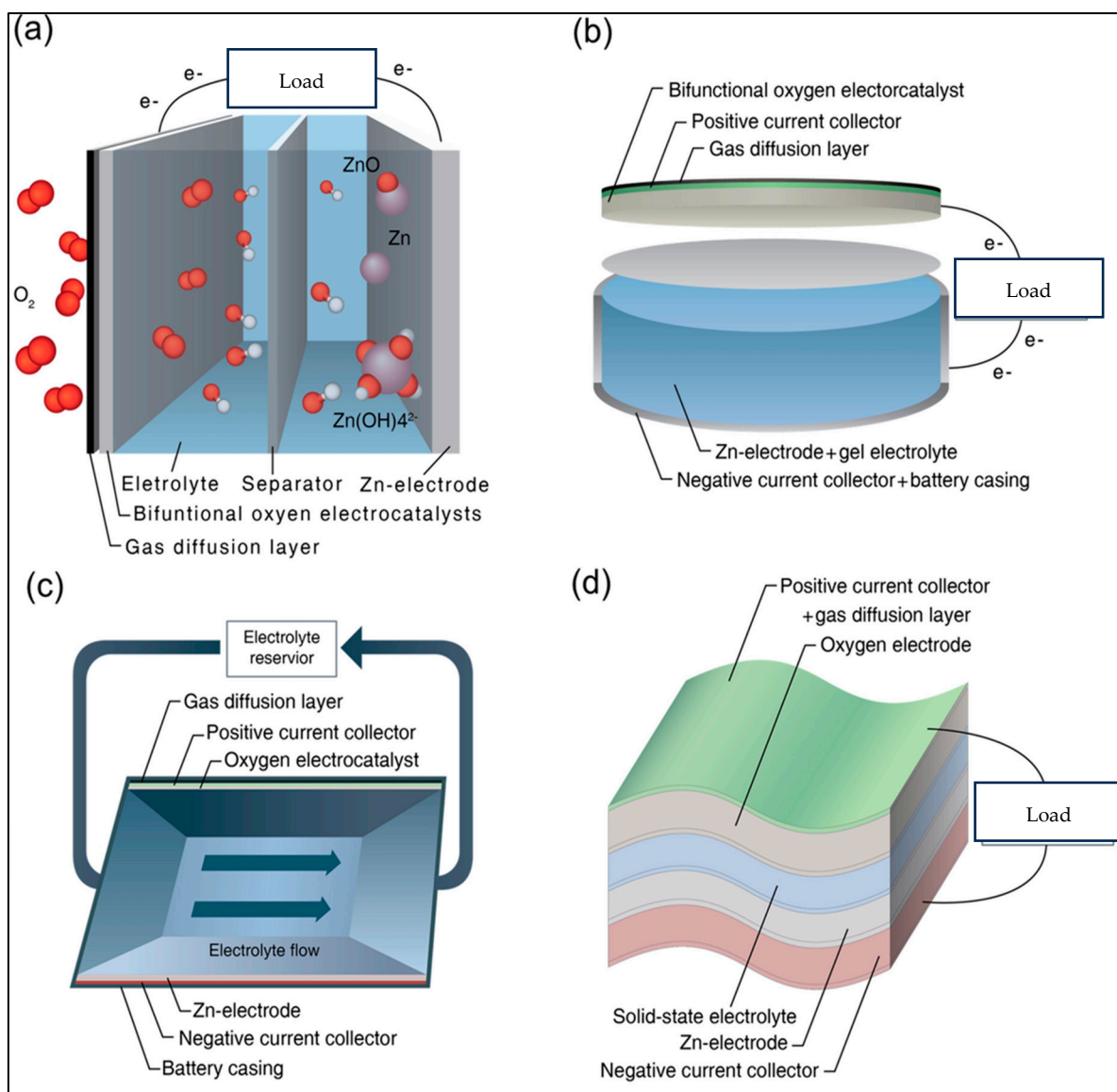


Figure 7. Rechargeable Zn-air battery designs: (a) Planar architecture with aqueous electrolyte. (b) Planar architecture with gel electrolyte. (c) Electrolyte flow-through design. (d) Flexible configuration (adapted from [176]).

Building on the foundational principles of conventional planar Zn-air batteries, the planar gel electrolyte architecture shown in Figure 7b represents an advanced iteration that addresses electrolyte evaporation loss and enhances efficiency using gel polymer electrolytes (GPEs). GPEs possess properties intermediate between liquid and solid states. Notably, they have high ionic conductivity (10^{-4} to 10^{-3} S cm⁻¹ at ambient temperature), flexibility, and efficient electrolyte retention. As ionic conductors and separators, GPEs facilitate ion transport through a mechanism similar to liquid electrolytes. Despite significant advancements in GPEs, they still face challenges in making Zn-air batteries suitable for consumable electronics and EVs. Alkaline GPEs tend to generate carbonates which diminishes battery reversibility. Given the ongoing research into electrolytes, further advancements are essential to address these limitations [177,178].

A Zn-air flow battery (Figure 7c) utilizes a circulating electrolyte design to enhance performance and mitigate degradation issues associated with both the anode and cathode. On the metal anode side, the larger volume flowing electrolyte improves the current distribution and reduces concentration gradients, which helps to prevent shape change,

dendrite formation, and passivation. The precipitated carbonate layer on the cathode can be washed away by the flowing electrolyte and removed using an external filter. This design is comparable to the approach utilized in alkaline fuel cells, where circulating electrolytes are employed to prevent carbonate precipitation on the cathode surface. Consequently, rechargeable Zn–air flow batteries are expected to offer a longer cycle life compared to traditional static electrolyte configurations. However, Zn–air flow batteries also come with certain disadvantages. The increased complexity of the system, which includes the need for pumps, tubing, and circulating the electrolyte, results in decreased energy efficiency. Additionally, the excess volume of electrolytes and the associated components lead to lower specific and volumetric energy density [179–182].

A Zn–air flexible battery (Figure 7d) is an innovative power source designed to be flexible, making it suitable for various applications such as wearable technology. They are preferred due to their cost-effectiveness, high energy density, and intrinsic safety, which obviates the need for a rigid protective casing. Many studies are exploring methods and materials to produce flexible Zn–air batteries, including thin-film “wearable” designs, cylindrical cable-type batteries, and biocompatible flexible batteries. The key challenge in developing flexible Zn–air batteries is their exposure to the air, making the use of liquid electrolytes undesirable due to risks of evaporation or leakage onto sensitive electronic equipment. Consequently, current research efforts are centered on developing a solid-state electrolyte that is mechanically flexible, durable, and exhibits adequate ionic conductivity. Additionally, the electrodes and other cell components must be capable of withstanding and maintaining operation under significant bending. Despite these challenges, the advantages of flexibility, safety, and high energy density make Zn–air flexible batteries a promising choice for future energy storage solutions [183–186].

2.3. Aluminum–Air Batteries

Aluminum–air batteries (Al–air) have been the subject of extensive research since the 1960s. The concept of utilizing an Al anode was initially introduced by Zaromb in 1962 within the context of an Al/O₂ system renowned for its high energy density. Subsequent research has explored various applications, such as EVs, military communications, and unmanned aerial and underwater vehicles. A significant advancement occurred in 2016, creating a 100 kg Al–air stack battery capable of extending an EV’s range beyond 3000 km. This achievement underscores the substantial potential of Al–air technology for the transportation sector [187]. Al–air batteries offer a cutting-edge energy storage approach due to aluminum’s high volumetric capacity, abundance, and low cost. Typically, these primary batteries consist of an Al metal anode, an air cathode, and an aqueous electrolyte, which is often sodium chloride (NaCl), potassium hydroxide (KOH), or sodium hydroxide (NaOH). Additionally, AABs include components such as external loads, pumps, anolyte and catholyte chambers, current collectors, separators, membranes, and electronic systems, with configurations varying by design. Aluminum is oxidized at the negative electrode by hydroxide ions during discharge, producing aluminate ions and electrons. Simultaneously, O₂ from the air is reduced at the air cathode by these electrons, and hydroxide ions migrate through the electrolyte to maintain charge balance [188–191]. The corresponding reactions with various electrolyte types are summarized in detail in Table 3.

Al–air batteries exhibit diverse configurations, varying in both electrolyte composition and design structure. As depicted in Figure 8a, a planar structure refers to a flat, layered design where the components of the Al–air battery are arranged in flat sheets stacked either vertically or horizontally. Three types of aqueous electrolytes are used based on their pH: neutral, acidic, and alkaline electrolytes. Neutral Al–air batteries are eco-friendly, utilizing non-toxic raw materials and generating non-hazardous by-products. The generated OH[−]

during the operation quickly combines with aluminum ions to form aluminum hydroxide, keeping the electrolyte neutral. This neutrality offers a high level of safety to Al–air batteries, making them suitable for marine and consumer applications. Since the 1970s, large neutral Al–air battery stacks (Figure 8b) have been developed for marine use, leveraging seawater as a natural electrolyte. This allows offshore Al–air batteries to operate with only aluminum plates and air cathodes, as seawater can be utilized directly as an electrolyte. Neutral Al–air batteries have seen applications in consumer products, including wearable devices, small electronics, and other household appliances. However, these batteries are hindered by significant challenges, such as the intense polarization of the Al anode due to the passivation of the aluminum surface. This passivation layer impedes the migration of aluminum ions and electron transfer, reducing the battery’s discharge performance. The presence of chloride ions can help to reduce polarization by assisting in the dissolution of the oxide film [192].

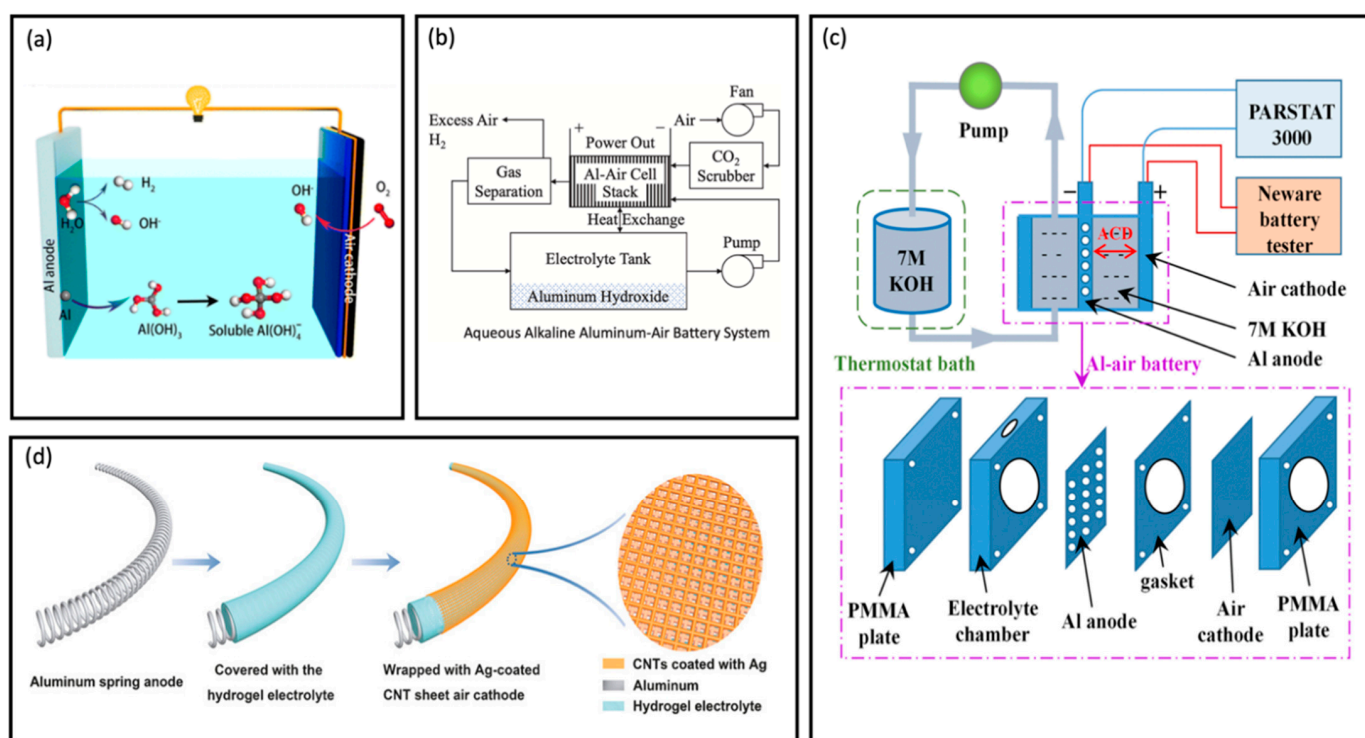


Figure 8. Al–air battery configurations: (a) Planar architecture with aqueous electrolyte [192]. (b) Al–air battery stack architecture [51]. (c) Electrolyte flow-through design [38]. (d) Flexible configuration [193].

To combat the disadvantages of anode passivation in neutral electrolytes, acidic electrolytes were proposed. Hydrochloric acid (HCl) and sulphuric acid (H₂SO₄) have been studied as possible options, offering the potential for higher voltages due to the high theoretical positive potential of the air cathode in low-pH environments. However, the aluminum anode’s thermodynamic properties in acidic electrolytes are unsatisfactory, with severe H₂ evolution side reactions occurring alongside the main reaction. The time needed for the disintegration of the oxide film in lower concentrations of acidic electrolytes is higher than in alkaline electrolytes, leading to longer activation processes and increased polarization. Moreover, acidic electrolytes can cause pitting corrosion, which is detrimental to smooth discharge. These practical limitations have hindered the usage of acidic electrolytes in Al–air batteries, though ongoing research aims to address these issues [194–196].

The introduction of alkaline electrolytes marked a breakthrough for Al–air batteries. KOH or NaOH-based electrolytes, quickly disintegrate the passivation layer on the aluminum, greatly increasing the kinetics of the charge transfer reactions. Insoluble aluminum hydroxide is converted into soluble tetrahydroxy aluminate ions, reducing polarization, and maintaining high ionic conductivity. Alkaline Al–air batteries can maintain high voltages under high current densities due to the intense destructive capacity of hydroxide ions on the oxide film, facilitating smoother ion mobility at the solid-electrolyte interface at the anode. However, alkaline electrolytes also have inherent flaws. The reactive aluminum is exposed to the electrolyte as the passivation layer dissolves during discharge, leading to hydrogen evolution, which poses safety risks and reduces the energy density and specific capacity of the battery. Although high-concentration electrolytes and additive compounds are used to mitigate these issues, the actual anode potential in alkaline solutions remains lower than the theoretical value, indicating significant anode polarization [38,197]. Despite these challenges, alkaline Al–air batteries show promise for vehicle power supplies. Phinergy developed an electric car combining Al–air batteries and Li-ion batteries, extending the range of the Li-ion batteries from 60 km to 350 km [198]. Recently, a short-range aircraft powered by Al–air batteries was designed, showcasing significant advantages in weight and cost with a theoretical 950 nautical miles of mileage [199]. The primary barrier to commercialization lies in high anodic corrosion and complicated stack design. Many effective options to inhibit self-corrosion are studied, but achieving easy mechanical charging, simple, and safe replacement of aluminum anodes and electrolytes remains crucial for industrialization.

Al–air flow batteries (Figure 8c) employ an electrolyte flow system to remove reaction by-products, thereby improving energy efficiency. This design leads to exceptional electrochemical performance, including excellent discharge capabilities and extended cycle life. There are two primary methods for facilitating electrolyte flow in Al–air flow batteries: external mechanical pump-assisted driving and paper-based capillary action driving. The mechanical pump-assisted method, utilizing devices like peristaltic or syringe pumps, ensures a fast and stable electrolyte flow, significantly enhancing the performance of Al–air flow batteries. However, the bulky and complex structure of this system makes it suitable only for large-scale applications. To reduce size and complexity, researchers have developed a paper-based microfluidic Al–air battery. In this system, the solution flow is driven by capillary action within the microchannels of cellulose paper. This approach offers a compact and simplified design but comes with limitations such as reduced energy storage capacity and shorter battery shelf life, resulting in weaker discharge behavior compared to their larger counterparts [67,200]. Wen et al. [38] reported significant results using an Al–air flow battery with a 7 M KOH electrolyte flowing externally. They reached a peak power density of 545 mW cm^{-2} in a pure O_2 environment, with optimal performance parameters including a 0.5 mm anode-cathode distance (physical distance between the two electrodes to prevent short-circuit), an operating temperature of $60 \text{ }^\circ\text{C}$, and an electrolyte flow rate of 15 mL min^{-1} . The battery demonstrated an anode efficiency of 96.2% and energy efficiencies of 44.4% in air and 42.6% in pure O_2 . Furthermore, their research indicated that the technology can be scaled to kilowatt-level packs, with energy densities of 700 Wh L^{-1} and 900 Wh kg^{-1} , making it promising for applications in EVs and large-scale energy storage systems. Huang et al. developed a novel acoustofluidic saltwater Al–air flow battery that uses ultrasonic vibrations to drive the electrolyte flow and create an ultrasonic field within the reaction chamber. This innovative approach led to a peak power density of 43.88 mW cm^{-2} , which is up to 7.5 times higher than that with static electrolytes and comparable to mechanical pumping systems. The optimization of reaction vessel thickness, ultrasonic vibration velocity, and electrolyte concentration contributed to this performance

enhancement. Additionally, the acoustofluidic system significantly decreased the energy usage, mass, and size of the electrolyte-driven component compared to traditional methods. This research highlights the potential of ultrasonic pump-based Al–air flow batteries for energy storage applications requiring eco-friendliness, cost efficiency, safety, and stable discharge performance [201].

A flexible Al–air battery (Figure 8d) is an advanced type of battery designed to offer both high energy density and mechanical flexibility. Unlike traditional rigid batteries, flexible Al–air batteries are constructed to be pliable and stretchable, allowing them to be integrated into various applications such as smart textiles and wearable electronics. Xu et al. [193] presented a fiber-shaped flexible Al–air cell with notable advantages and performance. This design achieved an impressive energy density of 1168 Wh kg^{-1} , over 12 times greater than fibrous Li-ion batteries, and a specific capacity of 935 mAh g^{-1} , about 6 times higher than fiber-type zinc-carbon batteries. It maintained an output voltage above 1 V even when stretched by up to 30%, demonstrating excellent mechanical stability. The fiber design also allows for integration into textiles, making it suitable for flexible and wearable electronics. Key advantages include its environmental friendliness and the usage of a porous design with aligned carbon nanotubes and silver nanoparticles to enhance performance. However, practical energy density remains lower than theoretical values due to limitations in electrode materials, and there are concerns about the aluminum anode's self-corrosion and the complexity of the manufacturing process. Despite these challenges, the battery offers promising potential for innovative applications in smart textiles and wearable technology.

2.4. Magnesium–Air Batteries

In 1966, Carson and Kent conducted conceptual and practical investigations into high-performance magnesium–air (Mg–air) primary cells, termed the “Magair” cell. This system employed an air cathode, a Mg alloy anode, and a neutral salt electrolyte, achieving a nominal voltage of 1.60 V. During discharge, the cell exhibited voltages of 1.30 V and 1.00 V at current densities of 10 and 60 mA cm^{-2} , respectively. The authors also demonstrated the concept of mechanical rechargeability through periodic replenishment of the anode and electrolyte salt [202]. While Mg–air batteries have received comparatively less attention than other MAB technologies, their potential as energy storage systems is compelling due to magnesium's abundance and the battery's high theoretical energy density. Moreover, when considering practical performance metrics, Mg–air batteries exhibit competitive advantages over Zn–air and Al–air technologies. Since their inception in the 1960s, studies on Mg–air cells have been mostly centered around the primary, or reserve-type, configurations. These batteries require activation before use and offer continuous discharge until anode depletion. Conversely, developing rechargeable Mg–air batteries has proven significantly more challenging [203].

In general, Mg–air batteries face several hurdles, including low working voltage and practical specific energy, substantially below theoretical values. These limitations stem largely from sluggish oxygen-reduction kinetics and anode corrosion, common challenges in MAB systems. Magnesium's unique corrosion behavior, exacerbated by impurities, further complicates the issue. Unlike most metals, magnesium exhibits a negative difference effect, where increasing cathodic current accelerates hydrogen evolution. Additionally, the poor conductivity and electrochemical activity of discharge products (MgO and MgO_2) hinder rechargeability [204]. Figure 9 illustrates various configurations of Mg–air batteries, categorized by cell architecture and electrolyte types.

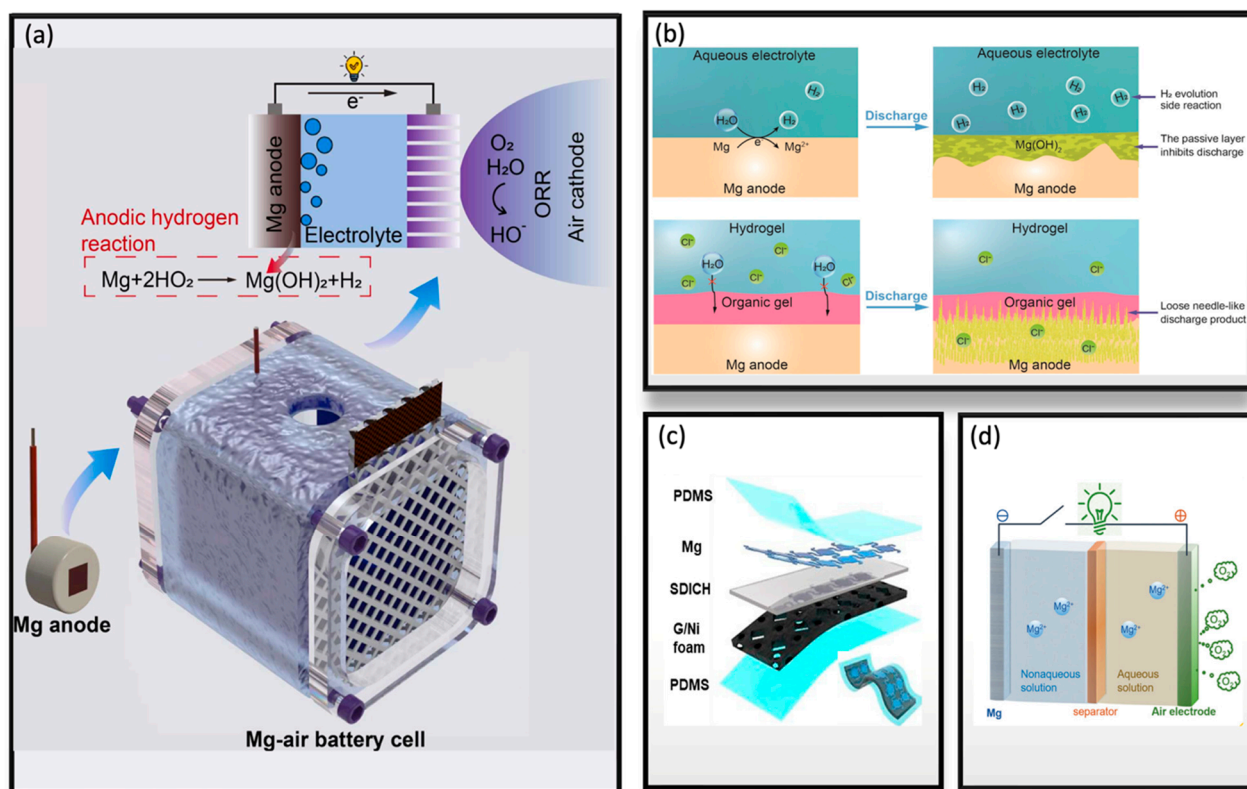


Figure 9. Mg-air battery configurations: (a) Planar architecture with aqueous electrolyte [205]. (b) Two-layer gel electrolyte structure [206]. (c) Flexible configuration [207]. (d) Hybrid electrolyte design [208].

Chen et al. [205] devised a planar structure utilizing ultra-high-purity (UHP) Mg-Ge anodes for Mg-air cells, enhancing their performance significantly as shown in Figure 9a. The inclusion of Ge in the anode composition improves anodic reaction activity while effectively suppressing the anode hydrogen evolution reaction (HER). The electrolyte utilized in this system is a 3.5 wt. % NaCl solution, which facilitates ion transport during the electrochemical processes. The UHP Mg-0.5Ge anode possessed an impressive cell voltage of 1.69 V at a current density of 0.5 mA cm^{-2} during discharge and achieved a high energy density of 2272 mWh g^{-1} at 20 mA cm^{-2} . These performance metrics surpass those of all previously researched Mg-based anodes. Moreover, the low content of impurity and the formation of a Ge-bearing surface layer results in a remarkable 95% discharge efficiency. This is 3.5 times greater than that of the frequently used AZ31 anode. Thus, the advantages include enhanced discharge characteristics and improved battery efficiency due to the low impurity content and a Ge-bearing surface film as mentioned. However, potential disadvantages may arise from the corrosive nature of the NaCl electrolyte, which might impact the longevity of the cell components, alongside the complexities associated with manufacturing high-purity materials, raising concerns about cost and scalability. Overall, the exceptional properties of the UHP Mg-Ge anode pave the way for significant advancements in Mg-air batteries.

Li et al. [206] employ a two-layer gel electrolyte structure that addresses significant performance limitations associated with Mg anodes. The architecture consists of a Mg anode, an air-breathing cathode, and a two-layer gel electrolyte as described in Figure 9b. The two layers built of an organic gel and hydrogel were evenly coated on the surface of the anode. The two-layer serves two primary functions: the first layer prevents corrosion of the Mg anode, while the second layer inhibits the development of a thick, insoluble passive layer that forms on the Mg's surface during discharge and corrosion processes. This design

enables effective interaction between the Mg anode and the electrolyte, facilitating the battery's operation. The working mechanism involves the reaction of Mg with water in the electrolyte, producing magnesium hydroxide and releasing H₂ gas, with electrons being transferred directly to the electrolyte. Key results from this study indicate that these Mg–air batteries achieved an impressive specific capacity of 2190 mAh g⁻¹ based on the anode alone and an anode efficiency of 99.3%, alongside an energy density of 2282 Wh kg⁻¹ based on the Mg anode and air electrode. The dual-layer architecture presents several advantages, including enhanced battery performance, improved efficiency, and high utilization of the Mg anode. However, the design also has drawbacks, such as increased complexity in the cell's design and potential concerns regarding the long-range stability of the gel electrolyte in various environmental conditions.

The architecture of the cell is based on a completely flexible Mg–air battery that employs dual-ion-conducting hydrogels (SDICH) as illustrated in Figure 9c. This design allows for significant mechanical flexibility and stretchability, making it suitable for integration into biomedical devices. The materials used include a Mg anode, an air-breathing cathode, and an SDICH electrolyte. This combination produces electricity while maintaining the necessary flexibility and stretchability for biomedical applications. The battery successfully powered 120 light-emitting diodes (LEDs) for over 5 h, demonstrating its capacity and efficiency. It exhibited stable electrical output even under mechanical stretching, indicating resilience to deformation without performance degradation. The biocompatibility of the battery was validated through *in vitro* and *in vivo* studies, showcasing its ability to be used in medical applications. The stretchable design allows the battery to be integrated into wearable and flexible devices, making it safe for use in biomedical applications, particularly in systems that are in contact with human tissue, such as wound dressings. However, the long-term stability of the dual-ion-conducting hydrogel under various environmental conditions may require further investigation. Additionally, the production of such advanced materials and architectures may be more complex and costly compared to simpler battery designs [207].

Hybrid electrolyte Mg–air batteries (Figure 9d) use both aqueous and non-aqueous electrolytes to improve the electrochemical reactions within the battery. This approach improves the characteristics of traditional Mg–air batteries by enhancing charge transport reactions, reducing polarization effects, and enabling recharging capabilities. Hybrid electrolyte Mg–air batteries offer several advantages. They can achieve up to 90% round-trip efficiencies, making them an attractive option for energy storage solutions. Their enhanced power density results from the integration of materials that facilitate fast charge transport and high current density. Furthermore, the design of hybrid electrolytes contributes to a longer battery lifespan by addressing issues such as self-corrosion and passivation of the Mg anode. However, there are notable disadvantages such as the Mg's self-corrosion which can produce insulating products like MgO and impede battery performance by increasing overpotential and polarization. Additionally, parasitic reactions that produce hydrogen gas can disrupt the pressure balance within sealed cells, further increasing cell polarization. Thus, hybrid electrolytes carry inherent disadvantages, along with the complexity of managing both aqueous and non-aqueous components and the need for advanced electrocatalysts for effective oxygen reduction. These factors can reduce the operational stability of the batteries, impacting their overall efficiency and longevity [204].

2.5. Sodium–Air and Potassium–Air Batteries

Sodium–air (Na–air) and potassium–air (K–air) batteries demonstrate substantial energy densities in contrast to other battery technologies. Na–air batteries offer a specific energy of 1680 Wh kg⁻¹ and a volumetric energy density of 2466 Wh L⁻¹, while K–air

batteries exhibit a specific energy of 1187 Wh kg^{-1} and a volumetric energy density of 1913 Wh L^{-1} . These impressive figures underscore the significant potential of sodium- and potassium-based systems for future energy storage applications. However, despite concerted research efforts during the last few decades, advancements in the research area of alkali MABs remain in their early stages. Peled et al. [209] introduced the theories of Na-air batteries in 2011. This initial cell configuration employed a liquid sodium anode, a polymer electrolyte, and a commercial air cathode. To prevent sodium metal buildup on the air electrode, the system was run at a high temperature of $105 \text{ }^\circ\text{C}$ to $110 \text{ }^\circ\text{C}$, exceeding sodium's melting point. Ren et al. [70] first illustrated the idea of a K-O₂ battery in 2013, showcasing decreased overpotentials by leveraging the reversibility of the O₂/O₂⁻ redox couple. For the first time, they reported a charge/discharge potential gap smaller than 50 mV at a current density of 0.16 mA cm^{-2} . Raman analyses and XRD verified the generation and decomposition of KO₂ during the battery cycle test. In the literature, K-air and K-O₂ batteries are often used interchangeably, but most research has been conducted with oxygen, with few works reported on dry ambient air [210].

Among the various types of Na-air cells, hybrid electrolyte and organic electrolyte Na-air cells have been the most extensively studied. These two types differ primarily not only by the electrolyte type but also by their structural designs. Organic Na-air batteries constitute one primary research focus within the broader Na-air battery field. Their fundamental architecture, as depicted in Figure 10a, centers around a Na anode, a porous bifunctional catalyst cathode, and an organic electrolyte-saturated separator.

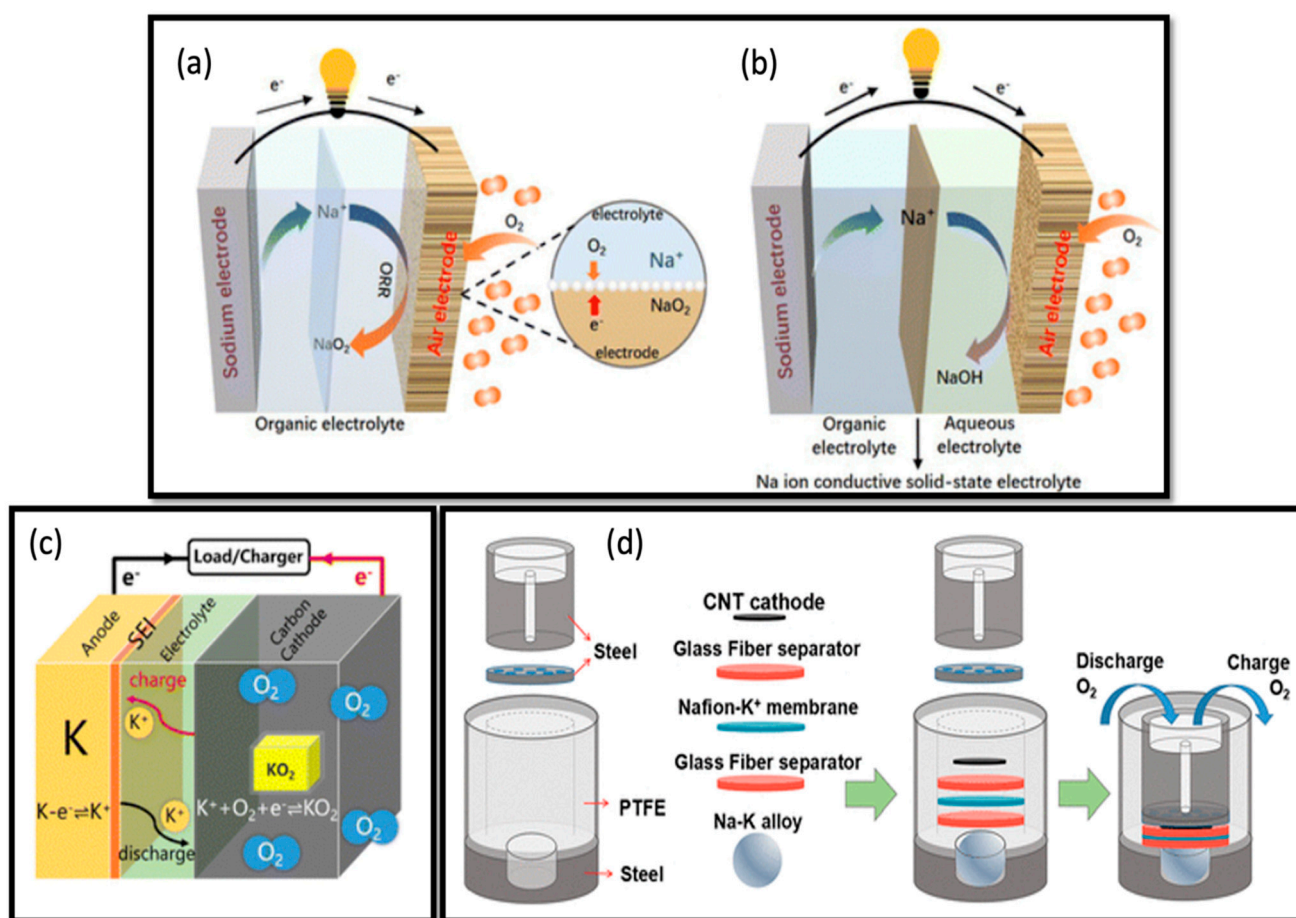


Figure 10. Graphical depiction of the operational mechanisms and cell configurations of the following cells: (a) Na-air cell with organic electrolyte [211], (b) Na-air cell with hybrid electrolyte [211], (c) planar K-O₂ cell [212], (d) K-O₂ cell with Na-K alloy anode [213].

A range of organic solvents like dimethyl ether (DME) and diethylene glycol dimethyl ether (DEGDME), along with salts such as sodium hexafluorophosphate (NaPF_6) and sodium bis(trifluoromethanesulfonyl)imide (NaTFSI), are used to modulate battery performance. The specific salt and its concentration significantly impact the battery's overall efficacy. Functionally akin to Li-O_2 due to the chemical parallels between sodium and lithium, organic Na-air batteries excel in lower overpotential and have a superior cycling stability [214–216].

In contrast, hybrid Na-air batteries come in a wide variety of designs, going beyond conventional structures. As shown in Figure 10b, they incorporate a dual-electrolyte system: an aqueous electrolyte at the anode and an organic electrolyte at the cathode, separated by a sodium ion-conductive solid electrolyte membrane, often NASICON ($\text{Na}_3\text{Zr}_2\text{Si}_2\text{PO}_{12}$). This configuration shields the anode from oxidative reactions while facilitating unidirectional sodium ion migration. The cathode electrolyte mirrors that of organic Na-air batteries, while the anode typically employs an aqueous NaOH solution. The energy storage mechanism in hybrid Na-air batteries is simpler, involving oxygen uptake and release at the positive electrode during the discharge and charge operations. This process corresponds to the ORR and OER, respectively. A key advantage of this design is the generation of a single discharge product, NaOH, which minimizes side reactions and enhances cycle life. Moreover, the solubility of NaOH in the electrolyte prevents accumulation on the air cathode, further improving efficiency. Unlike their organic counterparts, hybrid Na-air cells can function with atmospheric air and exhibit higher theoretical voltages. Both organic and hybrid Na-air batteries hold promise for diverse applications. However, they present distinct advantages and drawbacks. Organic Na-air batteries prioritize safety due to sodium's reactivity with water, but they suffer from higher costs, environmental concerns associated with organic electrolytes, and performance limitations caused by discharge product deposition. Additionally, they necessitate dry oxygen and gas purification systems, increasing operational expenses. In comparison, hybrid Na-air battery systems exhibit lower overpotentials, higher energy densities, and extended cycle life. Their ability to utilize ambient air and dissolve discharge products in the cathode electrolyte renders them more cost-effective and efficient. Consequently, hybrid Na-air batteries emerge as a compelling alternative to their organic counterparts [154,217–220].

Yu et al. [213] successfully showcased a novel K-O_2 battery that is dendrite-free operating at room temperature, utilizing a liquid Na-K alloy as the negative electrode, a Nafion- K^+ membrane separator, and a 0.5 M potassium hexafluorophosphate (KPF_6) in DEGDME electrolyte sandwiched between glass fibers and carbon nanotubes (CNTs) as the cathode (Figure 10b). The cathode is made of porous carbon paper coated with carbon nanotubes. The primary discharge product is KO_2 , with some KOH also formed, demonstrating the efficacy of the Na-K alloy anode. Without the Nafion- Na^+ membrane, the battery possesses a discharge capacity of around 2.0 mAh and an initial voltage of approximately 2.45 V. However, the Nafion membrane's ion selectivity restricts K^+ diffusion, hindering discharge capacity in Na- O_2 cells. This configuration offers advantages like dendrite-free operation, effective anode performance, and reduced side reactions due to the Nafion membrane. Nevertheless, it suffers from limited discharge capacity due to ion selectivity, solvent decomposition, and sustainability concerns as the battery transitions from Na- O_2 to K- O_2 during discharge.

2.6. Other Metal–Air Batteries

In the realm of MABs, the utilization of semiconductors as anodes has opened new avenues for energy storage. Among these, silicon-air (Si-air) batteries are particularly noteworthy with a theoretical volumetric energy density of 6713 Wh L^{-1} and a specific

energy of 5321 Wh kg^{-1} . The pioneering Si–air battery, developed by Cohn et al. [221] in 2009, maintained a consistent voltage between 1.0 and 1.2 V. This innovative design featured doped silicon wafers as the fuel, an air-breathing cathode, and a precisely engineered ionic liquid, 1-ethyl-3-methylimidazolium trifluoroborate ($\text{EMI} \cdot (\text{HF})_2 \cdot 3\text{F}$), as the electrolyte. Recent research has concentrated on aqueous Si–air batteries utilizing conventional KOH electrolytes. Initial research emphasized the importance of micro- or nano-porous Si surfaces to maintain extended discharge times, achieving up to 30 h at 0.05 mA cm^{-2} [222,223]. Without these surface modifications, the cell voltage drops sharply due to the formation of the passivation layer on the Si surface rapidly. The following studies demonstrated longer discharge times of up to 270 h at the same current density using a refill-type cell setup with an unmodified Si anode. In cases where a thicker Si wafer (3 mm) was employed as the anode, the alkaline Si–air battery, utilizing a 5 M KOH electrolyte, sustained operation for up to 1100 h at voltages above 1.1 V, delivering specific capacities of 115 mAh g^{-1} and anode mass conversion efficiencies around 3% [224]. More recent research has shown that reducing the KOH concentration to 0.5 M enhances Si anode utilization during discharge, with conversion efficiencies increasing to as much as 9% [225]. In 2024, Guerrero et al. [226] pioneered a study using both alkaline and non-aqueous Si–air batteries to power low-power transient electronics designed for partial self-destruction. The Si–air batteries demonstrate practical specific capacities and energies of 117 mAh g^{-1} and 123 Wh kg^{-1} for the alkaline system, and 1072 mAh g^{-1} and 841 Wh kg^{-1} for the non-aqueous system, until the active area of the Si anodes is fully consumed (Figure 11a). Nevertheless, Si–air batteries have several drawbacks. The silicon surface can quickly become passivated, causing a drop in voltage unless modified with micro- or nano-porous structures. The batteries also face mechanical stress due to silicon’s expansion and contraction during use, which can shorten their lifespan. Additionally, the electrolyte can be consumed during reactions, leading to corrosion. Production costs are high because of the need for pure silicon and specialized processes. Si–air batteries also have a shorter cycle life and can be less energy-efficient [227].

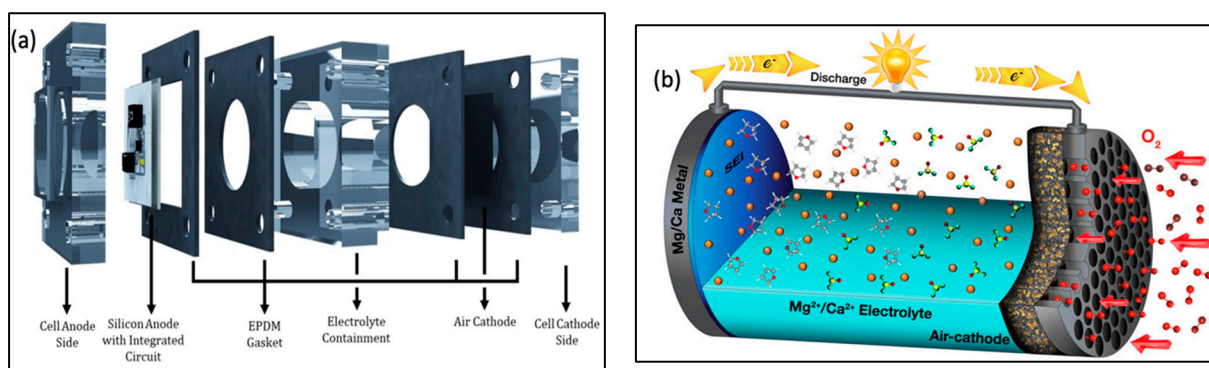


Figure 11. (a) Cell structure of a Si-air battery [226]. (b) Working illustration of a Mg/Ca-O₂ battery [228].

Germanium–air (Ge–air) batteries emerged shortly after Si–air batteries in 2013, described by Ocon et al. [229], leveraging germanium’s widespread use in Li-ion batteries. The cell featured a nanoporous Ge anode, a KOH electrolyte, and an air-breathing cathode. It operated at a sustained discharge and maintained a stable cell voltage of 0.42 V, with a power density of 0.21 mW cm^{-2} and a current density of 0.5 mA cm^{-2} . Remarkably, there were no signs of polarization, even at elevated current densities, as evidenced by the slight increase in potential after 200 h of operation. However, since their introduction, there have

been very few advancements in research on Ge–air batteries, and they remain a relatively unexplored area in the field.

The calcium–oxygen (Ca–O₂) battery presents a favorable avenue for rechargeable energy storage. These batteries are attractive due to their impressive theoretical volumetric energy density of 7574 Wh L⁻¹, specific energy of 3441 Wh kg⁻¹, and incredibly high nominal voltage of 3.5 V. This electrochemical system employs a calcium anode and an air-breathing cathode, where O₂ is reversibly converted to calcium peroxide. An ionic liquid-based electrolyte, consisting of EMIM-BF₄ and dimethyl sulfoxide, provides a stable operating environment. Recent studies have highlighted the exceptional performance of Ca–O₂ batteries, including their longevity (700 recharge cycles), stability in ambient air, and adaptability to flexible textile formats for wearable applications [230]. Lu et al. [228] introduced the concept of Mg/Ca–O₂ where a Mg/Ca metal is used as the anode. They conducted a comprehensive analysis of suitable electrolytes and identified key technological advancements required to address the challenges associated with this type of battery (Figure 11b). Challenges such as anode passivation and calcium ion transport limitations are yet to be addressed. Ca–O₂ batteries are in their initial research phase, and it will take considerable time and effort to realize their full potential.

The pioneering work on iron–air (Fe–air) batteries was first conducted by NASA in 1968. This concept was later adopted by the Swedish National Development Corporation in the 1970s to produce a 30 kWh battery for traction applications, achieving an energy density of 80 Wh/kg at a 5 h discharge rate [141]. Fe–air batteries boast several advantages over traditional batteries. Theoretically, they possess a volumetric energy density of 3244 Wh L⁻¹, a specific energy of 1080 Wh kg⁻¹, and an OCV of 1.28 V. Notably, in Fe–air batteries, the risk of iron dendrite formation during charging is eliminated, ensuring safety and longevity. Furthermore, the iron negative electrode offers a remarkably high theoretical specific capacity of 960 mAh g⁻¹, promising exceptional energy density [231]. Finally, their composition and operational characteristics make it a more environmentally friendly and sustainable energy storage solution with many recent works to solve the issues associated with this battery type.

In conclusion, while various MABs offer unique advantages such as high energy density and potential cost savings, their inherent complexity and current technological limitations make them unsuitable as stand-alone power sources in the context of the EV industry. Instead, their most promising application lies in being used as range extenders in EVs, where they can supplement existing battery systems and enhance driving range without the need for complete reliance on their performance. This hybrid approach maximizes their benefits while mitigating challenges related to efficiency, safety, and cost. To fully understand their potential, however, further study of practical experimental parameters is necessary to assess their viability in real-world applications.

3. Comparison of Performance Metrics

According to the International Energy Agency's (IEA) global EV outlook released in 2024, electric car sales continue to rise and could reach approximately 17 million in 2024, making up more than one in five cars sold globally and the pricing strategies of car manufacturers will perform a key role in increasing affordability, along with the rate at which EV battery prices decrease as evidenced by the trends shown in Figure 12. Under current projections, EV energy demand is expected to increase significantly by 2035. By 2030, demand could grow up to 4.5 times compared to 2023, and nearly 7 times by 2035. In more ambitious scenarios, demand may rise 5 to 7 times by 2030, and 9 to 12 times by 2035. For context, in 2035, the weekly EV battery demand could match the total annual demand

recorded in 2019 [232]. These demands emphasize the importance of integrating MABs that offer higher specific energy, lower costs, and improved safety in the EV industry.

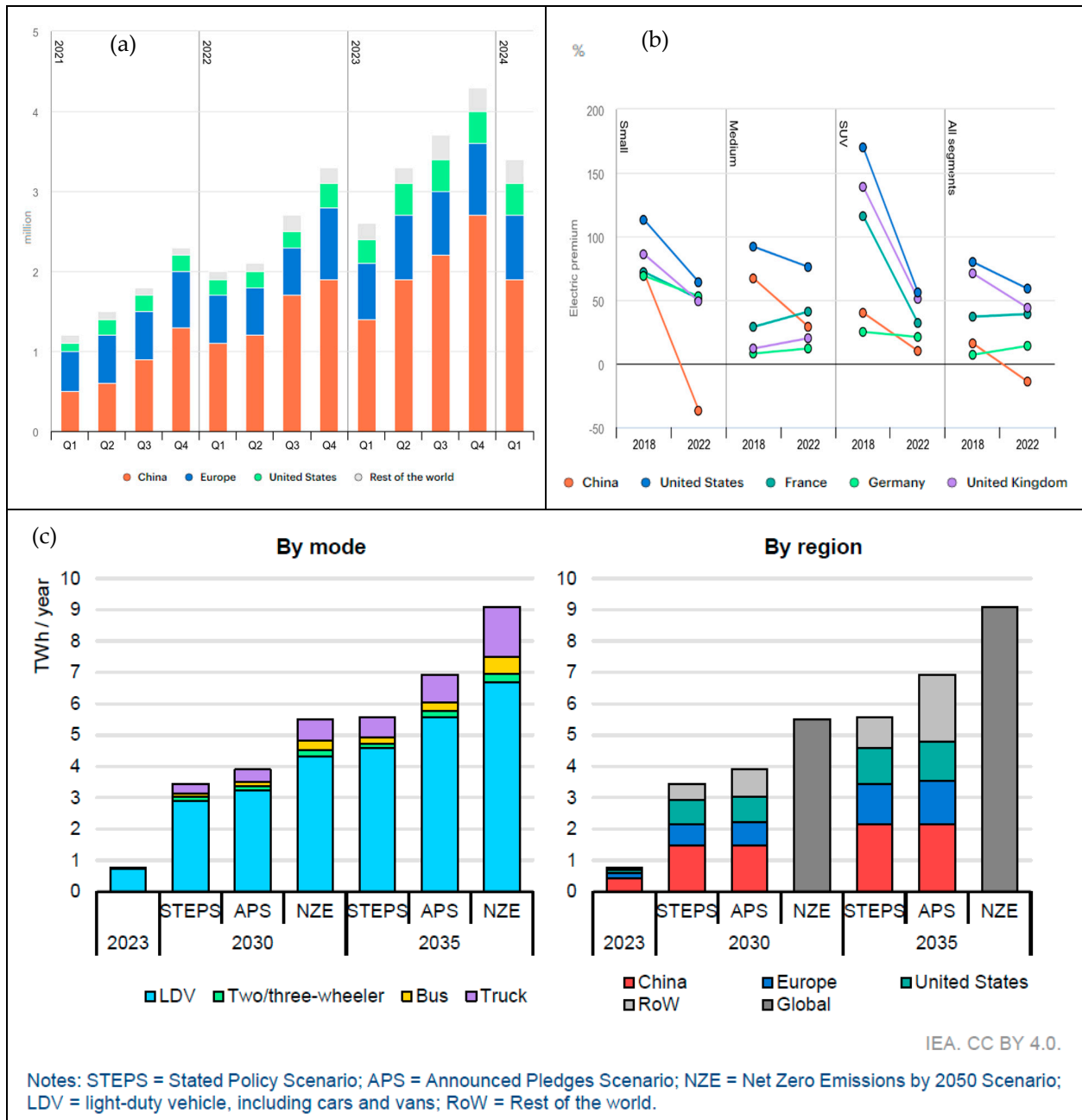


Figure 12. (a) Regional quarterly electric car sales (2021–2024), (b) the difference in sales-weighted average prices between traditional and electric vehicles in specific countries, before subsidies, by vehicle size (2018–2022), and (c) energy demand for electric vehicles, categorized by mode and region (2023–2035) [232].

As mentioned before, studying practical performance metrics is crucial as they provide real-world insights into the efficiency and limitations of MABs, beyond what theoretical parameters can predict. Thus, Figure 13 compares the practical characteristics of various MABs to better understand the potential of these candidates for next-generation EVs, alongside those of Li-ion batteries. The data are compiled from the latest literature showcasing the practical value ranges at the cell level, whereas the energy storage cost is shown as the price of a battery pack or system level. Safety ratings for various battery types are determined qualitatively on a scale of 1 to 10, with 1 being the least safe and 10 being the

safest, based on factors like the risk of toxic material release, overheating, and electrolyte flammability. Li-ion, Li-air, and Zn-air batteries are rated directly based on these criteria, while other MAB types are evaluated by comparing their properties to those of the known Li-ion, Li-air, and Zn-air batteries. Adjustments are made to account for differences in metal reactivity, electrochemical properties, and cell components.

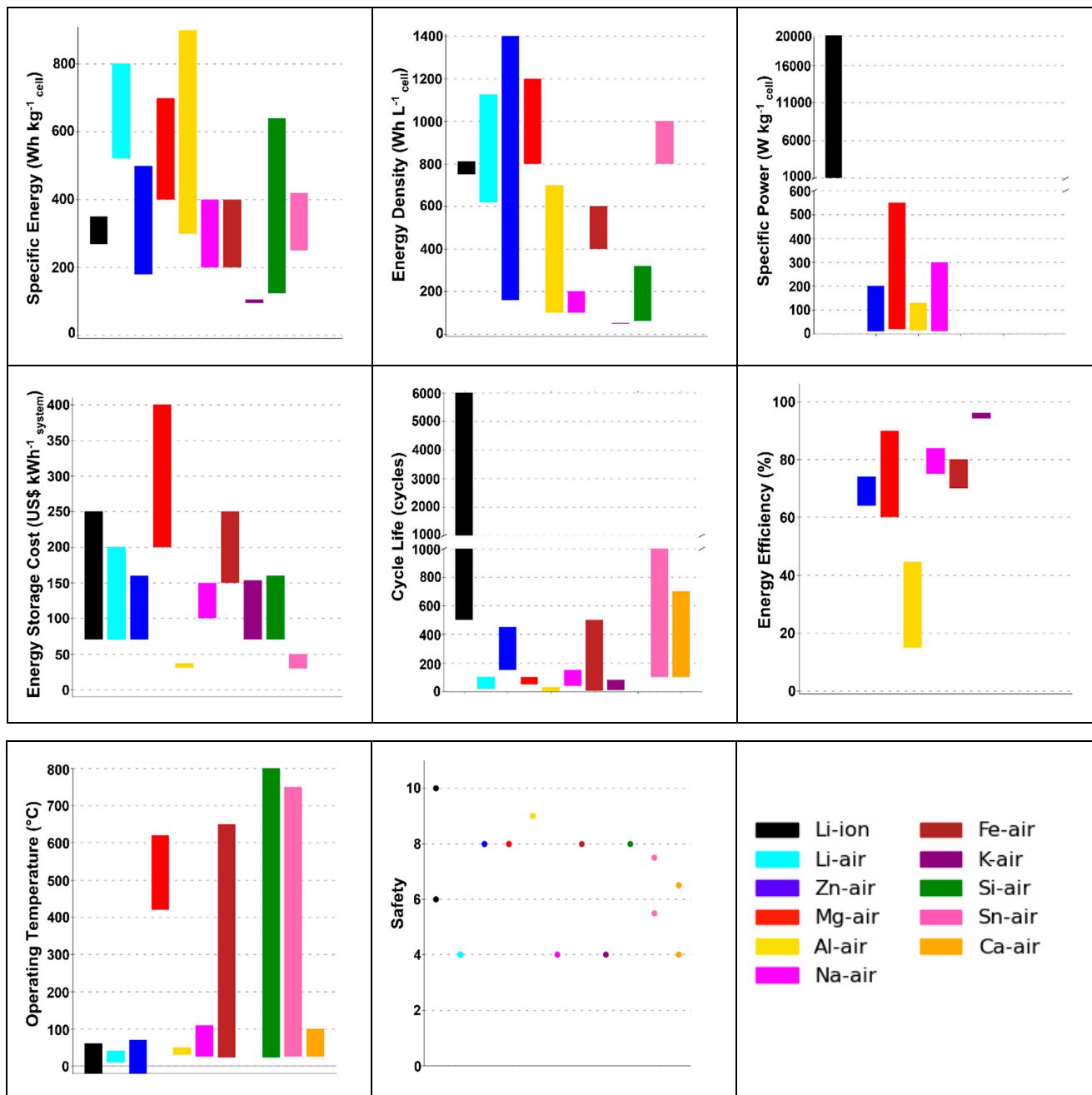


Figure 13. Comparative characteristics of various MABs and Li-ion cells. The data represent the practical value ranges at the cell level, derived from the existing literature. (For detailed references, see Supplementary Table S3).

This approach provides a logical framework for assigning relative safety values. Li-ion batteries have a variable safety profile, with ratings ranging from 6 to 10, indicating that their safety can vary significantly depending on specific conditions or configurations. Certain MABs show higher safety ratings, with Al-air batteries (aqueous electrolytes) rated at 9 and other types (Zn-air, Mg-air, Fe-air, and Si-air) rated at 8. Practical evaluation of

certain battery metrics, such as energy storage cost, energy density, and specific energy, as shown in Figure 14, can be achieved by approximating their influence on the battery pack volume (Vol_B), total vehicle cost ($C_{V,T}$), and vehicle range (R_V). These metrics are directly correlated with the battery pack's energy (E_B) and can be calculated using the equations adapted from [20] and shown in Table 1. The overhead factors in Supplementary Table S3 quantify the necessary safety and air management equipment for each battery type, especially for MABs. This estimation approach for battery system mass overhead and battery system volume overhead uses comparative analysis based on the known properties of Li–air and Zn–air batteries and adjusts them according to the specific characteristics of other MABs such as the density of the metal used, packing efficiency, electrochemical properties, and cell components.

3.1. Cycle Life, Efficiency, and Safety Evaluation

Li-ion batteries, being a well-established and widely used technology, offer a highly balanced profile with their excellent cycle life (1000–6000) and consistently high energy efficiency (95%). Analyzing the capabilities of MABs and their effectiveness as range extenders is significantly shaped by their cycle life, energy efficiency, and safety profile. Zn–air batteries offer a balanced compromise with a cycle life ranging from 150 to 450 cycles and efficiency between 64% and 74%. This makes them a viable option as a range extender, given their moderate performance in both longevity and energy efficiency. In comparison, Fe–air batteries achieve a slightly higher maximum cycle life of up to 500 cycles and an efficiency of 80%. However, their relatively lower energy density and specific energy results in an unfavorable trade-off for a range extender. Among relatively high-efficiency, mechanically rechargeable batteries with a moderate cycle life, Li–air and Al–air batteries stand out. Currently, Li–air batteries offer up to 100 cycles (electrically rechargeable), while Al–air batteries exhibit efficiencies as high as 45%. Both types show impressive energy metrics and driving range, demonstrating significant potential. However, further research and development are needed to standardize these battery designs and address their current limitations. For enhanced safety in hybrid vehicles, Al–air and Zn–air batteries are preferable to Li–air, as seen from the safety profile. K–air batteries, while boasting a high efficiency of 94.2–96.1% but a poor cycle life of 8–80 cycles, also fall short in other key energy metrics, making them unsuitable for range-extending applications in the near term. Similarly, Na–air batteries, with their moderate cycle life and efficiency, also present less favorable trade-offs. Meanwhile, Si–air, Sn–air, and Ca–air batteries lack sufficient data for immediate application but could offer unique advantages or potential for future use as research and technology progress. (See Supplementary Table S3 for references to the numeric data discussed here.)

3.2. Cost Considerations

Figure 14 illustrates results for three vehicle categories: a mini vehicle (Figure 14a,b), typically found in markets that prioritize affordability; a mid-size vehicle (Figure 14c,d), prevalent in markets emphasizing range; and a semi-trailer truck (Figure 14e,f), representing heavy-duty applications. Figure 14a,c,e show the vehicle cost as it relates to the driving range, plotted until the battery volume surpasses the designated space limit within each vehicle. For the mini-vehicle, the vehicle cost is USD 10,000, with a mass of 650 kg and an energy consumption efficiency of $0.08 \text{ Whkm}^{-1}\text{kg}^{-1}$. For the mid-size vehicle, the vehicle cost is USD 25,000, with a mass of 1500 kg and an energy consumption efficiency of $0.06 \text{ Whkm}^{-1}\text{kg}^{-1}$; and the semi-trailer truck has a vehicle cost of USD 100,000, a mass of 24,000 kg, and an energy consumption efficiency of $0.0334 \text{ Whkm}^{-1}\text{kg}^{-1}$. These curves use midpoint values for battery system overhead ranges, energy storage cost, volumetric energy

density, and specific energy (Supplementary Table S3). In Figure 14b,d,f, the cost of adding range per km is plotted against the vehicle's range. The curves are generated by calculating the tangents of the respective curves from Figure 14a,c,e. While these plots illustrate the inherent capability of each battery type to reduce costs and extend the driving range, the analysis does not consider factors such as power metrics, electric grid compatibility, self-discharge rate, cycle life, efficiency, and safety (as discussed in Section 3.2), which are essential for reliable operation in an electric vehicle. Na-air, K-air, and Si-air batteries have significant drawbacks due to their low energy densities, resulting in limited driving range extensions. Their cost per additional range is still greater than that of Li-air, Zn-air, and Al-air batteries, which offer comparable driving ranges at a significantly lower cost than Li-ion batteries across all three vehicle types. With the equipment to safeguard against atmospheric carbon dioxide and moisture, the utmost volumetric energy density of Li-air batteries at the vehicle level is projected to be only 384 WhL^{-1} . This volumetric limitation hinders their ability to achieve significantly longer driving ranges compared to Li-ion batteries [233]. On the flip side, Zn-air batteries, offering lower costs and greater range than Li-air batteries, are favored by researchers for forthcoming EVs because of their superior practical energy density [45,50]. Despite their potential, substantial improvements in energy efficiency, specific power, and cycling stability are necessary for the successful integration of Zn-air batteries, into electric vehicles in a dual-battery configuration. While Al-air batteries offer the lowest cost per additional kilometer, their low energy efficiency and complex mechanical recharge design may hinder their adoption. However, the combination of attributes such as low cost and high safety could indirectly boost range by powering auxiliary units, reducing the load on the main battery. The Fe-air battery has the second-highest cost for additional range, only surpassed by Mg-air. Although Mg-air batteries provide a driving range comparable to Li-ion batteries, their cost is significantly higher, exceeding what the average EV customer might expect to pay. Unless the estimated cost for both Fe-air and Mg-air is substantially reduced, these batteries may not be suitable for high-usage EVs.

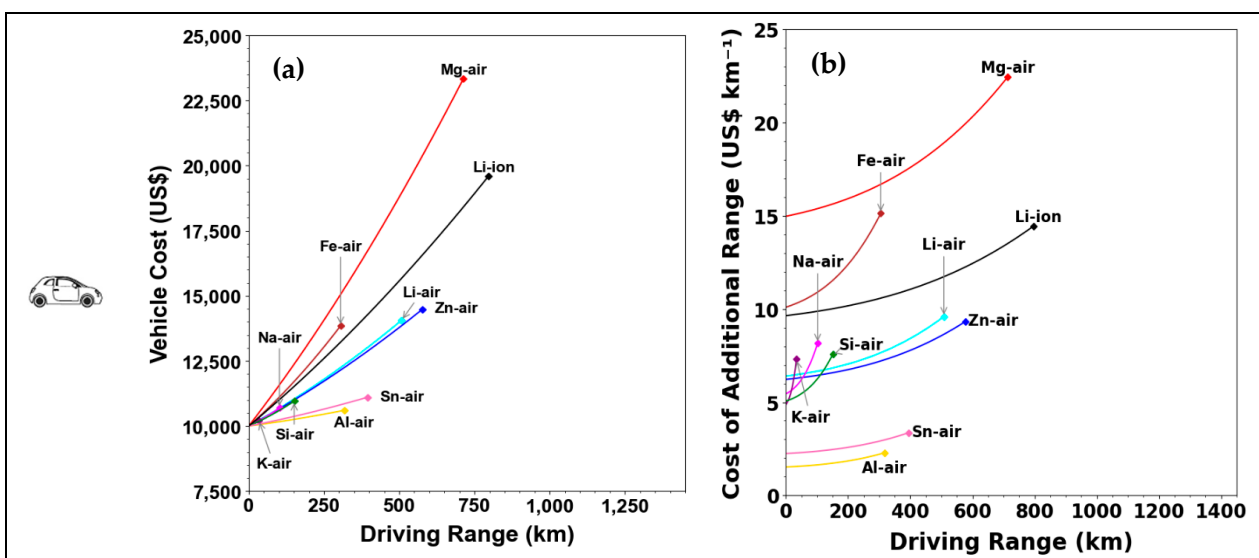


Figure 14. Cont.

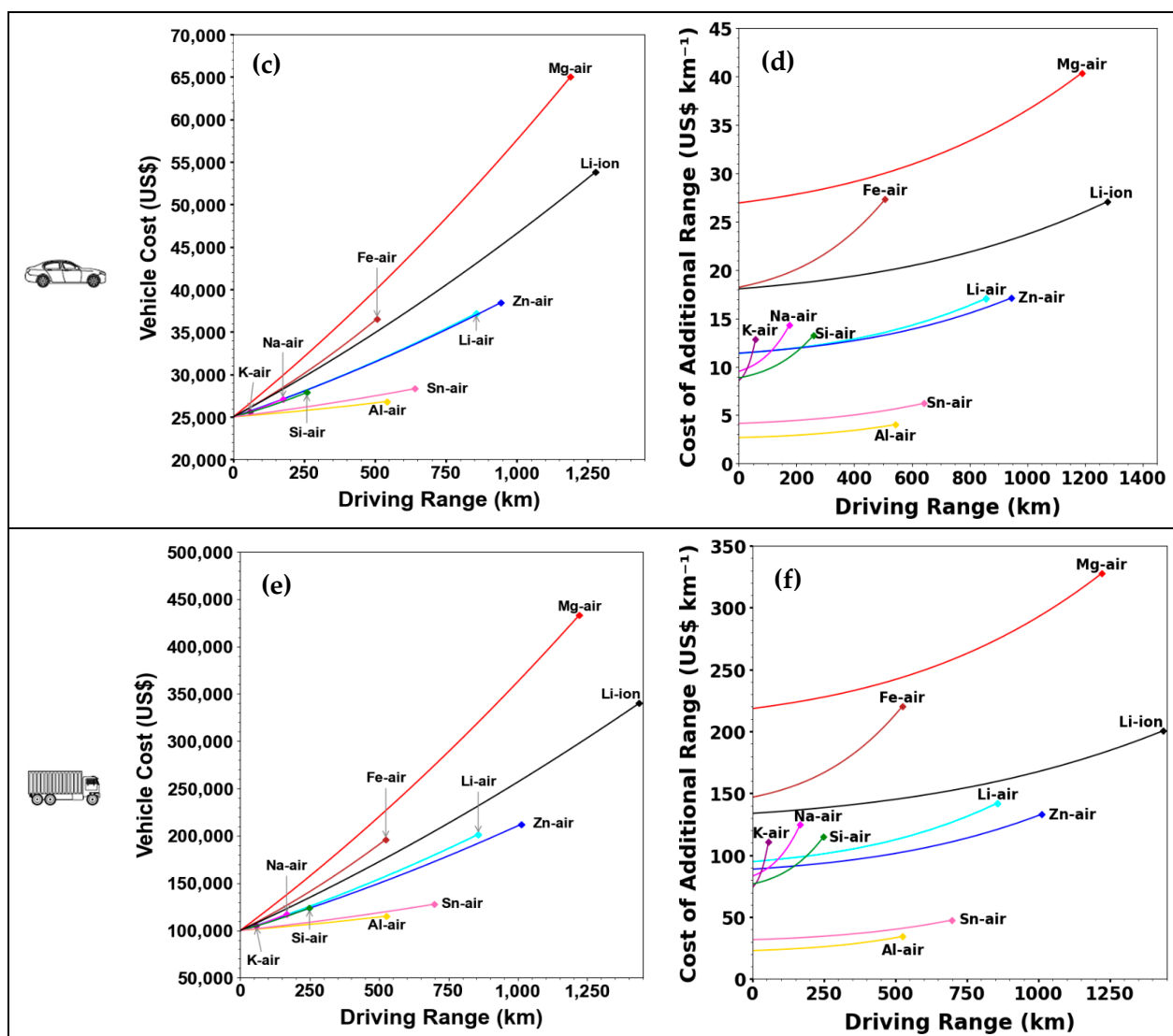


Figure 14. Vehicle cost vs. driving range and cost of additional range vs. driving range. Plots in (a,c,e) are computed from the equations R_V and $C_{V,T}$ (Table 1), while (b,d,f) are plotted from calculating the tangents of the curves of (a,c,e), respectively. (a,b): Mini-vehicle; (c,d): mid-size vehicle; (e,f): semi-trailer truck. Refer to Supplementary Tables S2 and S3 for further calculations and parameters.

4. Conclusions

The electrification of the transportation sector, a major contributor to climate change, necessitates the exploration of alternative battery types beyond Li-ion. MABs have emerged as a promising solution, offering the potential for extended driving ranges at reduced costs. This comparative review examines more than ten different MAB chemistries, evaluating their potential as range extenders in the EV market. The review delves into the design, functionality, and limitations of these MABs, highlighting key theoretical and practical parameters that influence their performance. This paper also shows how certain battery metrics like energy parameters and energy storage cost can be practically evaluated by estimating their effect on vehicle range, battery pack volume, and total vehicle cost. These metrics are related to the battery pack's energy. Cost considerations, particularly the relationship between vehicle cost and driving range, reveal the significant trade-offs involved in adopting these technologies. While no single battery technology can meet the diverse needs of all EV applications, certain MABs, such as Zn-air, Li-air, and Al-air, show considerable promise in addressing the specific demands of different vehicle types. Although some

MABs may not be optimal for current EV applications, this review also underscores their potential significance in other domains where their unique characteristics could be highly advantageous. The viability of MABs as range extenders in EVs depends on their ability to deliver longer driving ranges and their alignment with consumer cost expectations. While Li-ion batteries are well-suited for specific electric mobility applications, broader adoption of various MAB technologies is crucial for a complete transition to clean, low-carbon transportation. This review paper lays the groundwork for researchers to develop effective, reliable, and viable MABs, paving the way for more sustainable and cost-effective solutions in the EV market.

5. Future Outlook

Though this paper reviewed MABs for EVs only, these batteries show immense potential for a wide range of applications due to their high energy density, lightweight properties, and cost-effectiveness. In the realm of light-duty transport, MABs hold promise for EVs such as passenger cars and small trucks. Li-air, Zn-air, and Al-air variants can significantly extend driving ranges compared to traditional Li-ion batteries. Their lightweight nature also makes them ideal for e-bikes and electric scooters, enhancing performance by offering longer ranges and reducing vehicle weight. Beyond transportation, MABs are already making an impact in other fields. In portable electronics, they are commonly used in hearing aids and medical devices due to their compact size and steady power output over extended periods. They are also being explored for grid storage solutions to support renewable energy from sources like solar and wind. Their cost-effectiveness and high energy density make them a viable option for large-scale energy storage, helping to stabilize power grids and ensuring reliable electricity supply. The military and aerospace sectors are investigating MABs for powering critical equipment, benefiting from their high energy density and lightweight design. Similarly, emergency backup systems in hospitals, data centers, and other critical infrastructure rely on these batteries for their long shelf life and dependable power during outages. Current implementations include Zn-air batteries in hearing aids, MABs in remote sensors deployed in harsh environments, and marine applications such as buoys and underwater sensors, where their ability to operate efficiently in wet conditions is invaluable [60]. As research continues to address challenges like improving rechargeability and enhancing performance, metal-air batteries are poised for even broader applications across multiple industries, driving innovation and supporting sustainable energy solutions.

Supplementary Materials: The following supporting information can be downloaded at <https://www.mdpi.com/article/10.3390/batteries11010035/s1>, Table S1: Anode Material Properties and Performance Metrics; Table S2: Electric Vehicle Specifications and Market Analysis; Table S3: Performance and Cost Metrics for Metal-Air Batteries.

Author Contributions: Conceptualization, Y.S. and S.S.M.; methodology, Y.S.; software, Y.S.; validation, Y.S., S.S.M. and S.P.; formal analysis, Y.S.; investigation, Y.S.; resources, Y.S.; data curation, Y.S.; writing—original draft preparation, Y.S.; writing—review and editing, Y.S., S.S.M., S.P., M.M. and M.F.; visualization, Y.S.; supervision, M.F.; project administration, M.F.; funding acquisition, M.F. All authors have read and agreed to the published version of the manuscript.

Funding: This research received no external funding.

Conflicts of Interest: Author Mahboubeh Mousavi was employed by the company AlumaPower Corporation, Kitchener, ON, Canada. The remaining authors declare that the research was conducted in the absence of any commercial or financial relationships that could be construed as a potential conflict of interest.

Abbreviations

Al-air	Aluminum-air batteries
BEVs	Battery electric vehicles
Ca-O ₂	Calcium-oxygen battery
CNT	Carbon nanotubes
CO ₂	Carbon dioxide
EVs	Electric vehicles
Fe-air	Iron-air battery
GDL	Gas diffusion layer
Ge-air	Germanium-air batteries
GPEs	Gel polymer electrolytes
HER	Hydrogen evolution reaction
ICEVs	Internal combustion engine vehicles
IEA	International Energy Agency
LEDs	Light-emitting diodes
Li-air	Lithium-air
Li-ion	Lithium-ion
LISICON	Lithium superionic conductor
MABs	Metal-air batteries
Mg-air	Magnesium-air
Na-air	Sodium-air
OCV	Open circuit voltage
OER	Oxygen-evolution reaction
ORR	Oxygen-reduction reaction
SDICH	Dual-ion-conducting hydrogels
Si-air	Silicon-air batteries
SSE	Solid-state electrolytes
UHP	Ultra-high-purity
Zn-air	Zinc-air

References

1. Østergaard, P.A.; Duic, N.; Noorollahi, Y.; Kalogirou, S. Latest progress in Sustainable Development using renewable energy technology. *Renew. Energy* **2020**, *162*, 1554–1562. [CrossRef]
2. Gaele, M.F.; Di Palma, T.M. Polymer electrolytes for Al-air batteries: Current state and future perspectives. *Energy Fuels* **2022**, *36*, 12875–12895. [CrossRef]
3. Gouveia, J.; Mendes, A.; Monteiro, R.; Mata, T.; Caetano, N.; Martins, A. Life cycle assessment of a vanadium flow battery. *Energy Rep.* **2020**, *6*, 95–101. [CrossRef]
4. Aldhafeeri, T.; Tran, M.-K.; Vrolyk, R.; Pope, M.; Fowler, M. A review of methane gas detection sensors: Recent developments and future perspectives. *Inventions* **2020**, *5*, 28. [CrossRef]
5. Shittu, E.; Suman, R.; Ravikumar, M.K.; Shukla, A.K.; Zhao, G.; Patil, S.; Baker, J. Life cycle assessment of soluble lead redox flow battery. *J. Clean. Prod.* **2022**, *337*, 130503. [CrossRef]
6. Branco, H.; Castro, R.; Lopes, A.S. Battery energy storage systems as a way to integrate renewable energy in small isolated power systems. *Energy Sustain. Dev.* **2018**, *43*, 90–99. [CrossRef]
7. Network, R.E.P. Renewables Global Status Report. Paris: REN21 Secretariat, 272p. Available online: <https://www.ren21.net/gsr-2023/> (accessed on 24 June 2017).
8. Tooryan, F.; HassanzadehFard, H.; Collins, E.R.; Jin, S.; Ramezani, B. Smart integration of renewable energy resources, electrical, and thermal energy storage in microgrid applications. *Energy* **2020**, *212*, 118716. [CrossRef]
9. Madhavan, P.V.; Shahgaldi, S.; Li, X. Ex-situ Characterization of Nb-Ti Alloy/Pt Coated Stainless Steel Bipolar Plates for Proton Exchange Membrane Fuel Cells. *Energy Convers. Manag.* **2024**, *311*, 118536. [CrossRef]
10. Madhavan, P.V.; Zeng, X.; Shahgaldi, S.; Li, X. Investigation of Cr₂SiC Ceramic MAX Phase Coated Metallic Bipolar Plates in Ex-situ Conditions for Proton Exchange Membrane Fuel Cells. *Int. J. Hydrogen Energy* **2024**, *96*, 1232–1242. [CrossRef]
11. Madhavan, P.V.; Shahgaldi, S.; Li, X. Modelling Anti-Corrosion Coating Performance of Metallic Bipolar Plates for PEM Fuel Cells: A Machine Learning Approach. *Energy AI* **2024**, *17*, 100391. [CrossRef]

12. Moradizadeh, L.; Madhavan, P.V.; Chellehbari, Y.M.; Gupta, A.; Li, X.; Shahgaldi, S. Porous transport layers with low Pt loading having Nb–Ta alloy as interlayer for proton exchange membrane water electrolyzers. *Int. J. Hydrogen Energy* **2024**, *94*, 1114–1129. [[CrossRef](#)]
13. Gröger, O.; Gasteiger, H.A.; Suchsland, J.-P. Electromobility: Batteries or fuel cells? *J. Electrochem. Soc.* **2015**, *162*, A2605. [[CrossRef](#)]
14. Legala, A.; Kubesh, M.; Chundru, V.R.; Conway, G.; Li, X. Machine Learning Modelling for Fuel Cell-Battery Hybrid Power System Dynamics in a Toyota Mirai 2 Vehicle Under Various Drive Cycles. *Energy AI* **2024**, *17*, 100415. [[CrossRef](#)]
15. Li, W.; Xie, Y.; Hu, X.; Zhang, B.; Fowler, M.; Panchal, S.; Fraser, R.; Zhang, Y. An efficient two-stage heating strategy for embedded heat pipe system considering power and energy requirements from battery. *Appl. Therm. Eng.* **2024**, *257*, 124499. [[CrossRef](#)]
16. Neubauer, J.; Wood, E. The impact of range anxiety and home, workplace, and public charging infrastructure on simulated battery electric vehicle lifetime utility. *J. Power Sources* **2014**, *257*, 12–20. [[CrossRef](#)]
17. Singer, M. *Consumer Views on Plug-In Electric Vehicles—National Benchmark Report*; National Renewable Energy Laboratory (NREL): Golden, CO, USA, 2016.
18. Li, W.; Long, R.; Chen, H.; Geng, J. A review of factors influencing consumer intentions to adopt battery electric vehicles. *Renew. Sustain. Energy Rev.* **2017**, *78*, 318–328. [[CrossRef](#)]
19. Tran, M.-K.; Bhatti, A.; Vrolyk, R.; Wong, D.; Panchal, S.; Fowler, M.; Fraser, R. A review of range extenders in battery electric vehicles: Current progress and future perspectives. *World Electr. Veh. J.* **2021**, *12*, 54. [[CrossRef](#)]
20. Cano, Z.P.; Banham, D.; Ye, S.; Hintennach, A.; Lu, J.; Fowler, M.; Chen, Z. Batteries and fuel cells for emerging electric vehicle markets. *Nat. Energy* **2018**, *3*, 279–289. [[CrossRef](#)]
21. Zackrisson, M.; Fransson, K.; Hildenbrand, J.; Lampic, G.; O’Dwyer, C. Life cycle assessment of lithium-air battery cells. *J. Clean. Prod.* **2016**, *135*, 299–311. [[CrossRef](#)]
22. Zhang, X.; Li, Z.; Luo, L.; Fan, Y.; Du, Z. A review on thermal management of lithium-ion batteries for electric vehicles. *Energy* **2022**, *238*, 121652. [[CrossRef](#)]
23. Pu, J.H.; Li, Y.; Li, R.C.; Hua, N.; Zhang, H.; Lu, Y.; Panchal, S.; Fraser, R.; Fowler, M.; Zhang, X.-K. Design and performance of a compact lightweight hybrid thermal management system using phase change material and liquid cooling with a honeycomb-like structure for prismatic lithium-ion batteries. *J. Power Sources* **2024**, *624*, 235632. [[CrossRef](#)]
24. Ma, W.; Xie, Y.; Guo, S.; Li, W.; Yang, R.; Panchal, S.; Zhang, Y. A mechanism-data driven resistance transfer algorithm for lithium-ion batteries and its application to thermal modeling. *J. Energy Storage* **2024**, *102*, 114066. [[CrossRef](#)]
25. O’hayre, R.; Cha, S.-W.; Colella, W.; Prinz, F.B. *Fuel Cell Fundamentals*; John Wiley & Sons: Hoboken, NJ, USA, 2016.
26. Alaswad, A.; Baroutaji, A.; Achour, H.; Carton, J.; Al Makky, A.; Olabi, A.-G. Developments in fuel cell technologies in the transport sector. *Int. J. Hydrogen Energy* **2016**, *41*, 16499–16508. [[CrossRef](#)]
27. Ramasubramanian, B.; Rao, R.P.; Chellappan, V.; Ramakrishna, S. Towards sustainable fuel cells and batteries with an AI perspective. *Sustainability* **2022**, *14*, 16001. [[CrossRef](#)]
28. Bank, D. *Welcome to the Lithium-Ion Age*; Deutsche Bank AG: Sydney, Australia, 2016.
29. Van Noorden, R. A better battery. *Nature* **2014**, *507*, 26. [[CrossRef](#)] [[PubMed](#)]
30. Placke, T.; Kloepsch, R.; Dühnen, S.; Winter, M. Lithium ion, lithium metal, and alternative rechargeable battery technologies: The odyssey for high energy density. *J. Solid State Electrochem.* **2017**, *21*, 1939–1964. [[CrossRef](#)]
31. Nayak, P.K.; Yang, L.; Brehm, W.; Adelhelm, P. From lithium-ion to sodium-ion batteries: Advantages, challenges, and surprises. *Angew. Chem. Int. Ed.* **2018**, *57*, 102–120. [[CrossRef](#)] [[PubMed](#)]
32. Li, M.; Lu, J.; Chen, Z.; Amine, K. 30 years of lithium-ion batteries. *Adv. Mater.* **2018**, *30*, 1800561. [[CrossRef](#)]
33. Popp, D. Fit for 55: MEPs Back Objective of Zero Emissions for Cars and Vans in 2035. 2022. Available online: <https://www.europarl.europa.eu/news> (accessed on 5 October 2024).
34. Yu, X.; Chen, R.; Gan, L.; Li, H.; Chen, L. Battery safety: From lithium-ion to solid-state batteries. *Engineering* **2023**, *21*, 9–14. [[CrossRef](#)]
35. Feng, X.; Ren, D.; He, X.; Ouyang, M. Mitigating thermal runaway of lithium-ion batteries. *Joule* **2020**, *4*, 743–770. [[CrossRef](#)]
36. Deng, D. Li-ion batteries: Basics, progress, and challenges. *Energy Sci. Eng.* **2015**, *3*, 385–418. [[CrossRef](#)]
37. Mokhtar, M.; Talib, M.Z.M.; Majlan, E.H.; Tasirin, S.M.; Ramli, W.M.F.W.; Daud, W.R.W.; Sahari, J. Recent developments in materials for aluminum–air batteries: A review. *J. Ind. Eng. Chem.* **2015**, *32*, 1–20. [[CrossRef](#)]
38. Wen, H.; Liu, Z.; Qiao, J.; Chen, R.; Zhao, R.; Wu, J.; Qiao, G.; Yang, J. High energy efficiency and high power density aluminum-air flow battery. *Int. J. Energy Res.* **2020**, *44*, 7568–7579. [[CrossRef](#)]
39. Hou, J.; Yang, M.; Wang, D.; Zhang, J. Fundamentals and challenges of lithium ion batteries at temperatures between –40 and 60° C. *Adv. Energy Mater.* **2020**, *10*, 1904152. [[CrossRef](#)]
40. Bandhauer, T.M.; Garimella, S.; Fuller, T.F. A critical review of thermal issues in lithium-ion batteries. *J. Electrochem. Soc.* **2011**, *158*, R1. [[CrossRef](#)]
41. Costa, C.M.; Barbosa, J.C.; Gonçalves, R.; Castro, H.; Del Campo, F.; Lanceros-Méndez, S. Recycling and environmental issues of lithium-ion batteries: Advances, challenges and opportunities. *Energy Storage Materials* **2021**, *37*, 433–465. [[CrossRef](#)]

42. Ma, J.; Li, Y.; Grundish, N.S.; Goodenough, J.B.; Chen, Y.; Guo, L.; Peng, Z.; Qi, X.; Yang, F.; Qie, L. The 2021 battery technology roadmap. *J. Phys. D Appl. Phys.* **2021**, *54*, 183001. [CrossRef]
43. Chen, J.; Kollmeyer, P.; Panchal, S.; Masoudi, Y.; Gross, O.; Emadi, A. Experimental results of battery power capability measurement on cells with different state of health levels. In Proceedings of the 2024 IEEE Transportation Electrification Conference and Expo (ITEC), Chicago, IL, USA, 19–21 June 2024; pp. 1–6.
44. Liu, Q.; Pan, Z.; Wang, E.; An, L.; Sun, G. Aqueous metal-air batteries: Fundamentals and applications. *Energy Storage Mater.* **2020**, *27*, 478–505. [CrossRef]
45. Li, Y.; Lu, J. Metal-air batteries: Will they be the future electrochemical energy storage device of choice? *ACS Energy Lett.* **2017**, *2*, 1370–1377. [CrossRef]
46. Li, T.; Huang, M.; Bai, X.; Wang, Y.-X. Metal-air batteries: A review on current status and future applications. *Prog. Nat. Sci. Mater. Int.* **2023**, *33*, 151–171. [CrossRef]
47. Rani, B.; Yadav, J.K.; Saini, P.; Pandey, A.P.; Dixit, A. Aluminum-air batteries: Current advances and promises with future directions. *RSC Adv.* **2024**, *14*, 17628–17663. [CrossRef] [PubMed]
48. Hardwick, L.J.; De León, C.P. Rechargeable multi-valent metal-air batteries. *Johns. Matthey Technol. Rev.* **2018**, *62*, 134–149. [CrossRef]
49. Alemu, M.A.; Getie, M.Z.; Worku, A.K. Advancement of electrically rechargeable multivalent metal-air batteries for future mobility. *Ionics* **2023**, *29*, 3421–3435. [CrossRef]
50. Fu, J.; Cano, Z.P.; Park, M.G.; Yu, A.; Fowler, M.; Chen, Z. Electrically rechargeable zinc-air batteries: Progress, challenges, and perspectives. *Adv. Mater.* **2017**, *29*, 1604685. [CrossRef]
51. Buckingham, R.; Asset, T.; Atanassov, P. Aluminum-air batteries: A review of alloys, electrolytes and design. *J. Power Sources* **2021**, *498*, 229762. [CrossRef]
52. Feng, Y.; Xiong, W.; Zhang, J.; Wang, R.; Wang, N. Electrochemical discharge performance of the Mg–Al–Pb–Ce–Y alloy as the anode for Mg–air batteries. *J. Mater. Chem. A* **2016**, *4*, 8658–8668. [CrossRef]
53. Zhang, T.; Tao, Z.; Chen, J. Magnesium-air batteries: From principle to application. *Mater. Horiz.* **2014**, *1*, 196–206. [CrossRef]
54. Arafat, Y.; Azhar, M.R.; Zhong, Y.; Tadé, M.O.; Shao, Z. Metal-free carbon based air electrodes for Zn-air batteries: Recent advances and perspective. *Mater. Res. Bull.* **2021**, *140*, 111315. [CrossRef]
55. Bi, X.; Jiang, Y.; Chen, R.; Du, Y.; Zheng, Y.; Yang, R.; Wang, R.; Wang, J.; Wang, X.; Chen, Z. Rechargeable zinc-air versus lithium-air battery: From fundamental promises toward technological potentials. *Adv. Energy Mater.* **2024**, *14*, 2302388. [CrossRef]
56. Li, L.; Chang, Z.w.; Zhang, X.B. Recent progress on the development of metal-air batteries. *Adv. Sustain. Syst.* **2017**, *1*, 1700036. [CrossRef]
57. Li, T.; Peng, X.; Cui, P.; Shi, G.; Yang, W.; Chen, Z.; Huang, Y.; Chen, Y.; Peng, J.; Zou, R. Recent progress and future perspectives of flexible metal-air batteries. *SmartMat* **2021**, *2*, 519–553. [CrossRef]
58. U.S. Geological Survey. *Mineral Commodity Summaries 2024*; U.S. Geological Survey: Reston, VA, USA, 2024. Available online: <https://www.usgs.gov/publications/mineral-commodity-summaries-2024> (accessed on 5 October 2024).
59. Leimer, D.H.W. Abundances of Chemical Elements in the Earth's Crust. Available online: <https://sites.tntech.edu/hwleimer/geol-1040/geol-1040-lecture/abundances-of-chemical-elements-in-the-earths-crust/> (accessed on 6 June 2024).
60. Wang, C.; Yu, Y.; Niu, J.; Liu, Y.; Bridges, D.; Liu, X.; Pooran, J.; Zhang, Y.; Hu, A. Recent progress of metal-air batteries—A mini review. *Appl. Sci.* **2019**, *9*, 2787. [CrossRef]
61. Han, X.; Li, X.; White, J.; Zhong, C.; Deng, Y.; Hu, W.; Ma, T. Metal-air batteries: From static to flow system. *Adv. Energy Mater.* **2018**, *8*, 1801396. [CrossRef]
62. Cheng, F.; Chen, J. Metal-air batteries: From oxygen reduction electrochemistry to cathode catalysts. *Chem. Soc. Rev.* **2012**, *41*, 2172–2192. [CrossRef]
63. Cheng, J.; Zhang, L.; Yang, Y.-S.; Wen, Y.-H.; Cao, G.-P.; Wang, X.-D. Preliminary study of single flow zinc-nickel battery. *Electrochem. Commun.* **2007**, *9*, 2639–2642. [CrossRef]
64. Fu, J.; Zhang, J.; Song, X.; Zarrin, H.; Tian, X.; Qiao, J.; Rasen, L.; Li, K.; Chen, Z. A flexible solid-state electrolyte for wide-scale integration of rechargeable zinc-air batteries. *Energy Environ. Sci.* **2016**, *9*, 663–670. [CrossRef]
65. Zhou, G.; Li, F.; Cheng, H.-M. Progress in flexible lithium batteries and future prospects. *Energy Environ. Sci.* **2014**, *7*, 1307–1338. [CrossRef]
66. Sumboja, A.; Ge, X.; Zong, Y.; Liu, Z. Progress in development of flexible metal-air batteries. *Funct. Mater. Lett.* **2016**, *9*, 1630001. [CrossRef]
67. Wang, Y.; Kwok, H.; Pan, W.; Zhang, H.; Leung, D.Y. Innovative paper-based Al-air batteries as a low-cost and green energy technology for the miniwatt market. *J. Power Sources* **2019**, *414*, 278–282. [CrossRef]
68. Li, F.; Zhang, T.; Zhou, H. Challenges of non-aqueous Li–O₂ batteries: Electrolytes, catalysts, and anodes. *Energy Environ. Sci.* **2013**, *6*, 1125–1141. [CrossRef]

69. Yadegari, H.; Sun, Q.; Sun, X. Sodium-oxygen batteries: A comparative review from chemical and electrochemical fundamentals to future perspective. *Adv. Mater.* **2016**, *28*, 7065–7093. [[CrossRef](#)]
70. Ren, X.; Wu, Y. A low-overpotential potassium–oxygen battery based on potassium superoxide. *J. Am. Chem. Soc.* **2013**, *135*, 2923–2926. [[CrossRef](#)] [[PubMed](#)]
71. Zhang, X.-B. *Metal-Air Batteries: Fundamentals and Applications*; John Wiley & Sons: Hoboken, NJ, USA, 2018.
72. Liu, Q.; Chang, Z.; Li, Z.; Zhang, X. Flexible metal–air batteries: Progress, challenges, and perspectives. *Small Methods* **2018**, *2*, 1700231. [[CrossRef](#)]
73. McCloskey, B.D.; Scheffler, R.; Speidel, A.; Bethune, D.S.; Shelby, R.M.; Luntz, A.C. On the efficacy of electrocatalysis in nonaqueous Li–O₂ batteries. *J. Am. Chem. Soc.* **2011**, *133*, 18038–18041. [[CrossRef](#)]
74. Peng, Z.; Freunberger, S.A.; Chen, Y.; Bruce, P.G. A reversible and higher-rate Li–O₂ battery. *Science* **2012**, *337*, 563–566. [[CrossRef](#)]
75. Chen, Y.; Freunberger, S.A.; Peng, Z.; Fontaine, O.; Bruce, P.G. Charging a Li–O₂ battery using a redox mediator. *Nat. Chem.* **2013**, *5*, 489–494. [[CrossRef](#)] [[PubMed](#)]
76. Xu, J.-J.; Wang, Z.-L.; Xu, D.; Zhang, L.-L.; Zhang, X.-B. Tailoring deposition and morphology of discharge products towards high-rate and long-life lithium–oxygen batteries. *Nat. Commun.* **2013**, *4*, 2438. [[CrossRef](#)]
77. Zhang, T.; Zhou, H. A reversible long-life lithium–air battery in ambient air. *Nat. Commun.* **2013**, *4*, 1817. [[CrossRef](#)]
78. Tu, K.-N.; Gusak, A. Mean-time-to-failure equations for electromigration, thermomigration, and stress migration. *IEEE Trans. Compon. Packag. Manuf. Technol.* **2020**, *10*, 1427–1431. [[CrossRef](#)]
79. Bard, A.J.; Faulkner, L.R.; White, H.S. *Electrochemical Methods: Fundamentals and Applications*; John Wiley & Sons: Hoboken, NJ, USA, 2022.
80. Ye, L.; Liao, M.; Zhao, T.; Sun, H.; Zhao, Y.; Sun, X.; Wang, B.; Peng, H. A sodiophilic interphase-mediated, dendrite-free anode with ultrahigh specific capacity for sodium–metal batteries. *Angew. Chem.* **2019**, *131*, 17210–17216. [[CrossRef](#)]
81. Olabi, A.G.; Sayed, E.T.; Wilberforce, T.; Jamal, A.; Alami, A.H.; Elsaïd, K.; Rahman, S.M.A.; Shah, S.K.; Abdelkareem, M.A. Metal-air batteries—A review. *Energies* **2021**, *14*, 7373. [[CrossRef](#)]
82. Arai, H. Introduction—General features of metal-air batteries. In *Electrochemical Power Sources: Fundamentals, Systems, and Applications*; Elsevier: Amsterdam, The Netherlands, 2021; pp. 1–10.
83. Arai, H.; Ikezawa, A. *Electrochemical Devices | Electrochemical Power Sources: Fundamentals, Systems, and Applications*; Elsevier: Amsterdam, The Netherlands, 2021.
84. Arai, H. Metal Storage/Metal Air (Zn, Fe, Al, Mg). In *Electrochemical Energy Storage for Renewable Sources and Grid Balancing*; Elsevier: Amsterdam, The Netherlands, 2015; pp. 337–344.
85. Arai, H.; Hayashi, M. Secondary batteries—metal-air Systems | Overview (secondary and primary). *Encycl. Electrochem. Power Sources* **2009**, 347–355. [[CrossRef](#)]
86. Xu, S.; Lau, S.; Archer, L.A. CO₂ and ambient air in metal–oxygen batteries: Steps towards reality. *Inorg. Chem. Front.* **2015**, *2*, 1070–1079. [[CrossRef](#)]
87. Salado, M.; Lizundia, E. Advances, challenges, and environmental impacts in metal–air battery electrolytes. *Mater. Today Energy* **2022**, *28*, 101064. [[CrossRef](#)]
88. Park, M.; Kim, K.Y.; Seo, H.; Cheon, Y.E.; Koh, J.H.; Sun, H.; Kim, T.J. Practical challenges associated with catalyst development for the commercialization of Li-air batteries. *J. Electrochem. Sci. Technol.* **2014**, *5*, 1–18. [[CrossRef](#)]
89. Suryatna, A.; Raya, I.; Thangavelu, L.; Alhachami, F.R.; Kadhim, M.M.; Altimari, U.S.; Mahmoud, Z.H.; Mustafa, Y.F.; Kianfar, E. A Review of High-Energy Density Lithium-Air Battery Technology: Investigating the Effect of Oxides and Nanocatalysts. *J. Chem.* **2022**, *2022*, 2762647. [[CrossRef](#)]
90. Li, J.; Hou, L.; Yu, M.; Li, Q.; Zhang, T.; Sun, H. Review and Recent Advances of Oxygen Transfer in Li-air Batteries. *ChemElectroChem* **2021**, *8*, 3588–3603. [[CrossRef](#)]
91. Jilani, A.; Awan, Z.; Taqvi, S.A.A.; Khan, F.; Alshahrani, T. Recent Advances in the Development of Li-Air Batteries, Experimental and Predictive Approaches—Prospective, Challenges, and Opportunities. *ChemBioEng Rev.* **2024**, *11*, 95–114. [[CrossRef](#)]
92. Manthiram, A.; Li, L. Hybrid and Aqueous Lithium-Air Batteries. *Adv. Energy Mater.* **2015**, *5*, 1401302. [[CrossRef](#)]
93. Zhang, Z.; Xiao, X.; Zhu, X.; Tan, P. Addressing transport issues in non-aqueous Li–air batteries to achieving high electrochemical performance. *Electrochem. Energy Rev.* **2023**, *6*, 18. [[CrossRef](#)]
94. Luntz, A.C.; McCloskey, B.D. Nonaqueous Li–air batteries: A status report. *Chem. Rev.* **2014**, *114*, 11721–11750. [[CrossRef](#)] [[PubMed](#)]
95. Feng, N.; He, P.; Zhou, H. Critical challenges in rechargeable aprotic Li–O₂ batteries. *Adv. Energy Mater.* **2016**, *6*, 1502303. [[CrossRef](#)]
96. Shu, C.; Wang, J.; Long, J.; Liu, H.K.; Dou, S.X. Understanding the reaction chemistry during charging in aprotic lithium–oxygen batteries: Existing problems and solutions. *Adv. Mater.* **2019**, *31*, 1804587. [[CrossRef](#)] [[PubMed](#)]
97. Zhang, T.; Imanishi, N.; Takeda, Y.; Yamamoto, O. Aqueous lithium/air rechargeable batteries. *Chem. Lett.* **2011**, *40*, 668–673. [[CrossRef](#)]

98. Imanishi, N.; Yamamoto, O. Rechargeable lithium–air batteries: Characteristics and prospects. *Mater. Today* **2014**, *17*, 24–30. [[CrossRef](#)]
99. Imanishi, N.; Yamamoto, O. Perspectives and challenges of rechargeable lithium–air batteries. *Mater. Today Adv.* **2019**, *4*, 100031. [[CrossRef](#)]
100. Chen, P.; Bai, F.; Deng, J.W.; Liu, B.; Zhang, T. Recent progresses and challenges in aqueous lithium–air batteries relating to the solid electrolyte separator: A mini-review. *Front. Chem.* **2022**, *10*, 1035691. [[CrossRef](#)] [[PubMed](#)]
101. Imanishi, N.; Hasegawa, S.; Zhang, T.; Hirano, A.; Takeda, Y.; Yamamoto, O. Lithium anode for lithium-air secondary batteries. *J. Power Sources* **2008**, *185*, 1392–1397. [[CrossRef](#)]
102. Wang, Y.; Zhou, H. A lithium-air battery with a potential to continuously reduce O₂ from air for delivering energy. *J. Power Sources* **2010**, *195*, 358–361. [[CrossRef](#)]
103. Zhang, T.; Imanishi, N.; Hasegawa, S.; Hirano, A.; Xie, J.; Takeda, Y.; Yamamoto, O.; Sammes, N. Li/Polymer Electrolyte/Water Stable Lithium-Conducting Glass Ceramics Composite for Lithium–Air Secondary Batteries with an Aqueous Electrolyte. *J. Electrochem. Soc.* **2008**, *155*, A965. [[CrossRef](#)]
104. He, P.; Wang, Y.; Zhou, H. A Li-air fuel cell with recycle aqueous electrolyte for improved stability. *Electrochem. Commun.* **2010**, *12*, 1686–1689. [[CrossRef](#)]
105. Hasegawa, S.; Imanishi, N.; Zhang, T.; Xie, J.; Hirano, A.; Takeda, Y.; Yamamoto, O. Study on lithium/air secondary batteries—Stability of NASICON-type lithium ion conducting glass–ceramics with water. *J. Power Sources* **2009**, *189*, 371–377. [[CrossRef](#)]
106. Li, L.; Zhao, X.; Manthiram, A. A dual-electrolyte rechargeable Li-air battery with phosphate buffer catholyte. *Electrochem. Commun.* **2012**, *14*, 78–81. [[CrossRef](#)]
107. Shimonishi, Y.; Zhang, T.; Johnson, P.; Imanishi, N.; Hirano, A.; Takeda, Y.; Yamamoto, O.; Sammes, N. A study on lithium/air secondary batteries—Stability of NASICON-type glass ceramics in acid solutions. *J. Power Sources* **2010**, *195*, 6187–6191. [[CrossRef](#)]
108. Ding, F.; Xu, W.; Shao, Y.; Chen, X.; Wang, Z.; Gao, F.; Liu, X.; Zhang, J.-G. H⁺ diffusion and electrochemical stability of Li_{1+x}Al_xTi_{2–x}Si_yP_{3–y}O₁₂ glass in aqueous Li/air battery electrolytes. *J. Power Sources* **2012**, *214*, 292–297. [[CrossRef](#)]
109. Bidault, F.; Brett, D.; Middleton, P.; Brandon, N. Review of gas diffusion cathodes for alkaline fuel cells. *J. Power Sources* **2009**, *187*, 39–48. [[CrossRef](#)]
110. He, P.; Zhang, T.; Jiang, J.; Zhou, H. Lithium–air batteries with hybrid electrolytes. *J. Phys. Chem. Lett.* **2016**, *7*, 1267–1280. [[CrossRef](#)]
111. Manthiram, A.; Yu, X.; Wang, S. Lithium battery chemistries enabled by solid-state electrolytes. *Nat. Rev. Mater.* **2017**, *2*, 1–16. [[CrossRef](#)]
112. Choudhury, S.; Stalin, S.; Deng, Y.; Archer, L.A. Soft colloidal glasses as solid-state electrolytes. *Chem. Mater.* **2018**, *30*, 5996–6004. [[CrossRef](#)]
113. Wu, Y.; Li, Y.; Wang, Y.; Liu, Q.; Chen, Q.; Chen, M. Advances and prospects of PVDF based polymer electrolytes. *J. Energy Chem.* **2022**, *64*, 62–84. [[CrossRef](#)]
114. Wang, H.-F.; Wang, X.-X.; Li, F.; Xu, J.-J. Fundamental Understanding and Construction of Solid-State Li–Air Batteries. *Small Sci.* **2022**, *2*, 2200005. [[CrossRef](#)]
115. Vadhva, P.; Gill, T.E.; Cruddos, J.H.; Said, S.; Siniscalchi, M.; Narayanan, S.; Pasta, M.; Miller, T.S.; Rettie, A.J. Engineering solution-processed non-crystalline solid electrolytes for Li metal batteries. *Chem. Mater.* **2023**, *35*, 1168–1176. [[CrossRef](#)]
116. Raj, H.; Fabre, T.; Lachal, M.; Neveu, A.; Jean, J.; Steil, M.C.; Bouchet, R.; Pralong, V. Stabilizing the NASICON Solid Electrolyte in an Inert Atmosphere as a Function of Physical Properties and Sintering Conditions for Solid-State Battery Fabrication. *ACS Appl. Energy Mater.* **2023**, *6*, 1197–1207. [[CrossRef](#)]
117. Xu, A.; Wang, R.; Yao, M.; Cao, J.; Li, M.; Yang, C.; Liu, F.; Ma, J. Electrochemical properties of an Sn-doped LATP ceramic electrolyte and its derived sandwich-structured composite solid electrolyte. *Nanomaterials* **2022**, *12*, 2082. [[CrossRef](#)]
118. Zhang, H.; Yu, Z.; Cheng, J.; Chen, H.; Huang, X.; Tian, B. Halide/sulfide composite solid-state electrolyte for Li-anode based all-solid-state batteries. *Chin. Chem. Lett.* **2023**, *34*, 108228. [[CrossRef](#)]
119. Hamao, N.; Hamamoto, K. Fabrication of single-grain-layered garnet-type electrolyte sheets by a precursor method. *J. Asian Ceram. Soc.* **2022**, *10*, 1–8. [[CrossRef](#)]
120. Sun, J.; Zhao, N.; Li, Y.; Guo, X.; Feng, X.; Liu, X.; Liu, Z.; Cui, G.; Zheng, H.; Gu, L. A rechargeable Li-air fuel cell battery based on garnet solid electrolytes. *Sci. Rep.* **2017**, *7*, 41217. [[CrossRef](#)] [[PubMed](#)]
121. Lu, J.; Li, Y. Perovskite-type Li-ion solid electrolytes: A review. *J. Mater. Sci. Mater. Electron.* **2021**, *32*, 9736–9754. [[CrossRef](#)]
122. Hashishin, T.; Shimomura, H.; Kamiyama, R.; Matsuda, M. Analcime with high sodium ion conduction as a solid electrolyte. *J. Phys. Chem. C* **2022**, *126*, 19480–19486. [[CrossRef](#)]
123. Cao, W.; Yang, Y.; Deng, J.; Li, Y.; Cui, C.; Zhang, T. Localization of electrons within interlayer stabilizes NASICON-type solid-state electrolyte. *Mater. Today Energy* **2021**, *22*, 100875. [[CrossRef](#)]
124. Xu, Z.; Liu, Z.; Gu, Z.; Zhao, X.; Guo, D.; Yao, X. Polyimide-based solid-state gel polymer electrolyte for lithium–oxygen batteries with a long-cycling life. *ACS Appl. Mater. Interfaces* **2023**, *15*, 7014–7022. [[CrossRef](#)] [[PubMed](#)]

125. Hamao, N.; Yamaguchi, Y.; Hamamoto, K. Densification of a NASICON-type LATP electrolyte sheet by a cold-sintering process. *Materials* **2021**, *14*, 4737. [[CrossRef](#)] [[PubMed](#)]
126. Zhu, Q.; Ma, J.; Li, S.; Mao, D. Solid-state electrolyte for lithium-air batteries: A review. *Polymers* **2023**, *15*, 2469. [[CrossRef](#)] [[PubMed](#)]
127. Sun, Z.; Lu, H.; Fan, L.; Hong, Q.; Leng, J.; Chen, C. Performance of Al-air batteries based on Al–Ga, Al–In and Al–Sn alloy electrodes. *J. Electrochem. Soc.* **2015**, *162*, A2116. [[CrossRef](#)]
128. Zhang, Z.; Xiong, L.; Wang, S.; Xie, Y.; You, W.; Du, X. A review of the Al-gas batteries and perspectives for a “Real” Al-air battery. *J. Power Sources* **2023**, *580*, 233375. [[CrossRef](#)]
129. Elia, G.A.; Marquardt, K.; Hoepfner, K.; Fantini, S.; Lin, R.; Knipping, E.; Peters, W.; Drillet, J.F.; Passerini, S.; Hahn, R. An overview and future perspectives of aluminum batteries. *Adv. Mater.* **2016**, *28*, 7564–7579. [[CrossRef](#)] [[PubMed](#)]
130. Chen, L.; Li, B.; Zhu, L.; Deng, X.; Sun, X.; Liu, Y.; Zhang, C.; Zhao, W.; Chen, X. A PVA/LiCl/PEO interpenetrating composite electrolyte with a three-dimensional dual-network for all-solid-state flexible aluminum–air batteries. *RSC Adv.* **2021**, *11*, 39476–39483. [[CrossRef](#)] [[PubMed](#)]
131. Haynes, W.M. *CRC Handbook of Chemistry and Physics*, 95th ed.; Taylor & Francis Group, LLC: Abingdon, UK, 2014.
132. Hu, Y.; Sun, D.; Luo, B.; Wang, L. Recent progress and future trends of aluminum batteries. *Energy Technol.* **2019**, *7*, 86–106. [[CrossRef](#)]
133. Bogolowski, N.; Drillet, J.-F. An electrically rechargeable Al-air battery with aprotic ionic liquid electrolyte. *ECS Trans.* **2017**, *75*, 85. [[CrossRef](#)]
134. Carlin, R.T.; Osteryoung, R.A. Aluminum anodization in a basic ambient temperature molten salt. *J. Electrochem. Soc.* **1989**, *136*, 1409. [[CrossRef](#)]
135. Ocon, J.D.; Kim, J.W.; Abrenica, G.H.A.; Lee, J.K.; Lee, J. Quasi-perpetual discharge behaviour in p-type Ge–air batteries. *Phys. Chem. Chem. Phys.* **2014**, *16*, 22487–22494. [[CrossRef](#)]
136. Revel, R.; Audichon, T.; Gonzalez, S. Non-aqueous aluminium–air battery based on ionic liquid electrolyte. *J. Power Sources* **2014**, *272*, 415–421. [[CrossRef](#)]
137. Wang, D.; Gao, X.; Chen, Y.; Jin, L.; Kuss, C.; Bruce, P.G. Plating and stripping calcium in an organic electrolyte. *Nat. Mater.* **2018**, *17*, 16–20. [[CrossRef](#)] [[PubMed](#)]
138. Schröder, D.; Janek, J.; Adelhelm, P. Nonlithium Aprotic Metal/Oxygen Batteries Using Na, K, Mg, or Ca as Metal Anode. *Encycl. Electrochem. Online* **2007**, 1–29. [[CrossRef](#)]
139. Xiao, N.; Ren, X.; McCulloch, W.D.; Gourdin, G.; Wu, Y. Potassium superoxide: A unique alternative for metal–air batteries. *Acc. Chem. Res.* **2018**, *51*, 2335–2343. [[CrossRef](#)] [[PubMed](#)]
140. Deyab, M.; Mohsen, Q. Improved battery capacity and cycle life in iron-air batteries with ionic liquid. *Renew. Sustain. Energy Rev.* **2021**, *139*, 110729. [[CrossRef](#)]
141. McKerracher, R.; Ponce de Leon, C.; Wills, R.; Shah, A.A.; Walsh, F.C. A review of the iron–air secondary battery for energy storage. *ChemPlusChem* **2015**, *80*, 323–335. [[CrossRef](#)]
142. Zhao, X.; Xu, N.; Li, X.; Gong, Y.; Huang, K. Energy storage characteristics of a new rechargeable solid oxide iron–air battery. *RSC Adv.* **2012**, *2*, 10163–10166. [[CrossRef](#)]
143. Arai, H.; Garche, J.; Colmenares, L.C. *Electrochemical Power Sources: Fundamentals, Systems, and Applications: Metal–Air Batteries: Present and Perspectives*; Elsevier: Amsterdam, The Netherlands, 2020.
144. Sun, Q.; Dai, L.; Luo, T.; Wang, L.; Liang, F.; Liu, S. Recent advances in solid-state metal–air batteries. *Carbon Energy* **2023**, *5*, e276. [[CrossRef](#)]
145. Zhao, X.; Gong, Y.; Li, X.; Xu, N.; Huang, K. Performance of solid oxide iron-air battery operated at 550 C. *J. Electrochem. Soc.* **2013**, *160*, A1241. [[CrossRef](#)]
146. Jin, X.; Uddin, A.M.; Zhao, X.; White, R.; Huang, K. Understanding the High-Temperature Solid-Oxide Iron-Air Redox Battery Operated with an Oxygen Shuttle Mechanism: A Computational Study. *J. Electrochem. Soc.* **2015**, *162*, A1476. [[CrossRef](#)]
147. Girishkumar, G.; McCloskey, B.; Luntz, A.C.; Swanson, S.; Wilcke, W. Lithium-air battery: Promise and challenges. *J. Phys. Chem. Lett.* **2010**, *1*, 2193–2203. [[CrossRef](#)]
148. Lu, J.; Li, L.; Park, J.-B.; Sun, Y.-K.; Wu, F.; Amine, K. Aprotic and aqueous Li–O₂ batteries. *Chem. Rev.* **2014**, *114*, 5611–5640. [[CrossRef](#)]
149. Kowalczyk, I.; Read, J.; Salomon, M. Li-air batteries: A classic example of limitations owing to solubilities. *Pure Appl. Chem.* **2007**, *79*, 851–860. [[CrossRef](#)]
150. Geng, D.; Ding, N.; Hor, T.A.; Chien, S.W.; Liu, Z.; Wu, D.; Sun, X.; Zong, Y. From lithium-oxygen to lithium-air batteries: Challenges and opportunities. *Adv. Energy Mater.* **2016**, *6*, 1502164. [[CrossRef](#)]
151. Grande, L.; Paillard, E.; Hassoun, J.; Park, J.B.; Lee, Y.J.; Sun, Y.K.; Passerini, S.; Scrosati, B. The lithium/air battery: Still an emerging system or a practical reality? *Adv. Mater.* **2015**, *27*, 784–800. [[CrossRef](#)] [[PubMed](#)]
152. Staniewicz, R.J. A study of the calcium-thionyl chloride electrochemical system. *J. Electrochem. Soc.* **1980**, *127*, 782. [[CrossRef](#)]

153. Weinrich, H.; Durmus, Y.E.; Tempel, H.; Kungl, H.; Eichel, R.-A. Silicon and iron as resource-efficient anode materials for ambient-temperature metal-air batteries: A review. *Materials* **2019**, *12*, 2134. [[CrossRef](#)]
154. Xu, X.; San Hui, K.; Dinh, D.A.; Hui, K.N.; Wang, H. Recent advances in hybrid sodium–air batteries. *Mater. Horiz.* **2019**, *6*, 1306–1335. [[CrossRef](#)]
155. Faktorovich-Simon, E.; Natan, A.; Peled, E.; Golodnitsky, D. Oxygen redox processes in PEGDME-based electrolytes for the Na-air battery. *J. Solid State Electrochem.* **2018**, *22*, 1015–1022. [[CrossRef](#)]
156. Ju, H.; Lee, J. High-temperature liquid Sn-air energy storage cell. *J. Energy Chem.* **2015**, *24*, 614–619. [[CrossRef](#)]
157. Andrés, C.M.C.; Pérez de la Lastra, J.M.; Andrés Juan, C.; Plou, F.J.; Pérez-Lebeña, E. Superoxide Anion Chemistry—Its Role at the Core of the Innate Immunity. *Int. J. Mol. Sci.* **2023**, *24*, 1841. [[CrossRef](#)] [[PubMed](#)]
158. Skyllas-Kazacos, M.; Cao, L.; Kazacos, M.; Kausar, N.; Mousa, A. Vanadium electrolyte studies for the vanadium redox battery—A review. *ChemSusChem* **2016**, *9*, 1521–1543. [[CrossRef](#)]
159. Skyllas-Kazacos, M.; Grossmith, F. Efficient vanadium redox flow cell. *J. Electrochem. Soc.* **1987**, *134*, 2950. [[CrossRef](#)]
160. Wu, W.-F.; Yan, X.; Zhan, Y. Recent progress of electrolytes and electrocatalysts in neutral aqueous zinc-air batteries. *Chem. Eng. J.* **2023**, *451*, 138608. [[CrossRef](#)]
161. Li, Y.; Dai, H. Recent advances in zinc–air batteries. *Chem. Soc. Rev.* **2014**, *43*, 5257–5275. [[CrossRef](#)]
162. Xu, M.; Ivey, D.; Xie, Z.; Qu, W. Rechargeable Zn–air batteries: Progress in electrolyte development and cell configuration advancement. *J. Power Sources* **2015**, *283*, 358–371. [[CrossRef](#)]
163. Pan, J.; Xu, Y.Y.; Yang, H.; Dong, Z.; Liu, H.; Xia, B.Y. Advanced architectures and relatives of air electrodes in Zn–air batteries. *Adv. Sci.* **2018**, *5*, 1700691. [[CrossRef](#)] [[PubMed](#)]
164. Lv, X.W.; Wang, Z.; Lai, Z.; Liu, Y.; Ma, T.; Geng, J.; Yuan, Z.Y. Rechargeable zinc–air batteries: Advances, challenges, and prospects. *Small* **2024**, *20*, 2306396. [[CrossRef](#)]
165. Li, Y.; Gong, M.; Liang, Y.; Feng, J.; Kim, J.-E.; Wang, H.; Hong, G.; Zhang, B.; Dai, H. Advanced zinc-air batteries based on high-performance hybrid electrocatalysts. *Nat. Commun.* **2013**, *4*, 1805. [[CrossRef](#)] [[PubMed](#)]
166. Wang, H.F.; Tang, C.; Zhang, Q. A review of precious-metal-free bifunctional oxygen electrocatalysts: Rational design and applications in Zn–air batteries. *Adv. Funct. Mater.* **2018**, *28*, 1803329. [[CrossRef](#)]
167. Yu, P.; Wang, L.; Sun, F.; Xie, Y.; Liu, X.; Ma, J.; Wang, X.; Tian, C.; Li, J.; Fu, H. Co Nanosheets rooted on Co–N–C nanosheets as efficient oxygen electrocatalyst for Zn–air batteries. *Adv. Mater.* **2019**, *31*, 1901666. [[CrossRef](#)]
168. Han, X.; Ling, X.; Wang, Y.; Ma, T.; Zhong, C.; Hu, W.; Deng, Y. Spatial isolation of zeolitic imidazole frameworks-derived cobalt catalysts: From nanoparticle, atomic cluster to single atom. *Angew. Chem. Int. Ed.* **2019**, *58*, 5359–5364. [[CrossRef](#)]
169. Shang, H.; Zhou, X.; Dong, J.; Li, A.; Zhao, X.; Liu, Q.; Lin, Y.; Pei, J.; Li, Z.; Jiang, Z. Engineering unsymmetrically coordinated Cu-S1N3 single atom sites with enhanced oxygen reduction activity. *Nat. Commun.* **2020**, *11*, 3049. [[CrossRef](#)]
170. Zhang, J.; Zhou, Q.; Tang, Y.; Zhang, L.; Li, Y. Zinc–air batteries: Are they ready for prime time? *Chem. Sci.* **2019**, *10*, 8924–8929. [[CrossRef](#)] [[PubMed](#)]
171. Deiss, E.; Holzer, F.; Haas, O. Modeling of an electrically rechargeable alkaline Zn–air battery. *Electrochim. Acta* **2002**, *47*, 3995–4010. [[CrossRef](#)]
172. Ma, H.; Wang, B.; Fan, Y.; Hong, W. Development and characterization of an electrically rechargeable zinc-air battery stack. *Energies* **2014**, *7*, 6549–6557. [[CrossRef](#)]
173. Org, W.; Hong, W.; Li, H.; Wang, B. ELECTROCHEMICAL SCIENCE A Horizontal Three-Electrode Structure for Zinc-Air Batteries with Long-Term Cycle Life and High Performance. *Int. J. Electrochem. Sci.* **2016**, *11*, 3843–3851.
174. Li, P.-C.; Chien, Y.-J.; Hu, C.-C. Novel configuration of bifunctional air electrodes for rechargeable zinc–air batteries. *J. Power Sources* **2016**, *313*, 37–45. [[CrossRef](#)]
175. Park, M.G.; Lee, D.U.; Seo, M.H.; Cano, Z.P.; Chen, Z. 3D ordered mesoporous bifunctional oxygen catalyst for electrically rechargeable zinc–air batteries. *Small* **2016**, *12*, 2707–2714. [[CrossRef](#)]
176. Nazir, G.; Rehman, A.; Lee, J.-H.; Kim, C.-H.; Gautam, J.; Heo, K.; Hussain, S.; Ikram, M.; AlObaid, A.A.; Lee, S.-Y. A Review of Rechargeable Zinc–Air Batteries: Recent Progress and Future Perspectives. *Nano-Micro Lett.* **2024**, *16*, 138. [[CrossRef](#)]
177. Liu, Q.; Liu, R.; He, C.; Xia, C.; Guo, W.; Xu, Z.-L.; Xia, B.Y. Advanced polymer-based electrolytes in zinc–air batteries. *eScience* **2022**, *2*, 453–466. [[CrossRef](#)]
178. Belete, A.S.; Worku, A.K.; Ayele, D.W.; Assegie, A.A.; Teshager, M.A. The Recent Advancement of Graphene-Based Cathode Material for Rechargeable Zinc–Air Batteries. *Processes* **2024**, *12*, 1684. [[CrossRef](#)]
179. Leong, K.W.; Wang, Y.; Ni, M.; Pan, W.; Luo, S.; Leung, D.Y. Rechargeable Zn-air batteries: Recent trends and future perspectives. *Renew. Sustain. Energy Rev.* **2022**, *154*, 111771. [[CrossRef](#)]
180. Wu, M.; Zhang, G.; Tong, H.; Liu, X.; Du, L.; Chen, N.; Wang, J.; Sun, T.; Regier, T.; Sun, S. Cobalt (II) oxide nanosheets with rich oxygen vacancies as highly efficient bifunctional catalysts for ultra-stable rechargeable Zn-air flow battery. *Nano Energy* **2021**, *79*, 105409. [[CrossRef](#)]

181. Huang, S.; Zhang, H.; Zhuang, J.; Zhou, M.; Gao, M.; Zhang, F.; Wang, Q. Redox-Mediated Two-Electron Oxygen Reduction Reaction with Ultrafast Kinetics for Zn–Air Flow Battery. *Adv. Energy Mater.* **2022**, *12*, 2103622. [[CrossRef](#)]
182. Papanikolaou, M.; Hadjithoma, S.; Keramidis, O.; Drouza, C.; Amoiridis, A.; Themistokleous, A.; Hayes, S.C.; Miras, H.N.; Lianos, P.; Tsipis, A.C. Experimental and Theoretical Investigation of the Mechanism of the Reduction of O₂ from Air to O₂²⁻ by VIVO₂+–N, N, N-Amide Compounds and Their Potential Use in Fuel Cells. *Inorg. Chem.* **2024**, *63*, 3229–3249. [[CrossRef](#)] [[PubMed](#)]
183. Zhang, Y.; Deng, Y.-P.; Wang, J.; Jiang, Y.; Cui, G.; Shui, L.; Yu, A.; Wang, X.; Chen, Z. Recent progress on flexible Zn-air batteries. *Energy Storage Mater.* **2021**, *35*, 538–549. [[CrossRef](#)]
184. Fang, W.; Zhao, J.; Zhang, W.; Chen, P.; Bai, Z.; Wu, M. Recent progress and future perspectives of flexible Zn–Air batteries. *J. Alloys Compd.* **2021**, *869*, 158918. [[CrossRef](#)]
185. Liu, H.; Xie, W.; Huang, Z.; Yao, C.; Han, Y.; Huang, W. Recent advances in flexible Zn–Air batteries: Materials for electrodes and electrolytes. *Small Methods* **2022**, *6*, 2101116. [[CrossRef](#)]
186. Jiang, L.; Luo, X.; Wang, D.W. A review on system and materials for aqueous flexible metal–air batteries. *Carbon Energy* **2023**, *5*, e284. [[CrossRef](#)]
187. Liu, Y.; Sun, Q.; Li, W.; Adair, K.R.; Li, J.; Sun, X. A comprehensive review on recent progress in aluminum–air batteries. *Green Energy Environ.* **2017**, *2*, 246–277. [[CrossRef](#)]
188. Liu, X.; Jiao, H.; Wang, M.; Song, W.-l.; Xue, J.; Jiao, S. Current progresses and future prospects on aluminium–air batteries. *Int. Mater. Rev.* **2022**, *67*, 734–764. [[CrossRef](#)]
189. Goel, P.; Dobhal, D.; Sharma, R. Aluminum–air batteries: A viability review. *J. Energy Storage* **2020**, *28*, 101287. [[CrossRef](#)]
190. Mori, R. Recent developments for aluminum–air batteries. *Electrochem. Energy Rev.* **2020**, *3*, 344–369. [[CrossRef](#)]
191. Mori, R. Rechargeable aluminum–air battery using various air-cathode materials and suppression of byproducts formation on both anode and air cathode. *ECS Trans.* **2017**, *80*, 377. [[CrossRef](#)]
192. Zhao, Q.; Yu, H.; Fu, L.; Wu, P.; Li, Y.; Li, Y.; Sun, D.; Wang, H.; Tang, Y. Electrolytes for aluminum–air batteries: Advances, challenges, and applications. *Sustain. Energy Fuels* **2023**, *7*, 1353–1370. [[CrossRef](#)]
193. Xu, Y.; Zhao, Y.; Ren, J.; Zhang, Y.; Peng, H. An all-solid-state fiber-shaped aluminum–air battery with flexibility, stretchability, and high electrochemical performance. *Angew. Chem.* **2016**, *128*, 8111–8114. [[CrossRef](#)]
194. Yang, S.; Knickle, H. Design and analysis of aluminum/air battery system for electric vehicles. *J. Power Sources* **2002**, *112*, 162–173. [[CrossRef](#)]
195. Tang, Y.; Lu, L.; Roesky, H.W.; Wang, L.; Huang, B. The effect of zinc on the aluminum anode of the aluminum–air battery. *J. Power Sources* **2004**, *138*, 313–318. [[CrossRef](#)]
196. Garcia-Garcia, F.; Skeldon, P.; Thompson, G.; Smith, G. The effect of nickel on alloy microstructure and electrochemical behaviour of AA1050 aluminium alloy in acid and alkaline solutions. *Electrochim. Acta* **2012**, *75*, 229–238. [[CrossRef](#)]
197. Ryu, J.; Park, M.; Cho, J. Advanced technologies for high-energy aluminum–air batteries. *Adv. Mater.* **2019**, *31*, 1804784. [[CrossRef](#)] [[PubMed](#)]
198. Yirka, B. Phinergy Demonstrates Aluminum–air Battery Capable of Fueling an Electric Vehicle for 1000 Miles. *PHYS ORG.* 27 March 2013. Available online: <https://phys.org/news/2013-03-phinergy-aluminum-air-battery-capable-fueling.html> (accessed on 16 August 2024).
199. Vegh, J.M.; Alonso, J.J. Design and optimization of short-range aluminum-air powered aircraft. In Proceedings of the 54th AIAA Aerospace Sciences Meeting, San Diego, CA, USA, 4–8 January 2016; p. 1026.
200. Rewatkar, P.; Goel, S. Catalyst-mitigated arrayed aluminum-air origami fuel cell with ink-jet printed custom-porosity cathode. *Energy* **2021**, *224*, 120017. [[CrossRef](#)]
201. Huang, H.; Liu, P.; Ma, Q.; Tang, Z.; Wang, M.; Hu, J. Enabling a high-performance saltwater Al-air battery via ultrasonically driven electrolyte flow. *Ultrason. Sonochem.* **2022**, *88*, 106104. [[CrossRef](#)] [[PubMed](#)]
202. Zhang, L.; Shao, Q.; Zhang, J. An overview of non-noble metal electrocatalysts and their associated air cathodes for Mg-air batteries. *Mater. Rep. Energy* **2021**, *1*, 100002. [[CrossRef](#)]
203. Raghavan, P.; Das, A.; Jabeen Fatima, M.J. *Advanced Technologies for Rechargeable Batteries: Metal Ion, Hybrid, and Metal-Air Batteries*; CRC Press: Boca Raton, FL, USA, 2024.
204. Li, C.S.; Sun, Y.; Gebert, F.; Chou, S.L. Current progress on rechargeable magnesium–air battery. *Adv. Energy Mater.* **2017**, *7*, 1700869. [[CrossRef](#)]
205. Chen, X.; Venezuela, J.; Shi, Z.; Wang, L.; Dargusch, M. Ultra-high-purity Mg-Ge anodes enable a long-lasting, high energy-density Mg-air battery. *Nano Energy* **2024**, *122*, 109269. [[CrossRef](#)]
206. Li, L.; Chen, H.; He, E.; Wang, L.; Ye, T.; Lu, J.; Jiao, Y.; Wang, J.; Gao, R.; Peng, H. High-energy-density magnesium-air battery based on dual-layer gel electrolyte. *Angew. Chem.* **2021**, *133*, 15445–15450. [[CrossRef](#)]
207. Huang, X.; Liu, Y.; Park, W.; Zhao, Z.; Li, J.; Lim, C.K.; Wong, T.H.; Yiu, C.K.; Gao, Y.; Zhou, J. Stretchable magnesium–air battery based on dual ions conducting hydrogel for intelligent biomedical applications. *InfoMat* **2023**, *5*, e12388. [[CrossRef](#)]

208. Guo, Z.; Zhao, S.; Li, T.; Su, D.; Guo, S.; Wang, G. Recent advances in rechargeable magnesium-based batteries for high-efficiency energy storage. *Adv. Energy Mater.* **2020**, *10*, 1903591. [[CrossRef](#)]
209. Peled, E.; Golodnitsky, D.; Mazor, H.; Goor, M.; Avshalomov, S. Parameter analysis of a practical lithium-and sodium-air electric vehicle battery. *J. Power Sources* **2011**, *196*, 6835–6840. [[CrossRef](#)]
210. Qin, L.; Xiao, N.; Zhang, S.; Chen, X.; Wu, Y. From K-O₂ to K-Air batteries: Realizing superoxide batteries on the basis of dry ambient air. *Angew. Chem. Int. Ed.* **2020**, *59*, 10498–10501. [[CrossRef](#)] [[PubMed](#)]
211. Mao, P.; Arandiyani, H.; Mofarah, S.S.; Koshy, P.; Pozo-Gonzalo, C.; Zheng, R.; Wang, Z.; Wang, Y.; Bhargava, S.K.; Sun, H. A comprehensive review of cathode materials for Na-air batteries. *Energy Adv.* **2023**, *2*, 465–502. [[CrossRef](#)]
212. Qin, L.; Ao, H.; Wu, Y. Feasibility of achieving two-electron K-O₂ batteries. *Faraday Discuss.* **2024**, *248*, 60–74. [[CrossRef](#)]
213. Yu, W.; Lau, K.C.; Lei, Y.; Liu, R.; Qin, L.; Yang, W.; Li, B.; Curtiss, L.A.; Zhai, D.; Kang, F. Dendrite-free potassium-oxygen battery based on a liquid alloy anode. *ACS Appl. Mater. Interfaces* **2017**, *9*, 31871–31878. [[CrossRef](#)] [[PubMed](#)]
214. Wang, T.; Han, Y.; Xu, P.; Feng, X.; Ji, W.; Arandiyani, H. In-situ generating highly efficient sites for multifunctional water splitting/Zn-air battery over hierarchically architected Fe₂Ni₃ nanoalloy/N-incorporated carbon matrix. *Chem. Eng. J.* **2022**, *450*, 138245. [[CrossRef](#)]
215. Lutz, L.; Alves Dalla Corte, D.; Tang, M.; Salager, E.; Deschamps, M.; Grimaud, A.; Johnson, L.; Bruce, P.G.; Tarascon, J.-M. Role of electrolyte anions in the Na-O₂ battery: Implications for NaO₂ solvation and the stability of the sodium solid electrolyte interphase in glyme ethers. *Chem. Mater.* **2017**, *29*, 6066–6075. [[CrossRef](#)]
216. Yadegari, H.; Sun, X. Sodium-oxygen batteries: Recent developments and remaining challenges. *Trends Chem.* **2020**, *2*, 241–253. [[CrossRef](#)]
217. Kang, Y.; Wang, S.; Zhu, S.; Gao, H.; San Hui, K.; Yuan, C.-Z.; Yin, H.; Bin, F.; Wu, X.-L.; Mai, W. Iron-modulated nickel cobalt phosphide embedded in carbon to boost power density of hybrid sodium-air battery. *Appl. Catal. B Environ.* **2021**, *285*, 119786. [[CrossRef](#)]
218. Xu, C.; Zhang, K.; Zhang, D.; Chang, S.; Liang, F.; Yan, P.; Yao, Y.; Qu, T.; Zhan, J.; Ma, W. Reversible hybrid sodium-CO₂ batteries with low charging voltage and long-life. *Nano Energy* **2020**, *68*, 104318. [[CrossRef](#)]
219. Enterría, M.; Reynaud, M.; Paredes, J.I.; Medinilla, L.; Younesi, R.; Ortiz-Vitoriano, N. Driving the sodium-oxygen battery chemistry towards the efficient formation of discharge products: The importance of sodium superoxide quantification. *J. Energy Chem.* **2022**, *68*, 709–720. [[CrossRef](#)]
220. Duan, C.; Li, X.; Wang, D.; Wang, Z.; Sun, H.; Zheng, R.; Liu, Y. Nanosized high entropy spinel oxide (FeCoNiCrMn)₃O₄ as a highly active and ultra-stable electrocatalyst for the oxygen evolution reaction. *Sustain. Energy Fuels* **2022**, *6*, 1479–1488. [[CrossRef](#)]
221. Cohn, G.; Starosvetsky, D.; Hagiwara, R.; Macdonald, D.D.; Ein-Eli, Y. Silicon-air batteries. *Electrochim. Commun.* **2009**, *11*, 1916–1918. [[CrossRef](#)]
222. Zhong, X.; Zhang, H.; Liu, Y.; Bai, J.; Liao, L.; Huang, Y.; Duan, X. High-Capacity Silicon-Air Battery in Alkaline Solution. *ChemSusChem* **2012**, *5*, 177–180. [[CrossRef](#)]
223. Park, D.-W.; Kim, S.; Ocon, J.D.; Abrenica, G.H.A.; Lee, J.K.; Lee, J. Controlled electrochemical etching of nanoporous Si anodes and its discharge behavior in alkaline Si-air batteries. *ACS Appl. Mater. Interfaces* **2015**, *7*, 3126–3132. [[CrossRef](#)] [[PubMed](#)]
224. Durmus, Y.E.; Aslanbas, Ö.; Kayser, S.; Tempel, H.; Hausen, F.; De Haart, L.; Granwehr, J.; Ein-Eli, Y.; Eichel, R.-A.; Kungl, H. Long run discharge, performance and efficiency of primary Silicon-air cells with alkaline electrolyte. *Electrochim. Acta* **2017**, *225*, 215–224. [[CrossRef](#)]
225. Schalinski, R.; Schweizer, S.L.; Wehrspohn, R.B. The Role of Silicate Enrichment on the Discharge Duration of Silicon-Air Batteries. *ChemSusChem* **2023**, *16*, e202300077. [[CrossRef](#)]
226. Montiel Guerrero, S.S.; Durmus, Y.E.; Tempel, H.; Roth, C.; Kungl, H.; van Waasen, S.; Ein-Eli, Y.; Eichel, R.A. Unveiling the Potential of Silicon-Air Batteries for Low-Power Transient Electronics: Electrochemical Insights and Practical Application. *Batter. Supercaps* **2024**, *7*, e202300573. [[CrossRef](#)]
227. Yang, W.-T.; Yu, J.; Li, D.-X.; Hu, S.-Q.; Ding, X.; Chen, F.-Y.; Qiao, C. Performance of silicon-air batteries using industrial silicon as anode. *J. Mater. Sci. Mater. Electron.* **2023**, *34*, 800. [[CrossRef](#)]
228. Lu, Y.-T.; Neale, A.R.; Hu, C.-C.; Hardwick, L.J. Divalent nonaqueous metal-air batteries. *Front. Energy Res.* **2021**, *8*, 602918. [[CrossRef](#)]
229. Ocon, J.D.; Kim, J.W.; Uhm, S.; Mun, B.S.; Lee, J. An etched nanoporous Ge anode in a novel metal-air energy conversion cell. *Phys. Chem. Chem. Phys.* **2013**, *15*, 6333–6338. [[CrossRef](#)]
230. Ye, L.; Liao, M.; Zhang, K.; Zheng, M.; Jiang, Y.; Cheng, X.; Wang, C.; Xu, Q.; Tang, C.; Li, P. A rechargeable calcium-oxygen battery that operates at room temperature. *Nature* **2024**, *626*, 313–318. [[CrossRef](#)]
231. Fang, C.; Tang, X.; Wang, J.; Yi, Q. Performance of iron-air battery with iron nanoparticle-encapsulated CN composite electrode. *Front. Energy* **2024**, *18*, 42–53. [[CrossRef](#)]

-
232. Global EV Outlook 2024, Paris. 2024. Available online: <https://www.iea.org/reports/global-ev-outlook-2024> (accessed on 15 October 2024).
 233. Gallagher, K.G.; Goebel, S.; Greszler, T.; Mathias, M.; Oelerich, W.; Eroglu, D.; Srinivasan, V. Quantifying the promise of lithium–air batteries for electric vehicles. *Energy Environ. Sci.* **2014**, *7*, 1555–1563. [[CrossRef](#)]

Disclaimer/Publisher’s Note: The statements, opinions and data contained in all publications are solely those of the individual author(s) and contributor(s) and not of MDPI and/or the editor(s). MDPI and/or the editor(s) disclaim responsibility for any injury to people or property resulting from any ideas, methods, instructions or products referred to in the content.